THESIS FOR THE DEGREE OF DOCTOR OF PHILOSOPHY

Design and Control of a DC Collection Grid for a Wind Farm

LENA MAX

Department of Energy and Environment
CHALMERS UNIVERSITY OF TECHNOLOGY
Göteborg, Sweden 2009

Design and Control of a DC Collection Grid for a Wind Farm
LENA MAX
ISBN 978-91-7385-333-0

Doktorsavhandlingar vid Chalmers tekniska högskola
Ny serie nr. 3014
ISSN 0346-718X

Department of Energy and Environment
Chalmers University of Technology
SE–412 96 Göteborg
Sweden
Telephone +46 (0)31–772 1000

Chalmers Bibliotek, Reproservice
Göteborg, Sweden 2009

Design and Control of a DC Collection Grid for a Wind Farm
LENA MAX
Department of Energy and Environment
Chalmers University of Technology

Abstract

In this thesis, the internal DC collection grid for a wind farm is investigated regarding the design, losses and dynamic operation for both normal operating conditions and for different fault conditions. The main advantage for the DC collection grid is the considerably lower weight of the 1 kHz transformers in the DC/DC converters compared to the equivalent 50 Hz transformers. For a wind farm with 48 2.3 MW wind turbines, and a DC/DC converter in each turbine as well as a main DC/DC converter for the whole wind farm, the losses for the DC system are 3 % of the transferred power, which is similar to the losses of a corresponding AC collection grid. For the dynamic control of the wind farm, the DC/DC converters control the power flow in the wind farm and thereby also the voltage levels for the 1.5 kV DC link in the turbine as well as for the 32 kV DC collection bus. For the limited bandwidth resulting from the switching frequency 1 kHz and the maximum voltage deviations of 5 % for the DC voltages, the required capacitances are 152 mF for the DC link in the wind turbine and 16 mF for the DC bus, both giving a stored energy corresponding to 74 ms transferred rated power. In the case of a fault in the connecting main grid, the output power from the wind farm must be decreased. Here, assuming that the excess power is dissipated in each turbine, the detection of the fault as well as the disconnection and the reconnection of the wind farm are investigated. The requirements for the HVDC link to avoid over voltages during a grid fault are stated and it is also shown that the reconnection can be done within 14 ms, which is well within the time specified in existing grid codes. Further, the behavior of the system during internal faults for the DC bus is investigated. Methods for detecting and finding the location of the faults are determined, and it is shown that a faulted part can be disconnected and the non-faulted parts reconnected within 300 ms without using fully rated DC breakers.

Index Terms: DC/DC converter, DC collection grid, loss evaluation, wind energy, control design, fault handling.

Acknowledgements

The financial support for this research project given by the Swedish Energy Agency (Energimyndigheten) is gratefully acknowledged.

I would like to thank my supervisors Associate Prof. Ola Carlson and Prof. Torbjörn Thiringer for all support, guidance and encouragement during the project. I would also like to thank my examiner Prof. Tore Undeland for his support and valuable comments. The reference group consisting of Dr. Philip Kjær, Dr. Georgios Demetriades, Dr. Per Karlsson and Sven Sjöberg is also gratefully acknowledged for providing valuable input during the project.

I would like to thank the master thesis workers Thomas Nyikos and Tobias Tomaschett from ETH for their work with the experimental setup and Robert Karlsson for the help during the experimental work.

Further, many thanks go to my friends and colleagues in the Division of Electric Power Engineering and in the Division of High Voltage Engineering, especially Johan Andersson, Massimo Bongiorno, Jimmy Ehnberg, Ramona Huuva, Elisabeth Lindell and Stefan Lundberg, for making the working environment enjoyable.

Finally, I would like to thank my family and Mattias for their love and support.

Lena Max
Göteborg, Sweden
November, 2009

Contents

Chapter 1

Introduction

1.1 Problem background

The introduction of DC technology for wind farm applications is a present development including both research and commercial projects. The main focus in this stage is to use an HVDC (High Voltage DC) transmission between the wind farm and the connecting grid. A first demonstration project was built in Tjæreborg, Denmark in 2000, where a 8 MVA HVDC link was connecting a small wind farm with 4 turbines to the grid [1, 2]. A larger wind farm of 400 MW is currently being constructed outside Germany, where the transmission distance for the HVDC link to the connection to the grid is 200 km [2]. The main purpose of having an HVDC transmission for a wind farm is to enable a long distance cable transmission of high power. As more large wind farms are planned for offshore locations, HVDC transmission will be a more common transmission solution for new wind farms. There are also suggestions of having multi-terminal HVDC systems connecting several wind farms.

For wind farms, and especially for offshore locations, the weight of the components is an important issue. If the DC technology also would be used to replace the internal AC grid in the wind farm with a DC grid, the traditional 50 Hz transformers are replaced with DC/DC converters including medium frequency transformers, and the AC cables are replaced by DC cables. The weight of the medium frequency transformers in the DC/DC converters is significantly lower than the weight of equivalent traditional 50 Hz transformers. Thereby, the weight of the turbine and also the offshore platform connecting to the HVDC link can be reduced. Also, the DC cables have lower losses than the AC cables and there is no limitation for the transmission distance. Today, the key components for the DC grid for a wind farm, the DC/DC converters, as well as the DC breakers are still under development and not commercially available. Also, the operation of the wind farm including control during normal operation and during different faults must be studied further.

1.2 Overview of Previous Work

The previous work regarding DC solutions for wind farms has mainly been focused on the possibility to use HVDC as the transmission system. Starting with the steady-state characteristics for the HVDC link, the resulting losses for the HVDC system have been compared with the losses using the traditional HVAC (High Voltage AC) system in [3, 4, 5]. Also the cost has been evaluated for the HVDC transmission compared to the HVAC system [4, 5]. It is found that for long transmission distances, the HVDC transmission has both the lowest price and the lowest losses. Further, the fault ride through properties for wind farms with HVDC transmission have been investigated in [6, 7]. Here, the two options are to either use a breaking resistance in the HVDC link or to ”mirror“ the fault from the main grid to the internal wind farm grid using the built-in fault ride through system for the wind turbines. The operation of a wind farm connected to an HVDC transmission is discussed further in [8, 9, 10], also considering the dynamical behavior. The possibility to connect several wind farms, or several clusters within the same wind farm, with a multi-terminal HVDC system is investigated in [11].

The electrical system for the internal grid in the wind farm can be designed in many different ways. From the solution of having an internal AC grid connected to an HVDC transmission, the groups of turbines can be made smaller as in [11], where a wind farm consists of 25 groups of 4 turbines where each group of turbines is connected to a separate HVDC converter. In [9], all turbines in the wind farm have a separate HVDC converter, thus forming a multi terminal HVDC system within the wind farm. This solution has the advantage of no extra substation, but the disadvantage of the high voltage for the HVDC transmission present in each turbine.

By introducing high power DC/DC converters, it is possible to have an internal DC bus in the wind farm with a lower voltage level, and the voltage is then increased by the DC/DC converter to the HVDC transmission level. The high power DC/DC converters, that are key components for the implementation of a wind farm with an internal DC bus, are still under development [12]. These DC/DC converters have medium frequency transformers that are significantly smaller and less heavy compared to ordinary 50 Hz transformers [13]. A low weight is a significant advantage, especially for offshore locations. Having the possibility of different levels of the DC voltage, different solutions for the internal grid in a wind farm have been investigated in [14, 15]. In [14], different configurations of the internal grid for the wind farm have been studied and the wind farm with an internal DC grid was shown to be an interesting alternative. Also the possibility of series connection of the wind turbines is considered in [14] to eliminate the need for an offshore substation. In [15], different layouts for the internal DC grid in a wind farm are investigated, including the control of the HVDC transmission. Here, the solution with the lower losses

is found to be the case where the inverter towards the generator is directly connected to a common low-voltage DC bus. The DC bus is then connected to a DC/DC converter that increases the low output voltage from the generator to the voltage for the HVDC link.

Previously, multi terminal DC systems have been mainly considering systems with lower voltage and power. In [16, 17], the design and control is considered of a DC bus connected to a number of sources and loads, also considering to connect wind turbines. Here, a control system is proposed for a multi-terminal DC system.

For the high power DC collection grid for a wind farm, further research is needed considering the design and control of the system. For steady state operation, the losses should be obtained and compared to the losses of a wind farm with an internal AC grid. Investigating the control during steady state conditions will show the performance of the DC system and also give the resulting requirements for the design of the system. Further, the evaluation of fault cases will show the possible operation during different faults as well as the needed protection devices.

1.3 Aims and Main Contributions of the Thesis

- **Aim:** To investigate DC/DC converters for a wind farm application and find a suitable topology and design for the wind farm with an internal DC collection grid.
  Contribution: The most suitable DC/DC converter topology for the operating conditions in a wind farm has been identified, and for this topology, a suitable control strategy has been determined as well as the switching frequency.

- **Aim:** To find the losses of the DC system in the wind farm.
  Contribution: The losses have been determined for the components in the DC collection grid, and have been put in relation to the losses in a wind farm with an internal AC grid.

- **Aim:** To develop the control of the system during steady state and determine the resulting requirements for the design of the system.
  Contribution: A control strategy for the wind farm has been developed, where the DC/DC converters control the power flow and thereby also the DC link voltages. It has been identified that the bandwidth of the controller and the limitation of the voltage variations to 5 % determine the required DC link capacitances, which are obtained for the investigated system.

- **Aim:** To show the operation of the wind farm during different fault conditions, both for faults in the main grid and for internal faults in the wind farm. Both the detection and the clearing of the faults should be investigated, and the requirements for the

system should be determined.

Contribution: The safe operation of the wind farm for both external and internal faults has been demonstrated. For external faults, the fault ride through operation has been established including the detection of the fault and the required system properties to avoid over voltages. Also, it has been proven that the wind farm can reconnect after the fault well within the time specified in existing grid codes. For internal faults, a methodology for a robust detection and localization of the fault has been demonstrated for different faults for the DC bus. Finally, the detection of an internal fault and the disconnection of the faulted part has been established together with the resulting disturbance in the output power to the HVDC link.

1.4 Layout of the Thesis

This thesis investigates the design and operation of an internal DC collection grid for a wind farm. First, an overview of a wind farm with an internal DC grid is given in Chapter 2. Here, some possible layouts of the internal collection grid are shown and the components in the wind farm are presented. The DC/DC converters are identifies as key components that are studied further in Chapter 3, focusing on the operation in a wind farm with an internal DC grid. A suitable topology for the DC/DC converter is found for the operating conditions in a wind farm. Then, design aspects as control of the converter and choice of switching frequency and IGBT modules are shown for the chosen topology. Finally, the loss calculations for the DC/DC converter are verified with a down scaled experimental setup.

Knowing the design of the DC/DC converters, the complete DC collection grid, including the DC/DC converters, is designed in Chapter 4. Here, the layout of the wind farm used in the investigations of the operation of the wind farm is chosen and the design of the components in the wind farm is determined. For the chosen layout, the losses for the internal DC grid are presented, including the losses for the cables and the DC/DC converters. Further, the dynamic modeling of the wind farm is made in Chapter 5. The models of the different parts are shown in detail, and also an overview of the complete wind farm model is given.

Using the dynamic model of the wind farm, a control strategy for the DC collection grid during normal operating conditions is developed in Chapter 6. A basic control is achieved for the wind turbines to obtain the power flow to the DC grid during normal operation. Further, the control of the DC/DC converters is investigated to maintain stable operation with limited voltage deviations for all possible operating conditions, and the resulting requirement for the DC bus capacitance is obtained. The control method is verified using a down scaled experimental converter. Also the operation during startup of the system is shown. Continuing with the operation during faulted conditions, both internal and external

faults are investigation in Chapter 7. First, the operation during a fault in the connecting main grid is discussed considering the ability of the system to detect a fault and stop the output power. Also, the reconnection of the wind farm after a grid fault is investigated. Further, the operation during internal faults is discussed. The behavior of the system during a fault in the DC collection bus is shown including the detection of these faults and the disconnection of a faulted part. Finally, in Chapter 8 a summary and also concluding remarks are given. There are also some suggestions for future work.

1.5 Publications

The publications originating from this project are:

I **L. Max** and S. Lundberg, "System efficiency of a DC/DC converter based wind turbine grid system," in *Nordic Wind Power Conference (NWPC) 2006*, May., 2006.

II **L. Max**, "Energy efficiency for DC/DC converters in a DC grid system for wind farms," in *Nordic Workshop on Power and Industrial Electronics (NORPIE) 2006*, June 2006.

III **L. Max** and T. Thiringer, " Snubber and control method selection for a 5 MW wind turbine single active bridge DC/DC converter", in *12th European Conference on Power Electronics and Applications (EPE) 2007*.

IV **L. Max**, "Design aspects for a fullbridge converter thought for an application in a DC-based wind farm," in *Nordic Wind Power Conference (NWPC) 2007*, November., 2007.

V **L. Max** and S. Lundberg, "System efficiency of a DC/DC converter based wind farm," in *Wind Energy Journal*, vol.11, no.1, January/February 2008, p.109-120.

VI **L. Max** and T. Thiringer "Design and Control Considerations for a 5 MW Fullbridge DC/DC Converter in a Wind Turbine" in *EPE Wind Energy Chapter 2009 - 2nd seminar*

VII **L. Max** and O. Carlson, "Control and Loss Calculations for an Internal DC Grid in a Wind Farm," in *Nordic Wind Power Conference (NWPC) 2009*, September., 2009.

VIII **L. Max**, T. Thiringer and O. Carlson, "Control of a Wind Farm with an Internal DC Collection Grid" submitted to *IEEE Transactions on Energy Conversion*

IX **L. Max**, T. Thiringer and O. Carlson, "Fault Handling for a Wind Farm with an Internal DC Collection Grid" submitted to *IEEE Transactions on Energy Conversion*

Chapter 2

Design Overview of a Wind Farm with a DC Grid

2.1 Introduction

For a wind farm with an internal DC collection grid, there are several design aspects that must be considered. First, the layout of the wind farm must be chosen including the connection for the turbines. Then, also the different components must be determined. In this chapter, an overview is given of the layout and the main components, which are the wind turbines and the DC/DC converters as well as the DC cables and the protection system.

2.2 Layout of a Wind Farm with a DC Collection Grid

A wind farm with an internal DC grid can be designed in several different ways [13, 14, 15]. One option is to design the wind farm with a DC grid in a similar way as a wind farm with an AC grid, where the turbines are connected in radials to a common DC/DC converter as shown in Fig. 2.1 [14, 15].

In a wind farm with an internal DC grid, the AC cables in a traditional wind farm with an AC grid are replaced with DC cables, and the 50 Hz transformers are replaced with DC/DC converters with internal medium frequency transformers. As seen in the figure, a number of wind turbines are connected to a common DC bus that is connected to a DC/DC converter that will achieve the voltage level needed for the transmission system.

For the wind turbines connected to the internal DC collection grid, the output must be a DC voltage, and in Fig. 2.2 the electrical system used for a wind turbine with a DC output is shown.

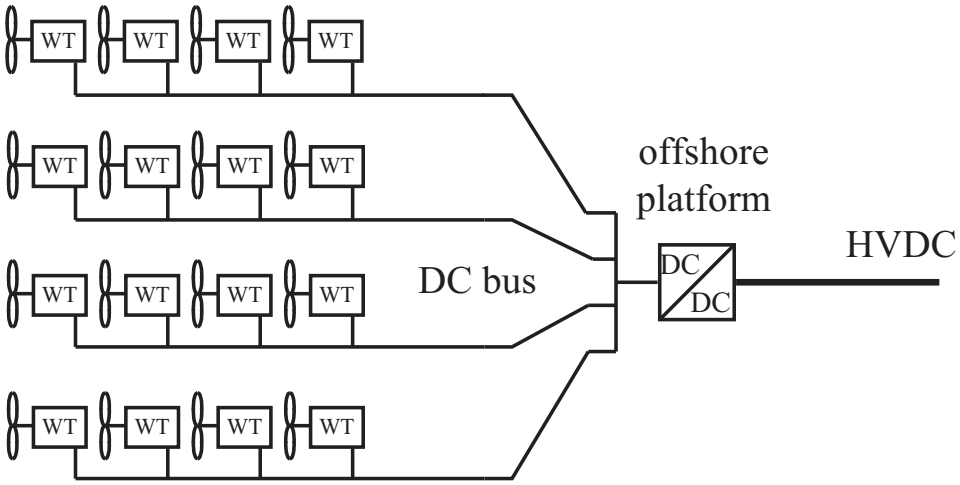

Fig. 2.1 Example of a layout of a wind farm with an internal DC collection grid.

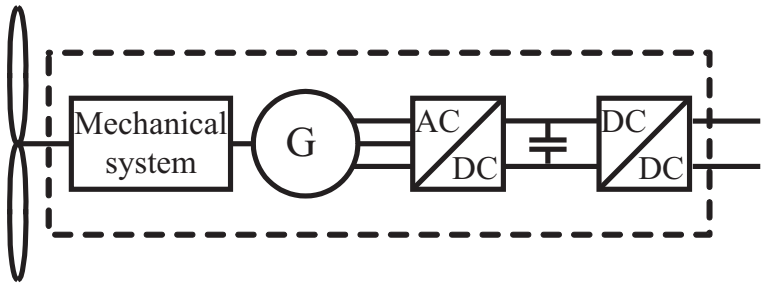

Fig. 2.2 A wind turbine with a DC output voltage.

In the wind turbine with a DC output, a full power converter is connected to the generator. A DC/DC converter is then connected between the internal DC link in the turbine and the DC collection grid to control the power flow and increase the voltage level. Consequently, there will be two DC/DC converters between each turbine and the HVDC transmission, one converter in the turbine and one converter for the whole wind farm increasing the voltage to the HVDC transmission as shown in Fig. 2.1.

For the wind farm shown in Figs. 2.1 and 2.2, the voltage levels can be chosen freely for the DC link in the turbine, the internal DC collection grid and the HVDC link. In [15], three different options are compared for the internal DC collection grid. The first option is to use the layout shown above, with a DC/DC converter in each wind turbine and also a DC/DC converter between the internal DC bus and the HVDC link. The second option is to remove the DC/DC converter in the wind turbine and thereby lower the losses. However, the voltage for the DC bus is then limited by the generator voltage and the DC link voltages in the turbines can not be controlled independently for each turbine. The third

option is to remove the DC/DC converter between the internal grid and the HVDC link and keep the converter in the wind turbine, which also will reduce the losses. However, in this case the voltage for the HVDC transmission will be present in all turbines, affecting the design of the turbines. The losses for these systems are compared in [15], and it was shown that the configuration with two DC/DC converters gives the highest losses. Further, it was stated that the transformer for one turbine has reduced efficiency compared to larger components, and therefore the solution with just one DC/DC converter towards the HVDC link has the lowest losses.

Another option to eliminate the DC/DC converter connecting the wind farm to the HVDC link is to connect the wind turbines in series as shown in Fig. 2.3 [13, 14].

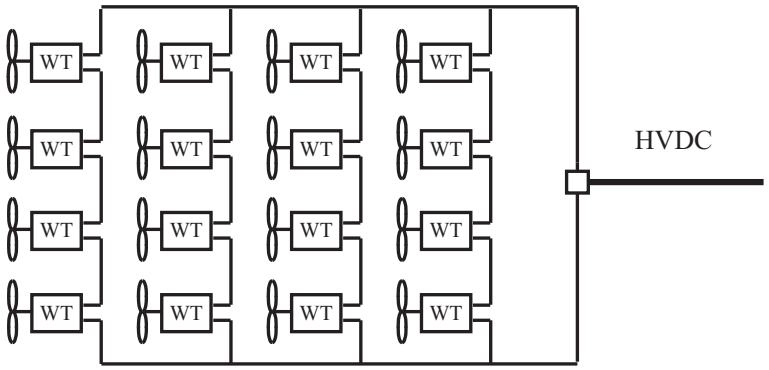

Fig. 2.3 A wind farm with an internal DC grid with series connected turbines.

For the series connected DC wind farm, the HVDC transmission voltage is obtained by adding the output voltages of the turbines connected in series. The advantage of using this configuration is that the DC/DC converter towards the HVDC link is not needed, and the disadvantage is the high potential present in the turbines. Further, the output voltage for the turbines must be overrated in case of the loss of a turbine [14].

2.3 Components in a Wind Farm

2.3.1 Wind Turbines

There are different ways to convert the mechanical power from the rotor blades to electrical energy. For a wind turbine connected to an AC grid, it could either be done with a fixed speed generator or with a variable speed generator. Different types of generator systems are described more in detail in [4, 18] and are here described briefly, and also compared to the wind turbine with a DC output. For all systems, the rotational speed

of the wind turbine is fairly slow and a gearbox is therefore needed to adjust it to the electrical frequency.

Fixed Speed Turbine

The fixed speed generator in Fig. 2.4 consists of an induction generator (IG) directly connected to the grid. The speed of the turbine is fixed and determined by the grid frequency, the gearbox and the pole-pair number of the generator. Due to the "locked" speed operation it is not possible to store the energy in turbulence as rotational energy. The turbulence will then result in power variations leading to mechanical wear and also affect the power quality of the grid. The fixed speed turbine system often have two fixed speeds, which can be achieved either with two generators with different ratings and pole pairs or by a generator with two windings with different ratings and pole pairs.

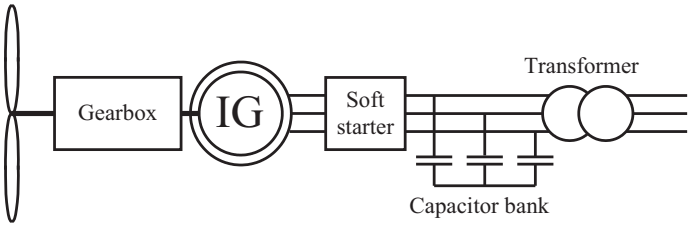

Fig. 2.4 Fixed speed turbine with an induction generator.

Variable Speed Turbine with Doubly Fed Induction Generator

The system in Fig. 2.5 consists of a wind turbine with a doubly fed induction generator (DFIG). In the DFIG, the stator is directly connected to the grid while the rotor is connected to a converter via slip rings. The converter only has to handle 20-30 % of the total power and the losses in the converter can be reduced compared to the converter that has to handle the full power. This system has a sufficient speed range to also smoothen out incoming wind power variations.

Full Variable Speed Turbine

For the variable speed wind turbine in Fig. 2.6, the rotational speed of the turbine is controlled by a full power converter. The generator could be either a synchronous generator or an induction generator. If the generator is designed with multiple poles, the gearbox can be eliminated. In the variable speed wind turbine, power fluctuations caused by varying wind speed can be absorbed by slightly changing the rotor speed.

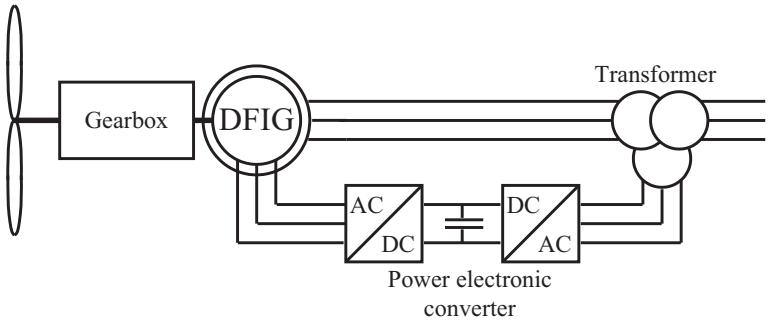

Fig. 2.5 Variable speed turbine with a doubly-fed induction generator (DFIG).

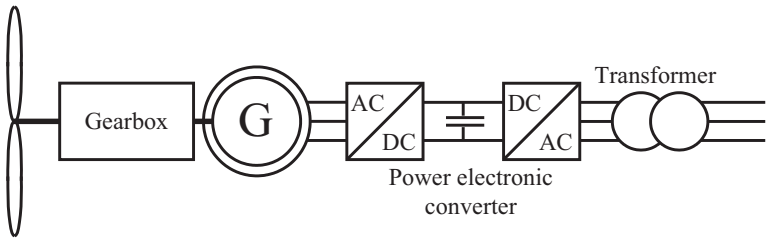

Fig. 2.6 Variable speed turbine with an induction or synchronous generator.

Turbine with a DC Output

The wind turbine with a DC output shown in Fig. 2.7 is similar to the wind turbine with full variable speed. The difference is that the inverter and 50 Hz transformer towards the internal grid is replaced with a DC/DC converter.

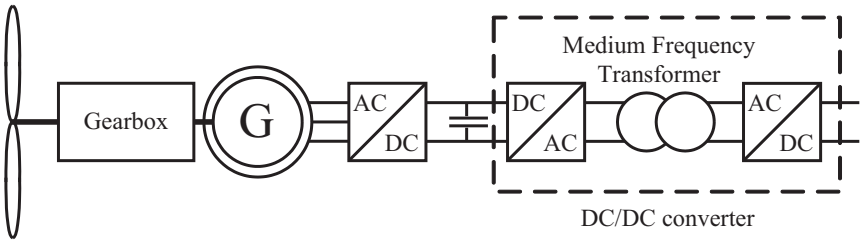

Fig. 2.7 Variable speed turbine with a DC output.

2.3.2 DC/DC converters

As shown in Figs. 2.1 and 2.7, the DC/DC converters are key components in a wind farm with an internal DC collection grid. For the DC/DC converter, an overview of the main components is shown in Fig. 2.8.

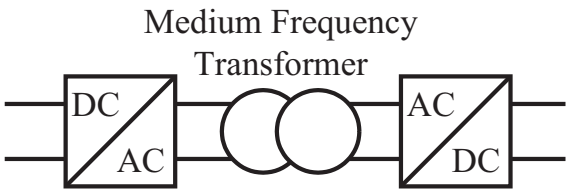

Fig. 2.8 Overview of the DC/DC converter.

Here, the inverter (DC/AC) at the input gives a one phase, medium frequency AC voltage that is applied at the transformer. On the secondary side of the transformer, the AC voltage is rectified to a DC voltage. The waveform of the medium frequency AC voltage depends on the topology of the converter. Further, also filters at the input and output of the DC/DC converter are needed.

DC/DC converters for these high power levels are still under development [12], and are described further in Chapter 3. When designing the converters, the choice of topology is important to achieve as low losses as possible and also a good dynamic performance for the wide range of operating conditions in a wind farm. Also, the medium frequency transformer needs further development before it is commercially available.

2.3.3 Cables and Protection Devices

For a wind farm, the distances between the turbines are normally quite short. Thereby, standard cables can be used in the internal collection grid both for the AC and DC solutions.

For a DC system, the protection is a critical issue. In the case of a fault, it is advantageous if the faulted part can be disconnected. There are available breakers for an AC system, but for the DC system the breakers are still under development [19]. Additional protection devices needed are breaker resistances for discharging a DC link as well as disconnecters that can isolate parts of the wind farm.

2.4 Operating Conditions for a Wind Turbine

When evaluating the design of the components for a wind farm, the operating conditions must be known. The operating point can be found for each wind speed, but if the average losses should be calculated, the wind distribution must be known. The most common probability density function to describe the wind speed is the Weibull function [20], which has the probability function

$$f(\omega_w) = \frac{k}{c}\left(\frac{\omega_w}{c}\right)^{k-1} \exp\left[-\left(\frac{\omega_w}{c}\right)^{k}\right]. \tag{2.1}$$

In (2.1), k is a shape parameter, c is a scale parameter and ω_w is the wind speed. If $k = 2$, the Weibull distribution is known as the Rayleigh distribution where c is given by the average wind speed $\bar{\omega}_w$ [18] as

$$c = \frac{2}{\sqrt{\pi}}\bar{\omega}_w. \tag{2.2}$$

The probability distribution is then given by the average wind speed [20] as

$$f(\omega_w) = \frac{\pi\omega_w}{2\bar{\omega}_w^2} \exp\left[-\frac{\pi\omega_w^2}{4\bar{\omega}_w^2}\right]. \tag{2.3}$$

Evaluating the probability function for the wind speed for the average wind speed $\bar{\omega}_w$ = 8.5 m/s [21], gives the resulting values shown in Fig. 2.9.

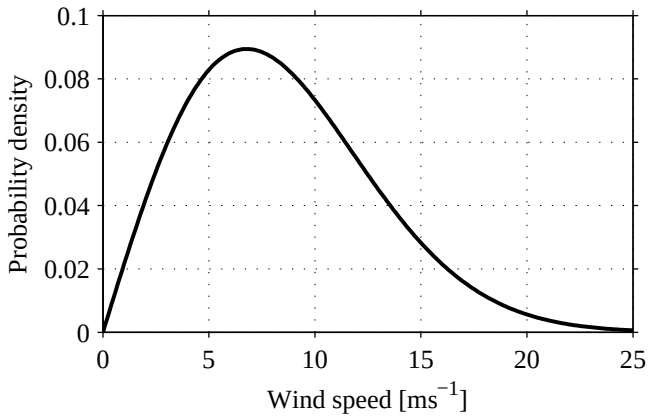

Fig. 2.9 Probability distribution for different wind speeds.

2.5 The Investigated Wind Farms

When investigating a wind farm, both for the operation of the whole wind farm and the properties of the components, the layout of the wind farm must be chosen. In these investigations, the same layout is chosen as shown in Figs. 2.1 and 2.2 with one DC/DC converter in each turbine and one main DC/DC converter for the whole wind farm. The aim is to have a layout that is as similar as possible to the existing wind farms with internal AC grids. Also, a larger number of DC/DC converters gives increased controllability

of the wind farm.

The same principal layout of the wind farm is used in all investigations. However, there are two different alternatives for the size of the turbines and also the number of turbines in the wind farm, one alternative for the investigation of the DC/DC converters and one alternative for the investigation of the whole wind farm.

2.5.1 Wind Farm Layout for Investigation of the DC/DC Converters

Starting with the investigation of the DC/DC converters in Chapter 3, a smaller wind farm with large 5 MW turbines is chosen as described further in Section 3.2.2. It is assumed that these large turbines will be standard in the future and they are therefore used in the investigations. However, the results will be similar for turbines of different sizes since similar components will be used. For this investigation, both constant and varying voltage levels are used for the evaluation of the converters.

2.5.2 Wind Farm Layout for Investigation of the Wind Farm

For the investigation of the whole wind farm including the system losses and the dynamic operation, the layout of an existing wind farm is chosen. Consequently, smaller wind turbines of 2.3 MW are used and the wind farm consists of a larger number of turbines. The layout of the wind farm used for the investigations of the dynamic operation is shown in Section 4.2.

2.6 Summary

In this chapter, an introduction was given to the layout and the components for a wind farm with an internal DC grid. It was shown that a layout similar to the layout of a wind farm with an internal AC grid is used, and that there is a DC/DC converter in each turbine as well as a main DC/DC converter for the whole wind farm connected to the HVDC transmission. Further, it was stated that the high power medium frequency DC/DC converters as well as the protection devices for the DC wind farm are key components that requires further development.

Chapter 3

Design of the DC/DC Converters for a Wind Farm Application

3.1 Introduction

As shown in Chapter 2, the high power medium frequency DC/DC converters are key components for the realization of a wind farm with an internal DC collection grid [12]. When designing the DC/DC converters, a suitable topology must be chosen and the design of the converters must be determined for the specific operating conditions in a wind farm.

The choice of topology for high power (up to 7 MW) medium frequency DC/DC converters have been studied and their performance has been compared in earlier literature [22, 23], including control methods and loss calculations. However, for the application in a wind farm, the converters have to be evaluated for these specific operating conditions. That includes designing the converters for this application and also evaluating the converters for the expected operating conditions.

In this chapter, three different topologies are evaluated for the operating conditions in a wind farm with a DC collection grid. This is shown more in detail in [24, 25], where the topologies are evaluated regarding losses, contribution to energy production cost and also additional factors as design and control of the converters. Here, the DC/DC converters are designed for a large 5 MW turbine using different electrical systems. The operation and the losses for the different topologies will be similar for different sizes of the turbines. When the topologies have been evaluated and a suitable topology has been chosen, the design of the converters is evaluated further. Finally, the loss calculations for the converters are verified using a down scaled experimental setup.

3.2 Choice of Converter Topology

3.2.1 Compared Topologies

Here, the three used topologies are described, which all have a fullbridge that gives a medium frequency voltage to the transformer. Then the diode bridge will rectify the voltage, giving a DC voltage as output. The difference between the fullbridge (FB) converter shown in Fig. 3.1 and the single active bridge (SAB) converter in Fig. 3.2 is the output filter which is current stiff for the fullbridge converter and voltage stiff for the single active bridge converter. For the resonant (LCC) converter shown in Fig. 3.3, resonant elements are inserted close to the transformer, achieving soft switching conditions for the IGBTs (Insulated Gate Bipolar Transistors) in the input bridge. Also the resonant converter has a voltage stiff output.

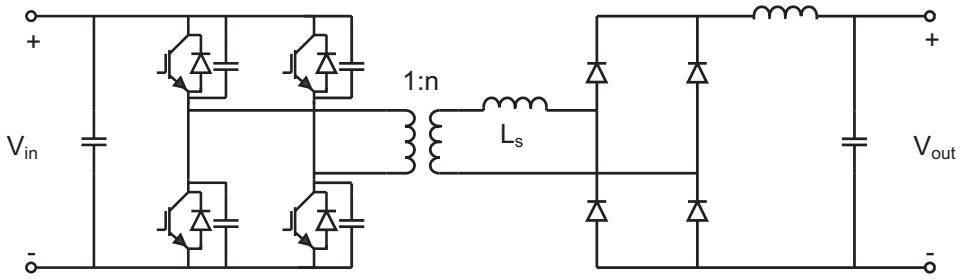

Fig. 3.1 Topology for the fullbridge converter.

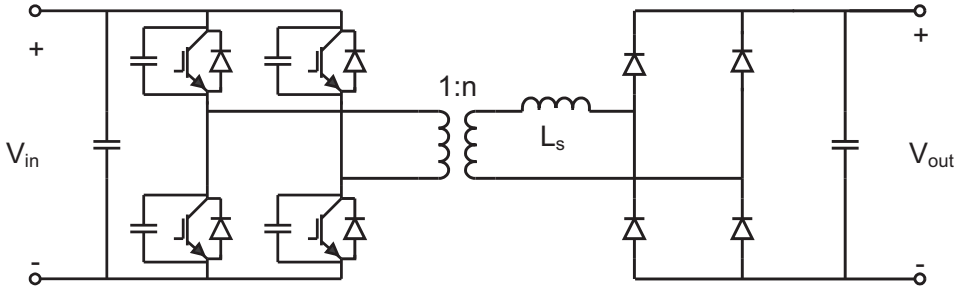

Fig. 3.2 Topology for the single active bridge converter.

Starting with the fullbridge converter, the output voltage is controlled by the duty cycle for the input bridge, and the output voltage is basically proportional to the duty cycle at a constant input voltage. The converter can either be controlled by the hard-switching duty cycle control or the soft-switching phase shift control. In the hard switching duty cycle control, the off-state is achieved by turning all switches off. Thereby, the output current

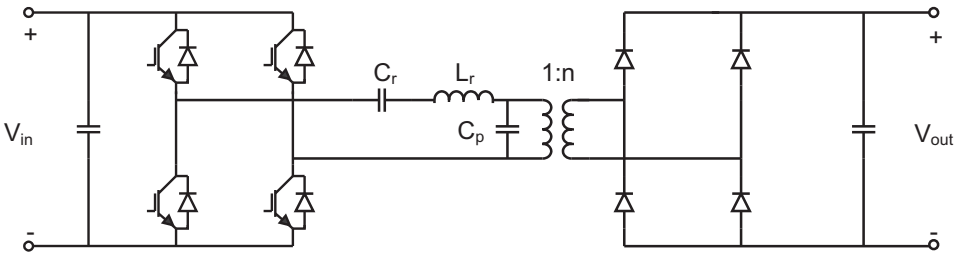

Fig. 3.3 Topology for the resonant converter.

is freewheeling in the output bridge and there is no current neither in the transformer nor in the input bridge. Using this control method, there are no snubber circuits across the transistors in the input bridge and the turn-off losses can therefore be large. Another issue to consider when using duty cycle control is that there can be oscillations in the input bridge during the off-state. In order to reduce the turn-off losses for the transistors, snubber capacitors can be connected across the transistors in Fig. 3.1. The converter is then controlled using phase shift control as described in [22, 26, 27]. During the off-state, one transistor and one diode are conducting in the input bridge, providing the possibility of soft switching for the transistors. This gives lower switching losses but a more complicated control for the input bridge and higher conduction losses during the off-state. However, since the leakage inductance of the transformer is small, there will just be soft switching of the leading leg of the input bridge [24, 28]. The lagging leg will be hard switched since the energy stored in the leakage inductance is not enough to achieve soft-switching of the transistors. In this first comparison, the phase shift control is used to lower the switching losses.

The single active bridge converter in Fig. 3.2 looks similar to the fullbridge converter but due to the voltage stiff output it behaves differently and accordingly it is controlled in a different way [29]. Here, the output filter creates a voltage stiff output and the current waveforms in the converter are dependent on the voltage across the leakage inductance L_s of the transformer. Here, the current in the transformer increases during the on-state and then decreases during the off-state. Consequently, there is a triangular current waveform in the transformer and the switches turn off at the peak current, resulting in high switching losses.

For the resonant converter shown in Fig. 3.3, the switching losses are reduced by switching at zero current and/or zero voltage. This is achieved by the resonant tank consisting of the inductance L_r and the capacitances C_r and C_p as shown in detail in [30]. However, there are some disadvantages with the load resonant converters. The need of a wide frequency range makes the dimensioning of passive components difficult [31], and resonant converters also have the disadvantage of a large resonant inductance and capacitance [22].

Resonant operation is used in [12], where a three-phase series resonant converter is designed for the operation in a wind farm.

3.2.2 Operating Conditions in the DC Based Wind Farm

When comparing the topologies, they must be designed and evaluated for the same operating conditions. Therefore, the operating conditions are described for a local wind turbine grid with 5 turbines of 5 MW each. The average losses are calculated depending on the average wind speed [24, 25] and are then used for the evaluation of the converter topologies.

The operating conditions in a DC based wind farm depend both on the produced power and voltage from a wind turbine as well as the control strategy for the voltage levels in the internal grid for the wind farm. As shown in Section 2.3.1, the wind turbine with a DC output in Fig. 3.4 looks similar to the standard full power converter variable speed wind turbine with an AC output. However, the electrical system is different since the DC/DC converter has replaced the inverter towards the grid. The purpose of the DC/DC converter in the wind turbine is mainly to increase the rectified voltage to a level suitable for the local wind turbine grid.

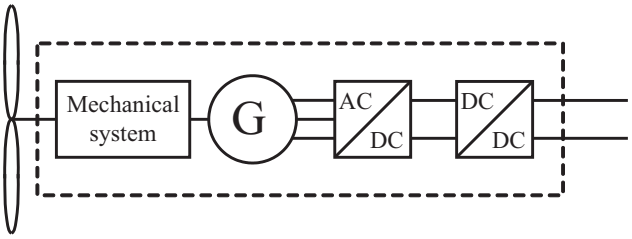

Fig. 3.4 Block diagram of the wind turbine with a DC-output.

The output voltage and output power from the rectifier in the wind turbine depend on the wind speed, the type of generator and the control strategy. In a variable speed wind turbine, the ratio between the wind speed and the rotational speed of the turbine is kept constant at low wind speeds, until the rated speed of the turbine is reached, and after this the speed is kept constant. The adjustment of the rotational speed according to the wind conditions at low wind speeds is made in order to convert as much wind energy into mechanical (shaft) energy as possible. In Fig. 3.5 a) the output power from the rectifier is shown and Fig. 3.5 b) shows the output voltage. The figure shows that for this turbine, the cut-in wind speed is 4 m/s, the rated rotational speed is reached at 10 m/s and the maximum power is obtained at 12 m/s.

Two different electrical systems are considered for the generator; the rectifier could either be a diode rectifier or an IGBT rectifier. Using a high efficiency diode rectifier, the output

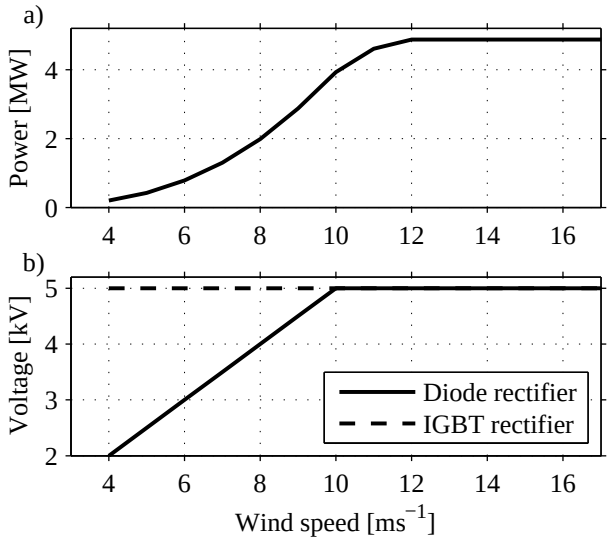

Fig. 3.5 Output from the wind turbine rectifier. a) power and b) voltage.

voltage of the rectifier is assumed to be proportional to the speed of the generator while the controllable IGBT rectifier gives a constant output voltage as seen in Fig. 3.5. The output voltage for the diode rectifier is assumed to be 2 kV at 4 m/s and 5 kV at 10 m/s and constant at 5 kV for the IGBT rectifier.

Knowing that the input voltage to the DC/DC converter can be either between 2 kV and 5 kV or constant 5 kV depending on the rectifier used, the operating conditions can be found for the converters. To obtain the operating conditions for the DC/DC converters for different control methods for the internal voltage levels in a wind farm, a local wind turbine grid for five turbines is used as shown in Fig. 3.6. There are three different positions for the wind turbine converter, positions 1a, 2a and 3a with the input and output voltages shown in Fig. 3.6 and described in detail in [24]. The operating conditions for these three positions in the local wind turbine grid will be used in the evaluation of the DC/DC converters. For position 1a, the diode rectifier is used giving an input voltage to the DC/DC converter between 2 kV and 5 kV while the output voltage is constant 15 kV. The diode rectifier is also used for position 2a, but for this position the output voltage is varying between 6 kV and 15 kV, and is proportional to the input voltage. For position 3a, the IGBT rectifier is used resulting in a constant input voltage of 5 kV and also the output voltage is constant at 15 kV. Consequently, the converters at positions 2a and 3a have a constant ratio between the input voltage and the output voltage. For position 3a these voltage levels are fixed and for position 2a the voltage levels are proportional to the rotational speed of the generator. The converter at position 1a has to compensate for the voltage variations and thereby has a varying ratio between the input voltage and the output voltage. In the same way for the main DC/DC converter, positions 1b and 3b have

identical operating conditions with constant voltage levels both for the input 15 kV and the output 75 kV. For position 2b, the input voltage is varying between 6 and 15 kV while the output is constant 75 kV.

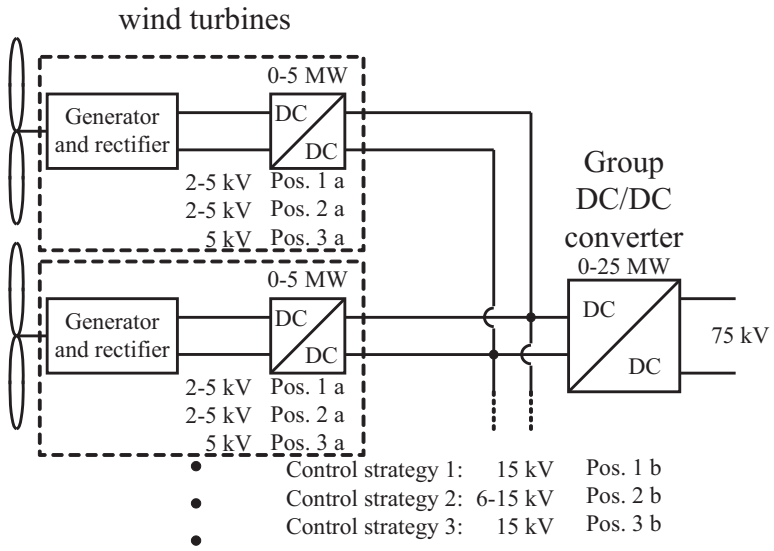

Fig. 3.6 The local wind turbine grid with voltage levels.

3.2.3 Loss Calculations

The losses are first calculated for each position as a function of the wind speed. After that, the losses are integrated over the probability distribution of the wind speed to achieve the average value of the losses.

There are two main components of the losses that are expected to vary between the topologies; the losses in the semiconductor components and the losses in the transformer. The losses in the input and output filters are not considered since the design of the filters is dependent on the requirements for the local grid. The losses are calculated using the operating conditions obtained from current and voltage waveforms from simulations with ideal components together with known data for the components. For the IGBT module, data for losses during hard-switching is found in the data sheet [32] and data for switching losses during soft-switching conditions is found in [33]. For the diode module, the losses are found in the data sheet for the component [34].

The transformer losses include both copper losses and core losses. The copper losses are calculated from the rms-current and the resistance of the transformer windings at the

operating frequency. Here, the skin effect is considered and an AC-resistance coefficient is used as shown in [35, 36]. For reducing the copper losses, a foil winding is used for the primary winding and a Litz-wire is used for the secondary winding.

In [30, 35, 37] a general expression for the core losses in the case of a sinusoidal voltage exciting the core is stated as

$$P_{core} = K_1 f_{tr}^{K_2} (B_{max})^{K_3} V_{core}. \tag{3.1}$$

Here the core loss P_{core} is a function of the peak value of the ac flux density B_{max} and the switching frequency f_{tr}. Further, K_1, K_2 and K_3 are constants that vary between the materials and V_{core} is the volume of the core. For the chosen core material of amorphous metal, the constants are K_1 = 46.7, K_2 = 1.51 and K_3 = 1.74 [38]. However, loss coefficients are often provided from the manufacturer of the core only for sinusoidal excitation. For non sinusoidal excitation, the core losses can be given by

$$P_{core} = \frac{1}{\tau} K_1 f_{eq}^{K_2 - 1} (B_{max})^{K_3} V_{core} \tag{3.2}$$

assuming no temperature dependence of the core losses [36, 39]. Here, τ is the switching period and f_{eq} is the equivalent frequency. The calculation of the equivalent frequency f_{eq} is shown in [36, 39].

3.2.4 Resulting Losses for the Different Topologies

Here, the resulting losses are shown for the three different topologies based on the method for loss calculations described above. For the different operating conditions shown in Fig. 3.6, the resulting losses are obtained for an average wind speed of 7.2 m/s as described in Section 2.4, and the resulting losses are shown in Fig. 3.7.

As can be seen in the figure, the resonant converter and the fullbridge converter have the lowest losses of the three topologies, while the single active bridge converter has higher losses. The variable operating conditions create problems for all three converters including increased losses compared to a converter designed for a single operating point [24, 25]. The single active bridge converter is most affected by the wide range of operation, where the large change of duty cycle, or increased switching frequency, causes an increase in the losses. This is due to the fact that the change of duty cycle is caused both by variations in power and voltage levels, resulting in large variations for all positions in the local wind turbine grid. For the fullbridge converter, the change of duty cycle is just caused by the variations in voltage levels. Both the fullbridge converter and the single active bridge

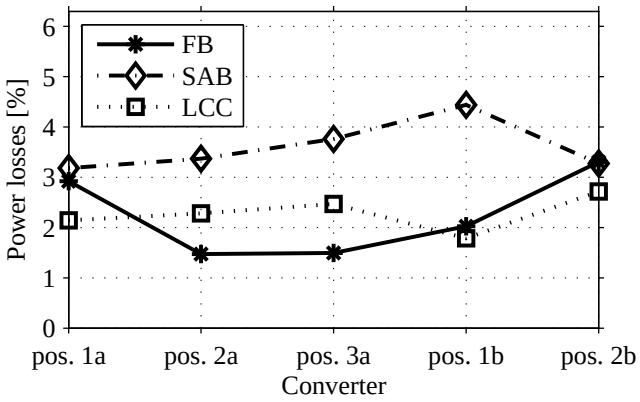

Fig. 3.7 Loss comparison for the different topologies.

converter suffer from the large power variations since it leads to a limitation of the snubber capacitors. The resonant converter has no significant increase in the losses due to the large range of operating conditions, but the stresses for the input and output filters are large for operation at low power levels. Also, an issue with the resonant converter is that the peak voltage for the transformer is considerably higher than the input voltage to the converter since the transformer is a part of the resonant tank. Considering the losses, the contribution to the energy production cost, simple design and easy control, the fullbridge converter is found to be a suitable choice for the wind farm application [24, 25].

3.3 Design Aspects for the Fullbridge Converter

When the fullbridge converter has been chosen as the suitable topology, the design and control are investigated further. First, two different control strategies are investigated and then the design of the transformer as well as the semiconductor components are chosen.

3.3.1 Choice of Control Strategy

For the fullbridge converter, both hard switched operation and soft switched phase shift operation have been extensively studied [26, 31, 40]. There are several suggestions to achieve soft switching in a large operating range, including auxiliary circuits and different control techniques. Also, in [41] it is shown that the semi-soft switching fullbridge converter has a slightly higher efficiency than the soft switching fullbridge converter. However, using the soft-switching operation of the converter, it is shown in Fig. 3.7 that there are high losses for the converters that have to compensate for voltage variations in a wind farm. Here, the hard switching duty cycle control is compared to the soft switching phase shift control. Comparing the losses using duty cycle control and phase shift control,

the results can be found in Fig. 3.8 and are also shown in detail in [42].

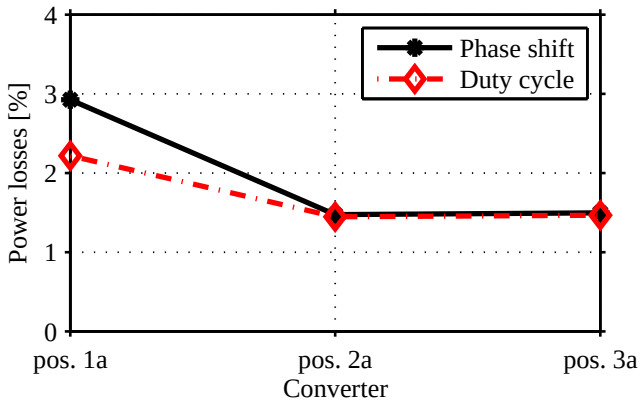

Fig. 3.8 Average losses for the average wind speed 7.2 m/s.

It can be seen that for positions 2a and 3a, the losses are similar for the two control methods, but for position 1a, the duty cycle control results in lower losses. The loss distribution for position 1a is shown in Fig. 3.9 for both duty cycle control and phase shift control.

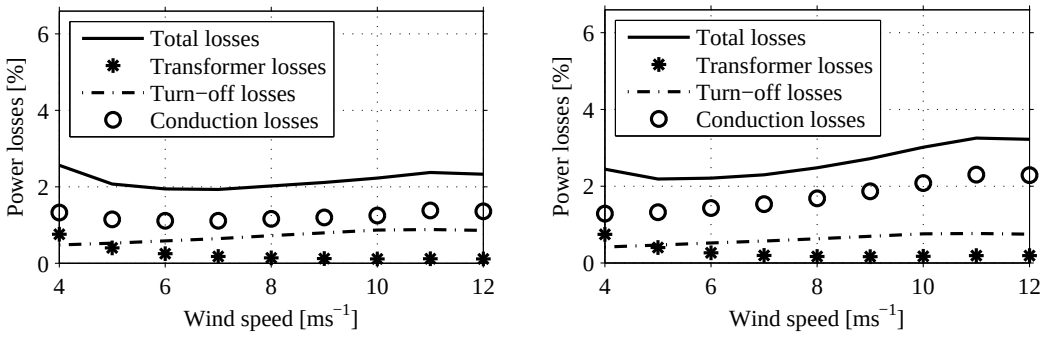

(a) Duty cycle control. (b) Phase shift control.

Fig. 3.9 Loss distribution for position 1a.

In the figure, a clear difference in the losses can be seen for the two control methods; the duty cycle control results in lower conduction losses but higher switching losses compared to the phase shift control. The converter using phase shift control has lower turn-off losses due to the snubber capacitor connected across the transistors. However, since just the leading leg is soft switched, the reduction in the turn-off losses due to the soft switching operation is limited. On the other hand, the conduction losses during the off-state are higher for the phase shift control. Using the duty cycle control, the current only

flows through the rectifying bridge at the off-state. For the phase shift control, during the off-state the current will flow through the output bridge, the transformer as well as one transistor and one freewheeling diode in the input bridge. This will lead to larger conduction losses in the case of the phase shift control at low duty cycle. Regarding the average losses, the increase in conduction losses for the phase shift control is significantly larger than the reduction of turn-off losses by the snubber capacitors for position 1a. For the converter at this position, the duty cycle is lowered at high wind speeds leading to a large difference in conduction losses between the control methods. For positions 2a and 3a, the losses are equal for the control methods as seen in Fig. 3.8. Resulting from the constant transformation ratio, the off-state is short for the converters at positions 2a and 3a. Here, the decrease in switching losses for the phase shift control compared to the duty cycle control is similar to the increase in conduction losses.

3.3.2 Choice of Switching Frequency and Transformer Core Material

The choices of switching frequency for the converter and core material for the transformer are important for the performance of the DC/DC converter. The switching frequency is a trade-off between low losses for the converter and low weight of the transformer as shown in Fig. 3.10 for the converter with constant voltage levels.

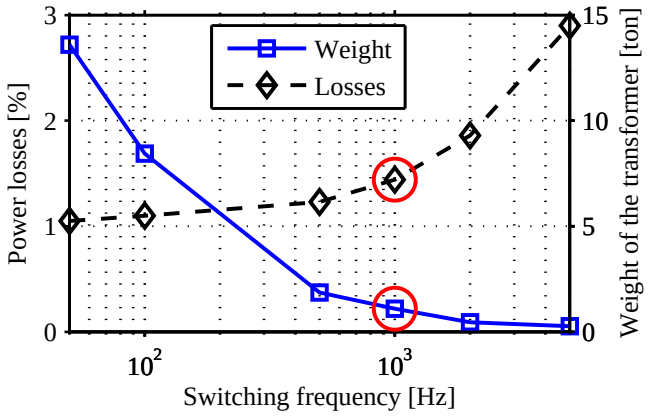

Fig. 3.10 Total converter losses vs. transformer weight for different switching frequencies.

At low switching frequencies, the conduction losses for the semiconductor components are the dominating losses followed by the losses in the transformer. As the switching frequency increases, these losses are fairly constant while the switching losses increase. Consequently, at a certain switching frequency, the total losses increase considerably due to the increasing switching losses, and it is found to be at approximately 1 kHz, depending

on the operating conditions of the converter. Since the size of the transformer is reduced with increasing switching frequency, a suitable value will be 1 kHz, where the transformer is as small as possible keeping fairly low total losses of the converter. As seen in Fig. 3.10, the weight of the 1 kHz transformer is approximately 10 % of the weight of the 50 Hz transformer. Also in [12], 1 kHz is found to be a suitable switching frequency. In [13], it is stated that the estimated weight of a 1200 Hz transformer is 8 % of a comparable 50 Hz transformer for 3 MW. Since the weight is critical for the components in a wind turbine [13], and the transformer losses are a small fraction of the total losses in the converter at high wind speeds (as shown in Fig. 3.9), the design of the transformer aims at a low weight (considering the constraint of a maximum leakage inductance for the 1 kHz transformer).

Regarding the core material of the transformer, a laminated steel core gives considerably higher losses than a core made of an amorphous metal alloy for medium frequency transformers. In [30], it is stated that laminated steel is used for low-frequency applications (below 2 kHz) due to the high core losses. A core of amorphous metal alloys gives lower losses, but the saturation flux density is slightly lower, and is then preferably used for medium frequencies. For high frequencies (above 10 kHz), ferrites is a suitable choice with lower losses [30, 43]. However, for the medium frequency transformer, the considerably lower saturation flux density for the ferrites gives a considerable increase in the size of the transformer [44]. Also in [37], it is stated that, for a 4 kHz transformer, amorphous and nanocrystalline core materials are more suitable than ferrites due to their high saturation flux and mechanical strength. Materials consisting of amorphous metal alloys are also used for the transformers shown in [12, 13] with switching frequencies at $\sim$1 kHz and power ratings of 3-5 MW.

3.3.3 Choice of IGBT Modules

Due to the high power rating of 5 MW and voltage levels of 5 kV at the input and 15 kV at the output for the DC/DC converter in a wind turbine, there are large stresses for the components. The semiconductor components used in this investigation are IGBT modules with rated voltage 3300 V and rated current 200 A for the input bridge. These IGBT modules were chosen since there is available loss data for soft-switching conditions [33]. For the output bridge, a diode with rated voltage 2500 V and rated current 2000 A is used. For the IGBT components, it is assumed that one module consists of 10 parallel connected devices with 200 A each, resulting in a total current rating of 2000 A.

However, there are also press-pack IGBT modules that are designed for series connection [45]. The losses for the converters using the IGBT module described in [33] (IGBT module 1) and the press pack IGBT module (IGBT module 2) are shown in Fig. 3.11.

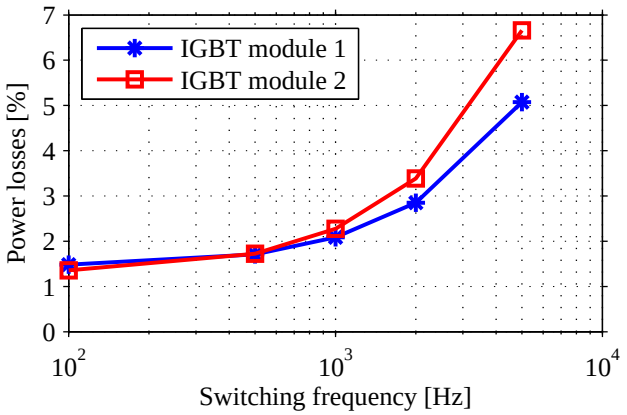

Fig. 3.11 Converter losses for position 1a, using duty cycle control and two different IGBT modules.

Here, it can be seen that the press pack IGBT has lower conduction losses but higher switching losses, which results in low losses at low switching frequencies and higher loses at high switching frequencies. However, for the used switching frequency 1 kHz, the losses are similar and both modules can be used.

3.3.4 Comments on the High Voltage Design Aspects

The high power, high voltage DC/DC converters described in this chapter have the same principle of operation as low power, low voltage DC/DC converters. However, there are of course a number of design issues that must be given further consideration when increasing the power and voltage ratings of the DC/DC converters.

Due to the high voltage, semiconductor components with high voltage (above 2.5 kV) must be connected in series. However, even if the blocking voltage is limited for each semiconductor module, the insulation towards ground is an important issue that must be solved [46]. Additionally, if the semiconductor components are connected in series, the voltage slope during the switching must be decreased and snubbers must probably be used. Here, both the semiconductor components and the switching frequency is similar as for the VSC HVDC stations [2, 47]. Therefore, it is assumed that the design of suitable switching valves is possible.

Also the high power, medium frequency transformer for these sizes and voltage levels is a component that has to be developed further before these DC/DC converters can be realized.

3.4 Experimental Verification of the Loss Calculations

To verify the calculation method for the losses as well as the simulated waveforms, a down scaled experimental setup is used. Here, the measured waveforms and losses are compared to the results from the simulations and loss calculations that are performed in the same way as for the full size converters for the wind farm application.

The design of the fullbridge converter aims to construct a down scaled converter suitable for tests that can be compared with simulations. It should be large enough to have similar characteristics as the full scale converter, but on the other hand it should be small enough to be realized using the existing laboratory equipment. The resulting converter is described in detail in [48] and will here be presented briefly. A photo of the experimental setup is shown in Fig. 3.12.

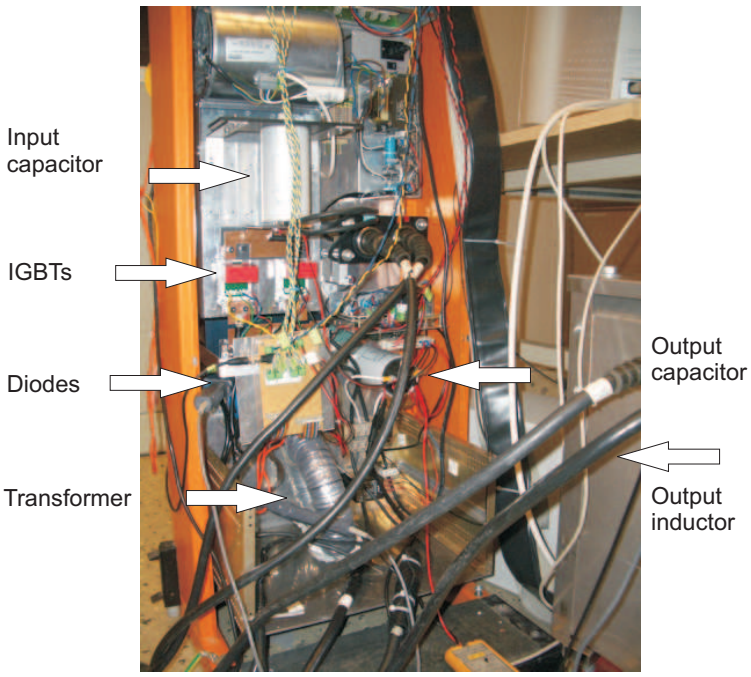

Fig. 3.12 Photo of the experimental setup.

The power rating of the converter is 9 kW with an input voltage of 300 V and an input current of 30 A. The transformer of the converter has the ratio 1:1, which gives the maximum theoretical output voltage of 300 V. In reality, the output voltage is slightly lower due to losses in the converter and also the loss of duty cycle. The main components of the converter are the IGBT modules for the input bridge, the diode modules for the rectifying bridge, the transformer, the filter inductance and capacitances as well as the control system. Additionally, there are auxiliary components such as the driver circuits, the measuring system, the cooling and the power supply to the auxiliary components.

3.4.1 Semiconductor Components

The IGBT modules used in the input bridge are the SemixS302GB128D modules from Semikron with rated voltage 1200 V and rated current 320 A. As drive circuits for the IGBT modules, two *Skyper*^{TM}32*Pro* from Semikron are used. They are mounted on the corresponding evaluation boards *EvaluationBoard*1*Skyper*^{TM}32*Pro*.

For the rectifying bridge the SGS - ThomsonMicroelectronics BYT230PIV - 1000 modules are used with a rated voltage of 1000 V and a rated current of 30 A. However, using the rectifying bridge without over-voltage snubbers results in large oscillations at turn-off close to the maximum voltage for the diodes. To reduce these oscillations RC-snubbers are inserted across each diode with the values R_{sn} = 60 Ω and C_s = 2.8 nF.

3.4.2 Transformer

The transformer used is a custom-made transformer with transformation ratio 1:1 which can be seen in Fig. 3.13. From the measurements of the transformer voltage and current, the stray inductance is determined to 10 μH and the main inductance to 14 mH. Further, the core material is the iron based magnetic alloy 2605SA1 from Metglas. However, it should be noted that the core material is no-field anneal and the given data for core losses in the data sheet is based on a core with longitudinal field anneal. In order to achieve the desired operation for the phase shift control, an additional inductance of 52 μH is inserted in series with the transformer.

3.4.3 Filter Components

As the input capacitor, a *Rifa Elyt Long Life PEH*169*UV*439*AQ* capacitor is used with the capacitance value of 3900 μF. In the output bridge, a *Rifa Elyt Long Life PEH*169*UV*433*OQ* capacitor with 3300 μF is used. The real value of the capacitance has a large possible deviation from the rated value, which is - 10 %/+ 30 %. This makes no difference for the loss calculations in steady state, but for the dynamic control of the load voltage, the value of the output capacitor is significant. Here, it is found that the output capacitor has an approximate capacitance of 4000 μF, which is 21 % above the rated value. Since the full-bridge converter requires a current-stiff output, the output filter inductance needs to be large, especially since the switching frequency is as low as 1 kHz. The inductance chosen was an existing free-standing inductor of 20 mH that can handle a current up to 80 A.

Fig. 3.13 Photo of the transformer.

3.4.4 Control System and Measurements

For generating the control signals for the drive circuits, a Simulink/MATLAB file is used where the control signals are generated from the phase shift determined by the user. Further, the control signals are connected to the drive circuits via a dSPACE DS1103 controller board and two additional cards for obtaining the right voltage levels for the control signal to the drive circuits.

The measurements for the circuit are done in two different ways, either by an oscilloscope or by using a measuring card and feeding the measured signals back to the dSPACE system. The dSPACE system has the drawback of a limited bandwidth since the sampling time is 50 μs, and therefore, the high-frequency signals are measured with the oscilloscope. However, the input and output voltages are measured with the dSPACE system via a voltage transducer card. In the same way, the input and output currents are measured using LEM-modules and a measuring card, described in [48], together with the dSPACE system.

3.4.5 Stray Resistances

In [24], where the waveforms from the experimental model were compared to the waveforms from a simulations model, it was found that some stray components were needed

to give an accurate representation of the circuit. In this non-ideal simulation model, some loss components are included in the circuit. The ideal simulation model is modified by adding non-ideal switches, and also including the resistances of the transformer and the output filter. Finally, the resistances across the input and output capacitors are added. The added resistances can be seen in Fig. 3.14 and the values of the components are shown in Table 3.1. For the bleeder resistances R_{Cin} and R_{Cload}, the values are known and for the transformer and the filter inductance, the resistance values R_{Ls} and R_{Lload} are measured at 1 kHz for the transformer and at DC current for the filter. However, the value of the resistance for the filter inductance is increased from the measured 37.6 mΩ to 50 mΩ for obtaining the AC resistance.

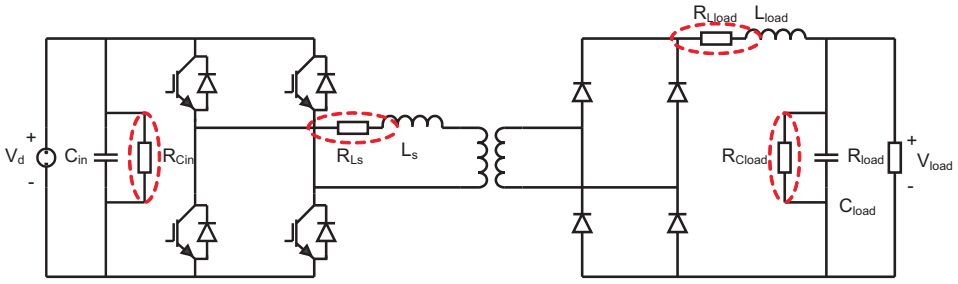

Fig. 3.14 Non-ideal simulation model for the experimental converter.

Table 3.1: Calculated losses for the simulated circuit.

Component	Resistance
R_{Cin}	47 kΩ
R_{Cload}	10 kΩ
R_{Ls}	72 mΩ
R_{Lload}	50 mΩ

3.4.6 Verification of the Loss Calculations

Starting with the measured waveforms, the input and output waveforms for the transformer are compared to the simulated waveforms in Fig. 3.15. For the simulations, the model shown in Fig. 3.14 is used.

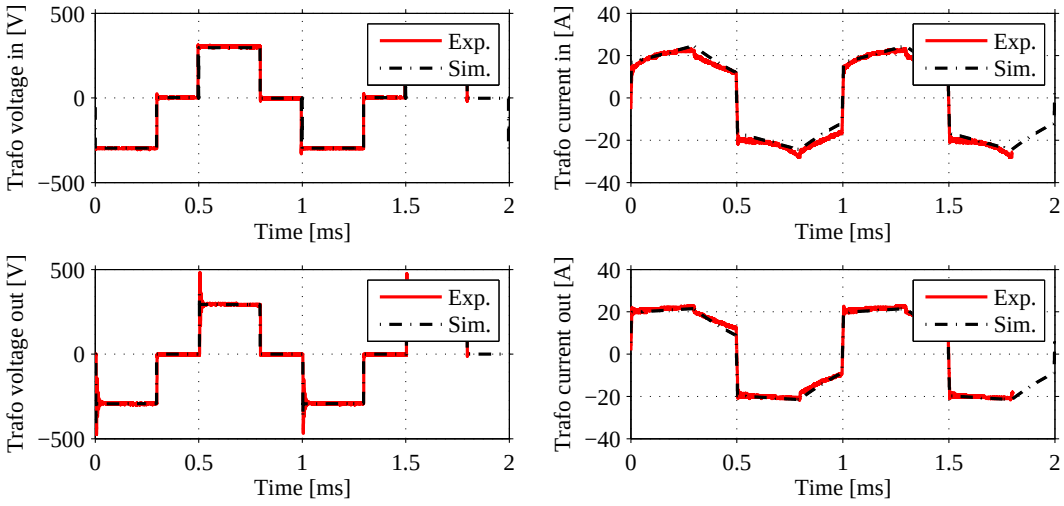

(a) Voltage waveforms.

(b) Current waveforms.

Fig. 3.15 Measured and simulated current and voltage waveforms at the input and output of the transformer.

In the figures, it can be seen that the measured and simulated waveforms are similar. There are some small deviations, but they should not have any significant impact on the loss calculations.

Continuing with the loss calculations, Fig. 3.16 (a) shows the calculated losses for the converter including the loss distribution for the duty cycle control. In Fig. 3.16 (b), the calculated losses are compared to the measured losses.

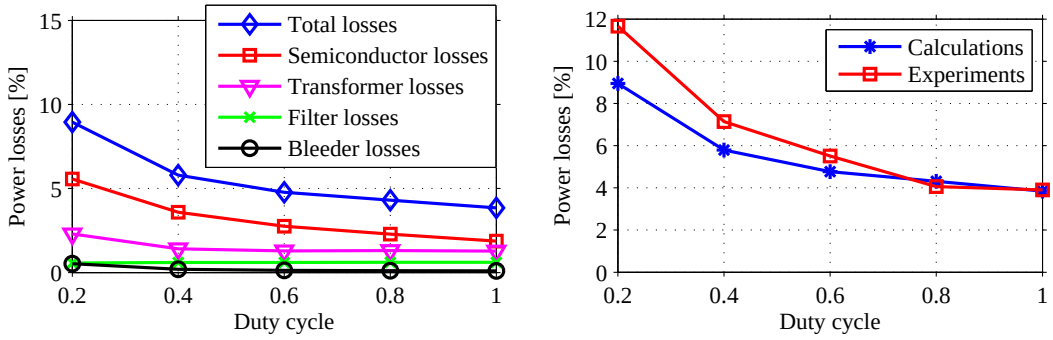

(a) Calculated loss distribution.

(b) Calculated total losses compared to the measured losses.

Fig. 3.16 Calculated total losses and loss distribution compared to the total measured losses.

It can be seen that the major contributions to the losses are the losses in the semiconductor

components and in the transformer, which are the losses used in the loss calculations for the full scale converter. Regarding the comparison between the calculated losses and the simulated losses, it can be seen that they are similar at high duty cycles, but at low values of the duty cycle the measured losses slightly exceed the calculated losses. For comparing the losses for the different control methods, Fig 3.17 shows (a) the measured losses and (b) the calculated losses for duty cycle control and phase shift control.

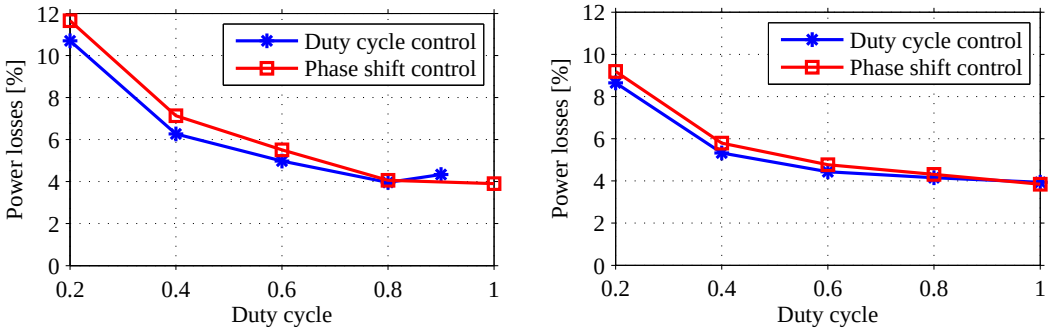

(a) Measured total losses.

(b) Calculated total losses.

Fig. 3.17 Calculated and measured total losses for both duty cycle control and phase shift control.

It can be seen that the difference in losses between the control methods is approximately the same for both the measured losses and the calculated losses.

3.5 Summary

In this chapter, the high power medium frequency DC/DC converters have been studied for the wind farm application. Three different topologies were evaluated and it was found that the fullbridge converter with a current stiff output filter is the most suitable topology. For this topology, a suitable switching frequency is 1 kHz, where the weight of the transformer is reduced by 90 % compared to a 50 Hz transformer and the losses are reasonably low. It was also found that, in the case of varying voltage levels, the hard switching control gives lower losses than the soft switching phase shift control. Finally, the loss calculations were verified using a down scaled experimental setup.

Chapter 4

Design and Loss Evaluation of the Wind Farm with a DC Grid

4.1 Introduction

Before evaluating the wind farm with a DC collection grid and finding the system performance and suitable control strategies, the design of the wind farm must be determined. In this chapter, the layout of the wind farm is determined as well as the designs for the components, using the chosen design of the DC/DC converters from Chapter 3. Further, the losses for the DC collection grid are calculated.

4.2 Chosen Layout of the Wind Farm

The layout of the wind farm investigated in this thesis is chosen to be similar to the wind farm Lillgrund as shown in [21]. The Lillgrund wind farm consists of 48 wind turbines with rated power 2.3 MW each [21], and the turbines are connected with an internal 33 kV AC grid as shown in Fig. 4.1. In the wind farm, the voltage is increased to 33 kV AC by a transformer in each wind turbine and there is one main transformer at platform W-01 that transforms the 33 kV voltage in the internal grid to the 130 kV transmission voltage. Further, in this study it is assumed that the distance between the turbines is 500 m.

The wind farm with an internal DC grid used in this study has the same layout as the AC based wind farm, but the AC cables are replaced with DC cables and the transformers are replaced with DC/DC converters. The internal voltage level is 32 kV DC and the voltage level for the HVDC transmission line is 130 kV DC. The main electrical components of the wind farm can be represented by the equivalent circuit shown in Fig. 4.2.

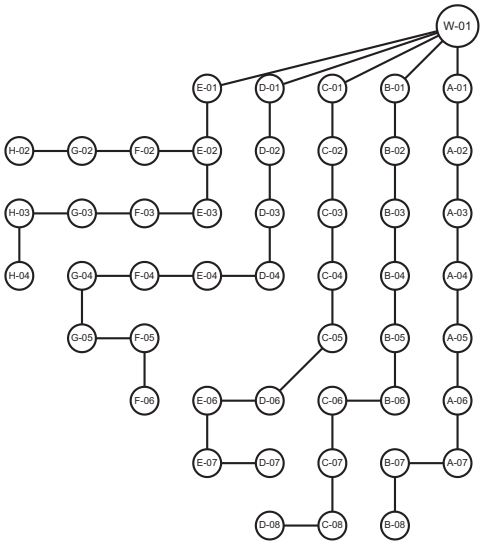

Fig. 4.1 The layout of the internal grid at Lillgrund.

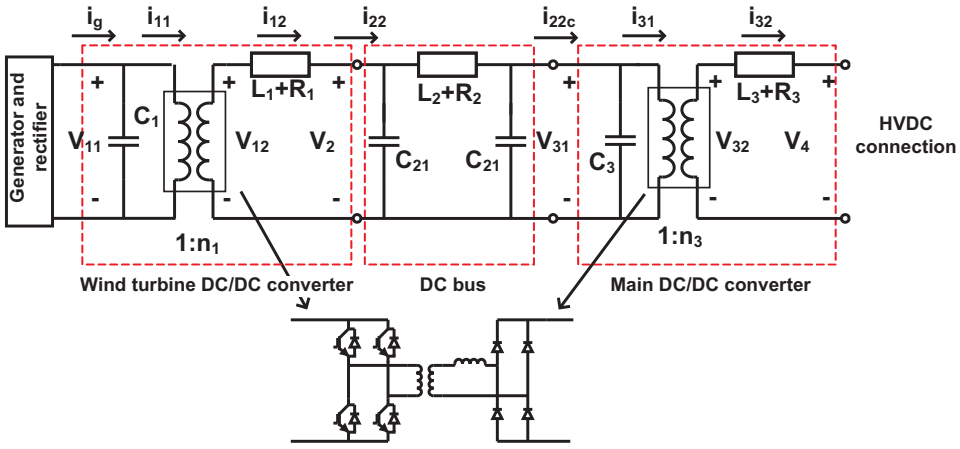

Fig. 4.2 The equivalent circuit of the internal DC grid.

Here, one wind turbine, including the generator and the rectifier, is connected to the wind turbine DC/DC converter that transforms the voltage to 32 kV for the internal grid. The DC/DC converter is here simplified to a variable transformer (representing the inverting fullbridge, the medium frequency transformer and the diode rectifier) and the input and output filters for the converter. The converter is then connected to the internal DC bus together with several other wind turbines as shown in Fig. 4.1. The internal DC cables are then connected in parallel to the main DC/DC converter that increases the voltage level to 130 kV suitable for the HVDC connection.

4.3 Design of the Components in the Wind Farm

For the wind farm with an internal DC grid, the main components are the wind turbines, the DC/DC converters and the DC cables.

4.3.1 Wind Turbines

In the wind farm Lillgrund, 2.3 MW wind turbines with full power converters are used [21]. The electrical layout of these wind turbines is shown in Fig. 4.3.

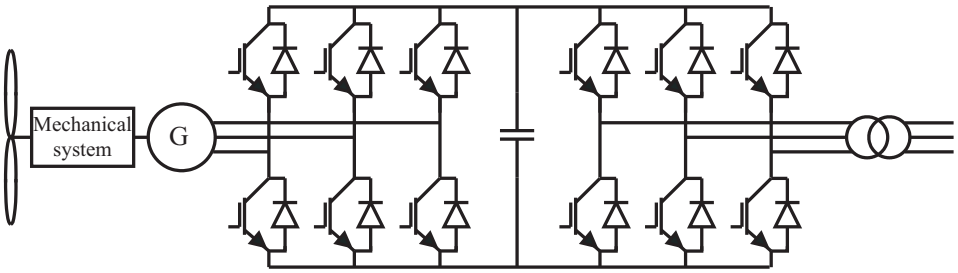

Fig. 4.3 AC wind turbine with a full converter system.

In the investigated wind farm with a DC collection grid, the output voltage to the internal grid should be a DC voltage instead of an AC voltage. To achieve this, the electrical layout of the turbine shown in Fig. 4.4 is used.

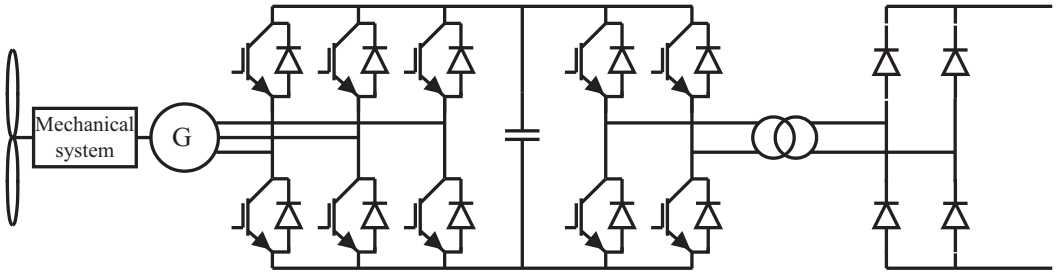

Fig. 4.4 Wind turbine with a DC output.

In the DC wind turbine, the three phase inverter and the 50 Hz transformer are replaced with a DC/DC converter. In the DC/DC converter, a fullbridge inverter gives a medium-frequency square-wave voltage that is transformed to the required voltage level by the medium frequency transformer. On the secondary side of the transformer, a diode bridge rectifies the output voltage.

Comparing the AC turbine with the DC turbine, it can be seen that the mechanical system, the generator and the rectifier are the same for both turbines. The main advantage for

the DC configuration is that the transformer is smaller since the switching frequency is $\sim$1 kHz instead of 50 Hz. The disadvantage is the additional diode bridge that is needed at the output to rectify the voltage.

The generator in the wind turbine is a 2.3 MW induction generator with 690 V output voltage, with the equivalent circuit shown in Fig. 4.5, and the parameters given in Table 4.1 [49]. The output voltage from the three-phase rectifier, which is the voltage at the DC-link, is assumed to be constant 1.5 kV.

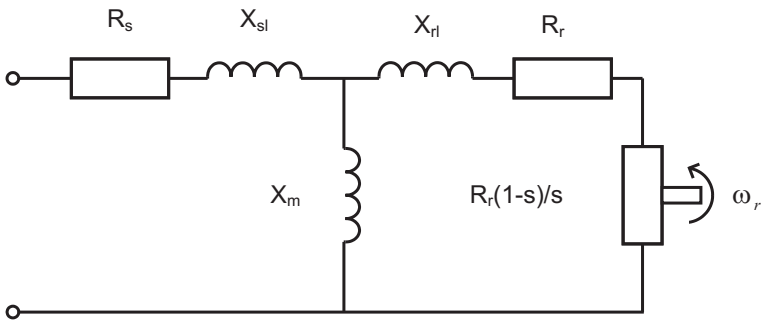

Fig. 4.5 Equivalent circuit for the induction generator.

Table 4.1: Parameters for the induction generator.

Parameter		Value	unit
Stator resistance	R_s	0.005	pu
Stator leakage reactance	X_{sl}	0.09	pu
Magnetizing reactance	X_m	3.3	pu
Rotor resistance	R_r	0.008	pu
Rotor leakage reactance	X_{rl}	0.1	pu

4.3.2 Cables

In [21], it can be seen that the internal grid for the wind farm has a voltage level of 33 kV. Further, the cross sectional area of the 33 kV cable depends on the location in the wind farm. For the first 6 wind turbines the cable has a smaller area than for turbine 7-9. Also, the connection between the last turbine and the offshore substation has a larger diameter

due to the mutual heating of the cables inside the gravity foundation [21].

In a similar way, the DC cables are dimensioned depending on the location in a wind farm, where the voltage level is 32 kV DC. For the first 6 turbines, the maximum current is 431 A, at turbine 9 the maximum current is 650 A and for all 10 turbines 720 A. Choosing a single core copper cable, the resulting cross sectional conductor areas are 185 mm^2, 400 mm^2 and 630 mm^2 respectively. For the HVDC cable, the resulting diameter of the cable is 630 mm^2.

A cable segment can be modeled with the π-link model as shown in Fig. 4.6 [17]. When choosing the voltage rating for the cables, the ground faults must be considered. During normal operation, the mid point grounding will give $\pm$16 kV for the DC bus. However, in the case of a ground fault, the potential can increase rapidly to 32 kV for a conductor. Therefore, the voltage rating for the cables should be the line-to-line voltage, which is 30 kV nominal voltage (maximum 36 kV) for the DC bus and 130 kV nominal voltage for the HVDC link.

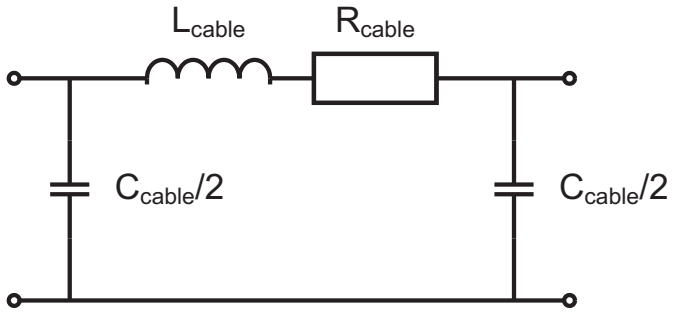

Fig. 4.6 π-link model for the cable.

When simulating and calculating the losses for the system, the cable parameters must be known. Starting with one cable, the values for the capacitance C_{ph} for one cable can be found in the data sheet of the cable as 210 nF/km, 280 nF/km and 340 nF/km respectively for the DC bus cable and 210 nF/km for the HVDC cable. Then, the cable capacitance C_{cable} for both cables can be obtained as

$$C_{cable} = \frac{C_{ph}}{2}. \tag{4.1}$$

The resistance R_{ph} of one cable is calculated using the resistivity ρ for copper as well as the cross sectional area A and the length l of the conductor as

$$R_{ph} = \frac{\rho}{A} l. \tag{4.2}$$

The resulting resistances are 84 mΩ/km, 40 mΩ/km and 24 mΩ/km for the DC bus cable and 23 mΩ/km for the HVDC cable. The total resistance R_{cable} in the π model is then the sum of the resistance ni the two cables.

$$R_{cable} = 2R_{ph}. \tag{4.3}$$

The total inductance L_{cable} of two parallel wires can be calculated using [50]

$$L_{cable} = \frac{\mu_0}{\pi}\left(\frac{1}{4} + \ln\frac{d}{r}\right), \tag{4.4}$$

where d is the distance between the centers of the two conductors and r is the radius of the conductors. Assuming that the cables are located next to each other, the resulting inductance values are 0.77 mH/km, 0.69 mH/km and 0.64 mH/km for the DC bus cable and 0.74 mH/km for the HVDC cable. Finally, the cable parameters are summarized in Table 4.2.

Table 4.2: Parameters for the ±16 kV DC bus and the ±65 kV HVDC connection.

Conductor area	R_{cable}	L_{cable}	C_{cable}
185 mm^2	168 mΩ/km	0.77 mH/km	105 nF/km
400 mm^2	79 mΩ/km	0.69 mH/km	140 nF/km
630 mm^2	48 mΩ/km	0.64 mH/km	170 nF/km
HVDC			
630 mm^2	47 mΩ/km	0.74 mH/km	105 nF/km

For the HVDC link, a capacitor of 50 μF is connected to each end of the cable. The values for these capacitors are determined by the fault ride through properties shown in Section 7.2. The length of the HVDC cable is assumed to be 40 km.

4.3.3 DC/DC Converters

There are two different designs for the DC/DC converter to be used in the chosen layout for the DC based wind farm, the DC/DC converter in the wind turbine and the main DC/DC converter for the whole wind farm. As was seen in the previous section, the generator is connected via an IGBT based rectifier giving a constant output voltage. Consequently, both converters have fixed voltage levels, the converter in the wind turbine should

increase the voltage level from 1.5 kV to 32 kV and the main DC/DC converter should increase the voltage from 32 kV to 130 kV.

When choosing the voltage ratios for the transformers in the DC/DC converters, the limitation for the converter to step down operation should be considered. Therefore, the transformer ratio should be chosen so the converter can be controlled in case of the lowest possible input voltage and the highest possible output voltage. Having a maximum steady state deviation in the voltage of ± 5 % from the nominal voltage level, it is assumed that the peak voltage deviations are within ± 10 % of the nominal voltage. Also, assume that there is a loss of duty cycle of 10 % due to the time for current reversal in the leakage inductance in the transformer. Consequently, for the nominal input voltage V_{in} and output voltage V_{out}, the transformer ratio n are calculated as

$$n = \frac{1.1 \cdot V_{out}}{0.9 \cdot 0.9 \cdot V_{in}}. \tag{4.5}$$

Using the nominal voltage levels 1.5 kV for the DC link in the wind turbine, 32 kV for the DC bus and 130 kV for the HVDC connection, the resulting transformer ratios are 29 for the wind turbine converter and 5.5 for the main converter. The steady-state duty cycle for nominal voltage levels will then be 80 %. The ratings for the current and voltage for the converters are summarized in Table 4.3.

Table 4.3: Parameters for the DC/DC converters.

	turbine converter	main converter
Rated power	2.3 MW	110 MW
Input voltage	1500 V	32 kV
Output voltage	32 kV	130 kV
Input current	1.5 kA	3.4 kA
Output current	72 A	850 A
Transformer ratio	29	5.5

The DC/DC converters are fullbridge converters with duty cycle control as described in Chapter 3. For the choice of IGBT modules, it was shown in Fig. 3.11 that there is no major difference in the losses, and the chosen IGBT module is then the 2.5 kV 2000 A press-pack module since it is designed for operating in parallel and series connections. Also, diode modules with the same power rating will be chosen. In Table 4.4, the maximum stresses for the semiconductor switches are shown (where the values for the currents

are the peak values).

Table 4.4: Maximum stresses for the semiconductor components.

	turbine converter	main converter
Transistor voltage	1500 V	32 kV
Transistor current	1900 A	4300 A
Diode voltage	44 kV	176 kV
Diode current	72 A	850 A

When choosing the number of semiconductor devises, the peak stresses for the components should be considered. The used semiconductor devices have the voltage rating 2.5 kV and the current rating 2 kA. For the converter in the wind turbine, 1.5 kV DC link voltage would require one 2.5 kV IGBT (or an IGBT with slightly higher voltage rating). For the current rating, the peak current is the same as the rated current, and therefore just one component is needed. However, to have redundancy in the case of the failure of an IGBT module, two IGBTs are connected in parallel to lower the current stresses and also allow continued operation in the case of a failure of a single IGBT module. For the diode bridge, it is assumed that each diode should withstand 1.25 kV, resulting in 34 series connected devices. Since the rated current is much smaller than 2 kA (just 72 A), only one diode is needed in parallel. For this diode, the current rating can be decreased to about 500 A, which is 25 % of the original current rating. For the main converter, it is also assumed that each component should withstand 1.25 kV in steady state to have some margin for transients and fault of a single component. The large number series connected devices gives a redundancy in the case of a failure of a single diode or transistor. Regarding the choice of failure mode for the devices, the components connected in series (all diodes and the transistors for the main converter) should fail to a short circuit and the transistors for the wind turbine converter should fail to open circuit. The number of modules needed for each switch are summarized in Table 4.5.

The parameters for the filter inductances for the converters are chosen to be L_1 = 0.3 H for the DC/DC converter in the wind turbine, and also L_3 = 0.3 H for the main DC/DC converter. The inductance is chosen to just achieve continuous conduction in the case of the lowest wind speed for the DC/DC converter in the wind turbine and for the main converter at 3 % of the rated power. For lower power levels, the converter will operate in discontinuous conduction mode. The values of the filter capacitors are determined in Section 6.3.2 and are C_1 = 152 mF for the wind turbine converter and C_3 = 11 mF for the main converter (plus additional 0.1 mF at the connection to each turbine). The transform-

Table 4.5: Number of semiconductor modules.

	turbine converter	main converter
Transistor series	1	26
Transistor parallel	2	3
Diode series	34	140
Diode parallel	0.25	1

ers are designed for the rated power and the resulting weight is 650 kg for the transformer in the wind turbine DC/DC converter and 28000 kg for the main DC/DC converter.

4.4 Loss Evaluation for the Wind Farm

For the wind farm with an internal DC grid, the parts that are different from a wind farm with an internal AC grid are the DC/DC converter in the wind turbine, the DC bus and the main DC/DC converter, which are shown in Fig. 4.7. Here, the steady state losses in the wind farm are calculated for these components for different operating conditions.

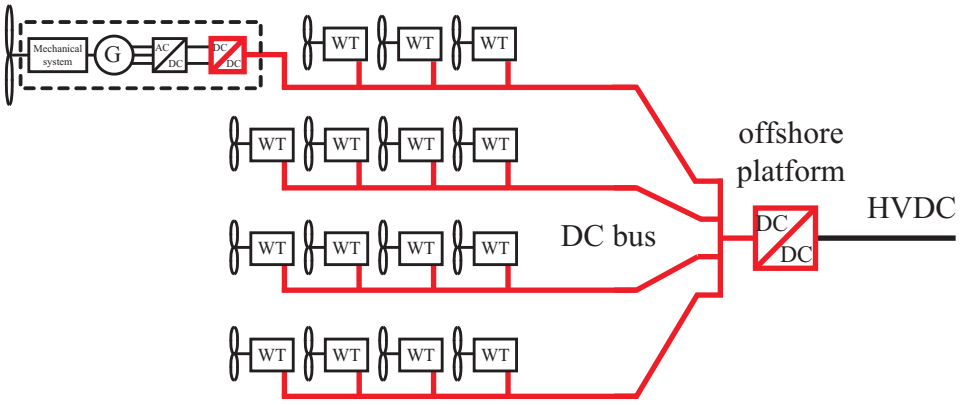

Fig. 4.7 Components used in the calculations of the losses.

4.4.1 Losses for the Cables

For the losses in the cables, the cable resistances are used for the chosen core areas. Here, it is assumed that the distances between the turbines are 500 m. In reality, the distances will vary depending on the layout of each radial. The resulting losses can be seen in Fig. 4.8.

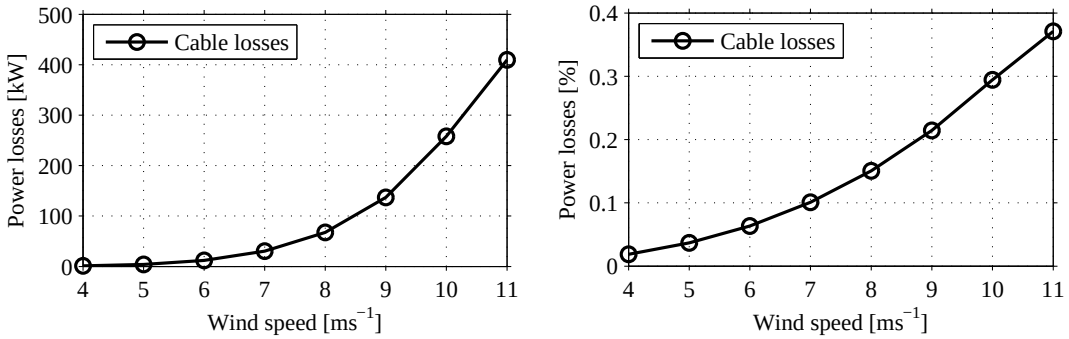

(a) Cable losses. (b) Cable losses as fraction of the input power.

Fig. 4.8 Losses for the DC bus cables.

In the figures, it can be seen that the cable losses are increasing from less then 0.02 % of the input power at low power levels to above 0.3 % at high power levels. The average losses at average wind speed 7.2 m/s are 0.24 %.

4.4.2 Losses for the DC/DC Converters

For the DC/DC converter in the wind turbine, the losses can be seen in Fig. 4.9.

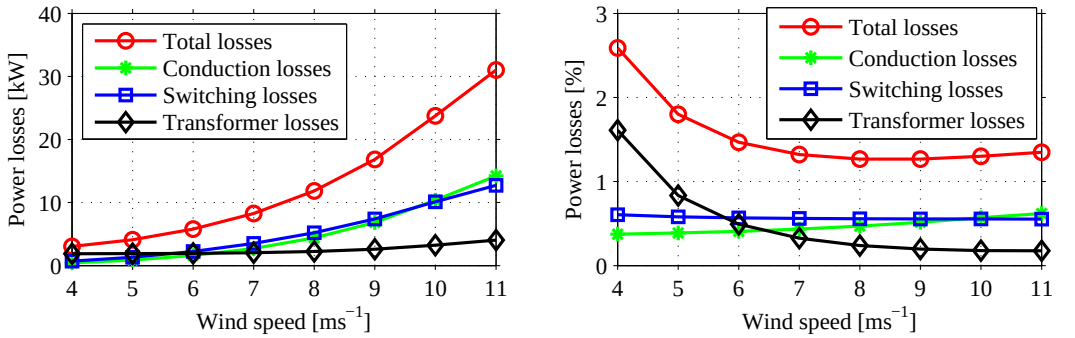

(a) Converter losses. (b) Converter losses as fraction of the input power.

Fig. 4.9 Losses for the DC/DC converter in the wind turbine.

The losses for high power levels are 1.3 % of the input power and for low power levels 2.6 %. Looking at the distribution of the losses, it can be seen that the switching losses are proportional to the input power. The fraction of conduction losses is almost constant, but increase slightly due to the increased on-state resistance at high current. The transformer losses is a larger fraction of the total losses at low power levels. This is due to the core

losses that just depend on the voltage applied at the transformer and therefore the absolute value of the core losses is constant for all power levels. However, the total losses in the transformer increase at high power levels due to the copper losses that increase with increasing current. Additionally, assuming an average wind speed of 7.2 m/s, the average losses for the DC/DC converter in the wind turbine are 1.35 % if the input power.

The losses are also calculated for the main DC/DC converter, where the results are shown in Fig. 4.10

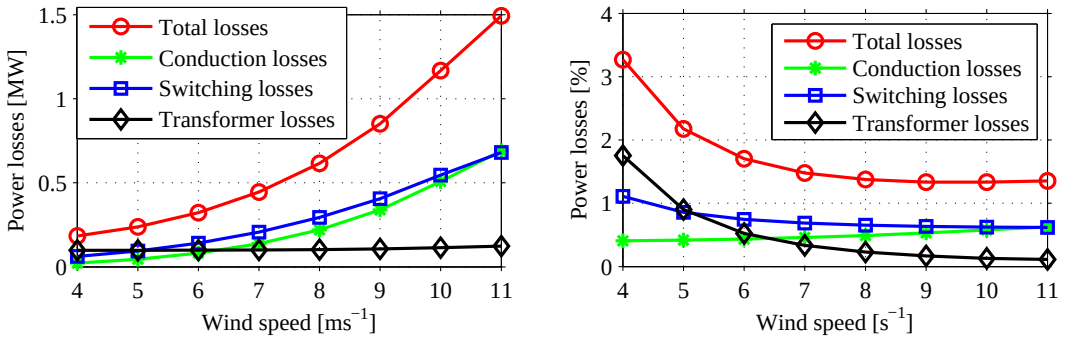

(a) Converter losses.

(b) Converter losses as fraction of the input power.

Fig. 4.10 Losses for the main DC/DC converter.

Also for the main converter it can be seen that the fraction of the losses is smaller for high power levels, 1.35 % of the input power, and higher for low wind speeds with 3.27 % of the input power. The average losses for the average wind speed of 7.2 m/s are 1.41 %. Similarly to the DC/DC converter in the wind turbine, the fraction of transformer losses decrease with increasing power while the fraction of conduction losses increase. Here, also the fraction of switching losses decrease slightly with increasing power.

4.4.3 Total Losses for the DC System

Adding all losses for the two DC/DC converters and the DC bus cables, the resulting losses can be found in Fig. 4.11.

For the total losses, it can be seen that the DC/DC converters have the largest contributions to the total losses. The total average losses are 3.0 % of the transferred power, where the wind turbine converter have 1.35 % losses of the transferred power, the main converter 1.41 % and the DC bus cables 0.24 %.

The total losses for the internal DC grid can be compared to the total losses of an internal

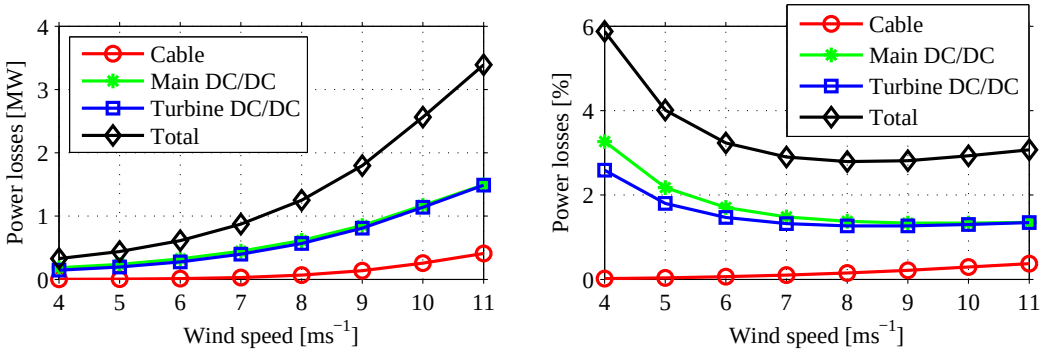

(a) Total cable and converter losses.

(b) Total cable and converter losses as fraction of the input power.

Fig. 4.11 Total losses for the cables and the two DC/DC converters.

AC grid connected to an HVDC transmission. The losses for the AC grid will depend on the chosen electrical system for the wind turbine. Assuming that there is a full power converter wind turbine, the difference between the turbines would be the inverter in the AC case and the DC/DC converter in the DC case as seen in Figs. 4.3 and 4.4. Here, the losses for the transformers can be assumed to be the same, and also the losses for the inverter towards the internal grid in Fig. 4.3 can be assumed to have similar losses as the fullbridge connected to the transformer in Fig. 4.4. The main difference in the losses would then be the additional losses for the rectifying diode bridge for the DC turbine. The losses for the diode bridge are 0.2 %, which can be compared to the total losses for the wind turbine DC/DC converter that are 1.35 %. Further, the losses for the main DC/DC converter of 1.41 % can be compared to the losses of the most recently installed VSC (Voltage Source Converter) HVDC transmissions, where each converter station has 1.6 % losses [51]. This figure is expected to decrease due to the development of VSC HVDC, so the losses of the main converter can be assumed to be the same as the losses for an HVDC converter station. The cable losses will be higher for the internal AC grid, but due to the relatively small cable losses for the short distances in the wind farm, this increase in losses is expected to be small. The additional losses from the DC/DC converters are then 0.2 % of the transferred power, and consequently the losses for the AC system are 2.8 % of the transferred power compared to 3.0 % for the DC system. However, it should be noticed that the losses vary significantly for different AC systems; if a DFIG turbine is used instead of a turbine with full power converter, the losses for the wind turbine converter can be reduced.

4.5 Summary

In this chapter, the design has been determined of the wind farm, which will be evaluated in Chapters 6 and 7. The layout is the same as for the wind farm Lillgrund, but the AC collection grid is replaced with a DC grid. The wind farm consists of 48 wind turbines of 2.3 MW each connected in five radials. In each wind turbine, there is a DC/DC converter that increases the 1.5 kV for the DC link in the wind turbine to 32 kV for the DC collection bus. Then, there is a main DC/DC converter for the wind farm that connects the 32 kV DC bus to the 130 kV HVDC transmission. Further, the designs of the cables and the DC/DC converters have been determined as well as the losses in the DC grid. It was found that the total average losses are 3.0 % of the transferred power, distributed with 1.35 % losses for the wind turbine converter, 1.41 % for the main converter and 0.24 % for the DC bus cables.

Chapter 5

Dynamic Modeling of the Wind Farm

5.1 Introduction

In Chapter 4, the design of the wind farm was determined and the losses for the system were calculated. In addition to the steady state losses for the wind farm, also the dynamic properties are important. The dynamic operation of the wind farm should be investigated both for normal operation and for different faults conditions. To carry out these investigations, a dynamic model of the wind farm must be developed. In this chapter, the dynamic models of all components are presented as well as an overview of the system model.

When modeling a large DC power electronic system, a large number of subsystems can be used [52]. These systems consist of for example a DC/DC converter in each subsystem. The simulation model described in this chapter will also be based on submodules with a wind turbine in each subsystem. When investigating the dynamic behavior of the system, the simulation model that is used depends on the conditions that should be studied. Looking at the startup of the system, the dynamics of the wind turbine are important and must then be modeled. However, if transient conditions for the DC bus should be studied, these are must faster than the dynamics for the wind turbine, which then can be neglected. Three different models will be used for the simulations of the wind turbine; one model in Matlab/Simulink and two models in PSCAD/EMTDC, one simplified model and one switching model. For the simulations of the whole wind farm, models in PSCAD/EMTDC will be used.

5.2 Model of the System

In the wind farm, the wind turbines are connected in five radials to a common DC bus that is connected to the main DC/DC converter as shown in Fig. 4.1. The simulation model consists of an overview model where the turbines and the main DC/DC converter are

modeled in submodules. Starting with the submodule of a wind turbine, an overview of the model is given in Fig. 5.1.

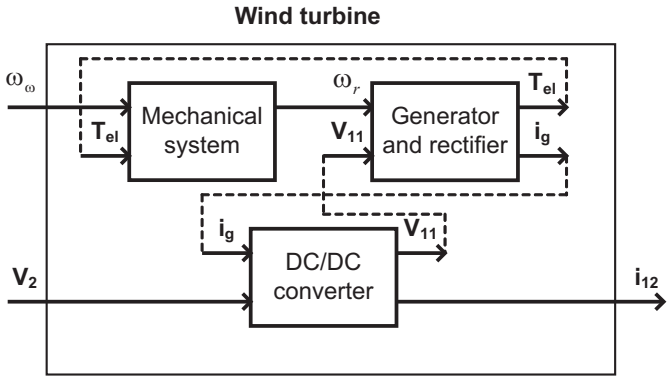

Fig. 5.1 Overview of the wind turbine model.

In the model, the inputs and outputs for each submodule are shown, i.e. which parameters that are determined in the submodule and which parameters that are inputs. For the wind turbine, the inputs to the system are the wind speed w_w and also the voltage V_2 at the connection point to the DC bus, which is determined by the main DC/DC converter. The output from the model is the current i_{12} delivered from the turbine to the DC bus. For the mechanical system, the turbine rotor is modeled. The wind speed is acting on the rotor disk and together with the rotational speed and the pitch angle, a mechanical torque is given. Using the electrical torque from the generator, the resulting speed is obtained for the generator. The output from the mechanical block is the rotational speed w_r that is also the input to the model of the generator and the rectifier. The model of the generator and rectifier determines the electrical torque T_{el} acting on the rotor and also gives the output current i_g from the rectifier to the DC/DC converter in the wind turbine. The second input to the generator is the DC link voltage V_{11} in the wind turbine. Finally, the output current from the rectifier is the input to the model of the DC/DC converter. The DC/DC converter controls the DC link voltage and the output of this model is thereby the DC link voltage V_{11} as well as the output current i_{12} to the DC bus.

Using the submodule with the model for the wind turbine, a model of the wind farm can be made as shown in Fig. 5.2, representing the wind farm shown in Fig. 5.3.

When studying the model, it should be noted that the voltages are determined from the main DC/DC converter, and the voltage at the turbines are the DC link voltage for the main converter plus the voltage drop along the cable. Starting from left in the figure, the last wind turbine in the radial has the input voltage $V_{2,10}$ from the cable between turbines 9 and 10 and gives the output current $i_{12,10}$ to the cable. For all wind turbines, the wind

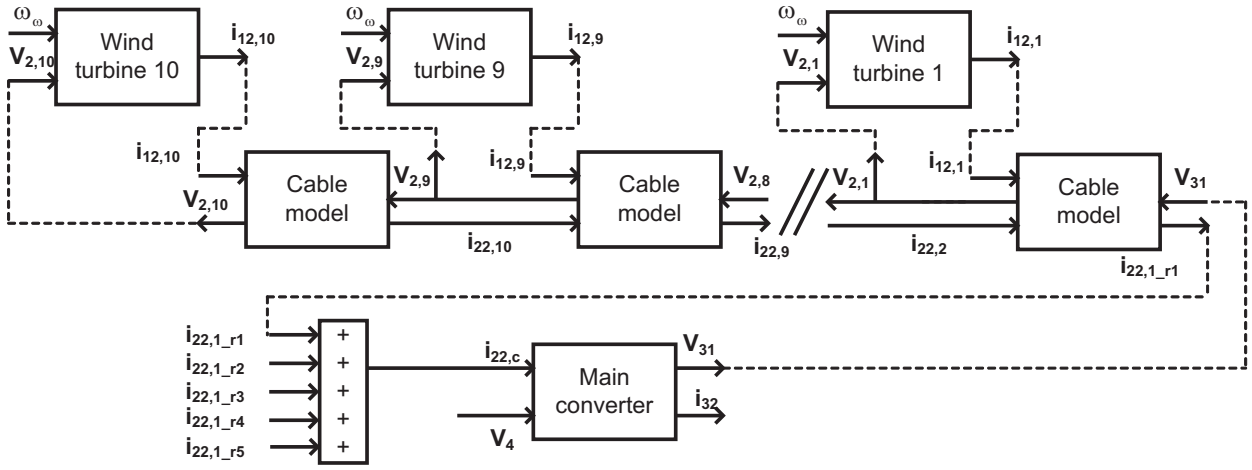

Fig. 5.2 Overview of the model of the wind farm.

speed w_w is an input parameter. In the same way for turbine 9, the input voltage $V_{2,9}$ is obtained from the cable model between turbine 9 and turbine 8, and this voltage is also the input voltage for the cable between turbines 9 and 10. The output from turbine 9 is the current $i_{12,9}$ that together with the current $i_{22,10}$ is fed into the cable model. All turbines in the radial are connected in the same way, with a cable model between each turbine. The current in the cable is the current from the turbine plus the current from the cable connecting the turbines further out in the radial. Looking at the cable model between turbine 1 and the main converter, the total current is the current $i_{12,1}$ from the turbine added with the current $i_{22,2}$ from the cable connected to turbine 2, which is the total current from turbines 2-10. The other side of this cable model is connected to the main converter together with the other four radials as shown in Fig. 5.3, where the output current $i_{22,1_{r}1}$ is added to the output current from the other radials and then gives the input current $i_{22,c}$ to the main converter as shown in Fig. 5.2. Further, the input voltage to the cable between turbine 1 and the main converter is the DC link voltage for the main converter V_{31}. For the main converter, the input voltage V_4 is the DC voltage at the HVDC connection and the input current $i_{22,c}$ is the total current from all turbines in the wind farm. The outputs are the HVDC current i_{32} and the DC bus voltage V_{31} at the input of the main DC/DC converter.

It should be noted that using the detailed model for the turbines for all 48 turbines is not needed and would also give a very slow simulation model. Therefore, the model is simplified as much as possible for all simulations. For example, the model of the turbine can be simplified with a current source connected to the DC/DC converter in the wind turbine for most turbines. Further, looking at one radial, the turbines including the DC/DC converters in the other radials can be modeled with current sources.

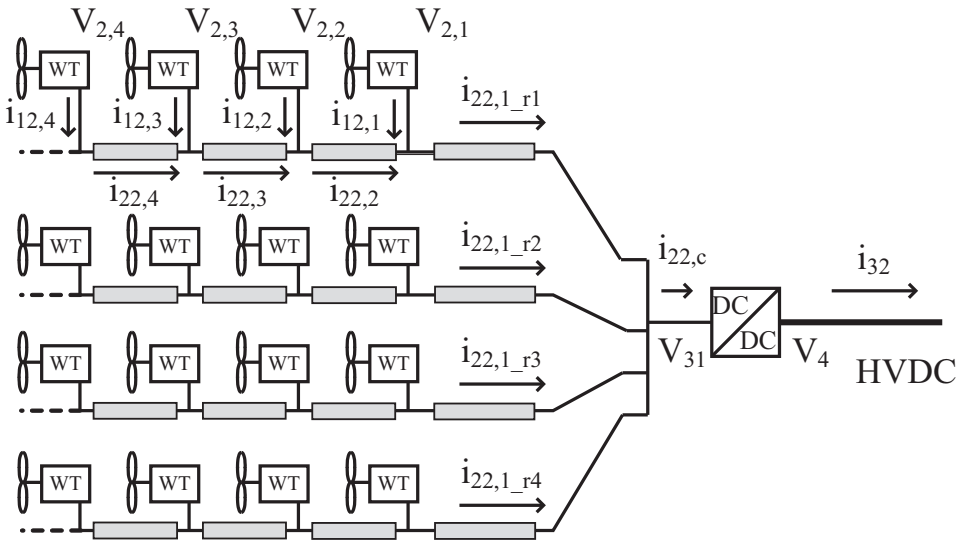

Fig. 5.3 Layout of the wind farm, with reduced number of turbines.

5.3 Model of the Wind Turbine Generator and Rectifier

For the simulations of the internal grid in the wind farm, adequate models for the wind turbines are required to achieve realistic operating conditions in the internal grid. In this section, the wind turbine models used for the three different simulation models are presented. There are two different parts of the model, the electrical part and the mechanical part. When modeling the mechanical part of the turbine, the model is made as simple as possible still keeping the same characteristics seen from the DC/DC converter in the wind turbine. Consequently, factors that are compensated for by the inverter controlling the generator are not seen by the DC/DC converter and can therefore be neglected in a study focusing on the DC/DC converters. This applies mainly to the models of the wind and the mechanical system.

Starting with the mechanical part, a large part of the model is given by equations and is therefore the same for all simulation models. However, the dynamics and the inertia for the turbine rotor and generator is modeled slightly differently. Continuing with the electrical model, the differences are larger between the models. In the Simulink model, a simplified model of a DC generator is used while the built-in model for an induction generator is used in PSCAD. For the rectifier, ideal models are used in Simulink and the simplified model in PSCAD while a more detailed model of the rectifier will be used for the switching model in PSCAD.

5.3.1 Mechanical System

Starting with the mechanical part of the wind turbine generator, the overview of the model is seen in Fig. 5.4. A similar mechanical system for modeling a wind turbine is shown in [31].

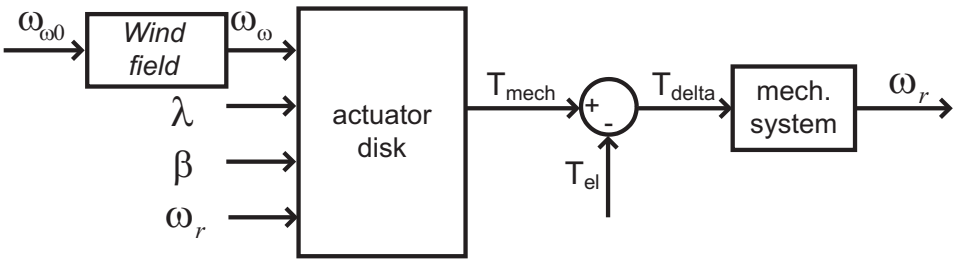

Fig. 5.4 Model overview for the mechanical part of the wind turbine.

In the figure, it can be seen that there are three main parts of the mechanical system; the input wind field, the model of the actuator disk and the mechanical system.

Model of the Wind

The main input to the system is the wind speed, which determines the power that can be obtained from the system. When the wind speed $\omega_{\omega 0}$ is measured, it is done in one certain point and differs from the average wind speed at the large area of the rotor. To obtain a more realistic value of the average wind speed ω_ω at the rotor, a spatial filter is used [31, 53]. The simplified transfer function for the spatial filter is

$$H_{SF}(s) = \frac{1}{sb+1}, \tag{5.1}$$

where $b = \gamma r_r / \bar{\omega}_\omega$ and γ is the damping factor, r_r is the radius of the rotor and $\bar{\omega}_\omega$ is the average wind speed at hub height. To obtain a more realistic model of the wind field at the rotor disk, also a rotational sampling filter can be used [53]. However, it is assumed that the effects of this filter can be removed by the inverter, and it is therefore neglected in this model.

Model of the Actuator Disk

The main part of the mechanical system is the actuator disk that converts the power in the wind to mechanical power on the shaft. The mechanical output power P_{mech} from the actuator disk is calculated as

$$P_{mech} = \frac{\rho_{air}}{2} A_r C_p(\lambda, \beta) \omega_\omega^3, \tag{5.2}$$

where ρ_{air} is the air density, A_r is the area swept by the rotor, ω_ω is the wind speed and $C_p(\lambda, \beta)$ is the power coefficient [18]. The power coefficient $C_p(\lambda, \beta)$ determines the amount of power extracted from the wind and is dependent of the pitch angle β and the tip speed ratio λ that is calculated using the rotor speed ω_r, the rotor plane radius r_r as well as the wind speed ω_ω as

$$\lambda = \frac{\omega_r r_r}{\omega_\omega}. \tag{5.3}$$

The values of C_p are dependent on the design of the blades and a table of values can be obtained from detailed calculations. Here, the value of C_p for steady state operation can be found from a lookup-table using the values shown in Fig. 5.5 [54].

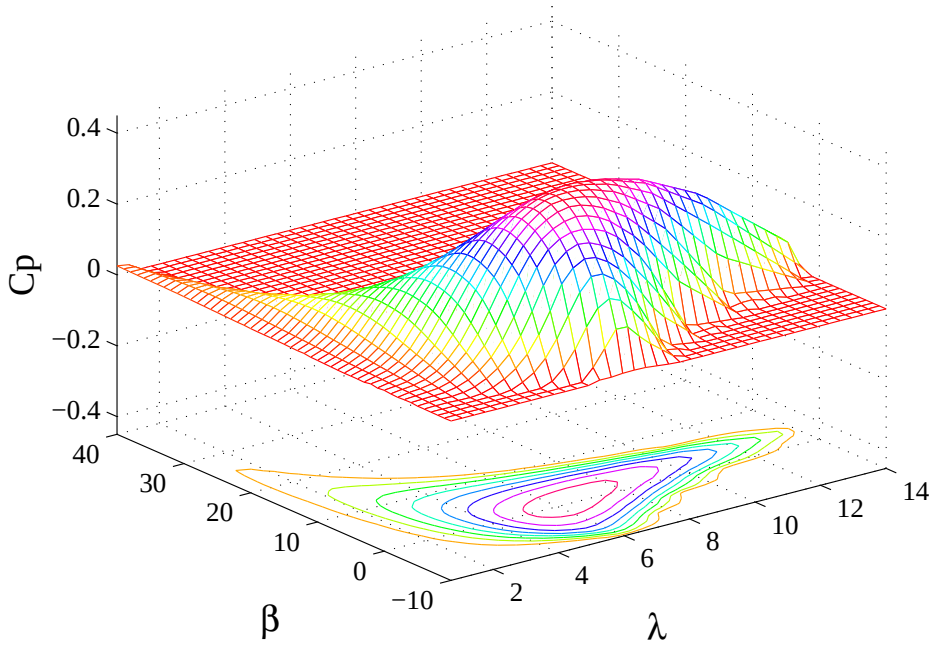

Fig. 5.5 Values of the constant C_p as a function of λ and β.

Knowing the values of λ that are obtained by (5.3) and β that is a result of the controller described in section 6.2, the value of C_p can be obtained and the mechanical power P_{mech} is calculated using (5.2). The mechanical power is then divided by the rotational speed of the rotor w_r (on the low-speed side of the gearbox) to obtain the mechanical torque T_{mech} on the shaft. The electrical torque T_{el} is subtracted from the mechanical torque resulting in the torque T_{delta} acting on the rotor.

Model of the Mechanical System

The mechanical system in a wind turbine is generally modeled as a two-mass model, considering the inertias of both the turbine and the generator, using a soft shaft model [53]. However, here it is assumed that the effects of a two mass model with a soft shaft can be compensated by the inverter controlling the generator. Therefore the average power from the turbine and the rotational speed of the turbine are not affected significantly by the choice of soft or stiff shaft. Therefore, a stiff shaft is use to simplify the model of the turbine.

5.3.2 Electrical System

The models of the electrical system differ between the simulation models, and therefore these models are treated separately. The model made in Simulink is a simplified model and is here just used for steady-state simulations. The model in PSCAD/EMTDC is a more detailed model and can therefore be used to study the startup of the system including the magnetization of the generator.

Generator Model in Simulink

In the simulation model in Simulink, the generator and rectifier are represented by a DC generator and the inverter is modeled as a variable transformer as seen in Fig. 5.6.

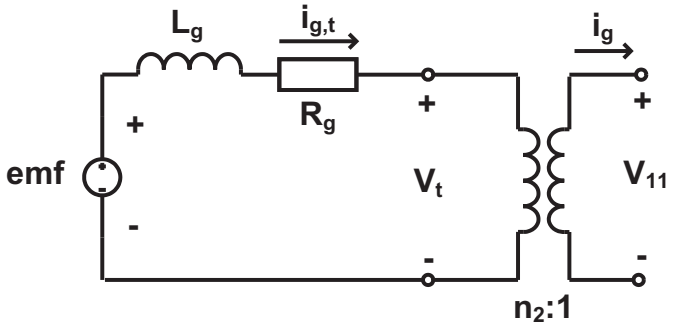

Fig. 5.6 Equivalent circuit for the model of the generator in Simulink.

The simplified model used for the generator, including the back emf and well as the inductance L_g and the resistance R_g in the generator windings gives the transfer function for the electrical system $F_e(s)$ as

$$F_e(s) = \frac{1}{L_g s + R_g}. \tag{5.4}$$

The implementation in Simulink of the model is shown in Fig. 5.7.

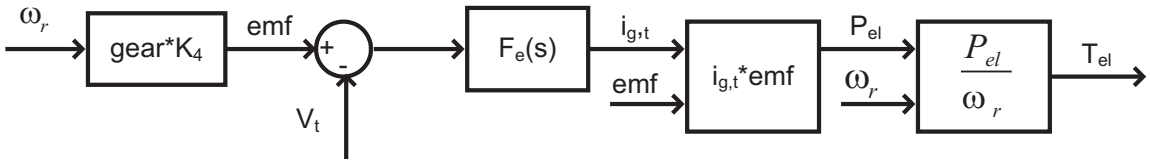

Fig. 5.7 Model overview for the electrical part of the wind turbine in Simulink.

The induced voltage emf in the circuit is determined by the rotational speed of the wind turbine. To obtain the value emf of the back emf, the rotational speed w_r of the turbine must be multiplied by the ratio $gear$ of the gearbox that gives the rotational speed w_g of the generator, as well as the constant K_4 that gives the value of emf. The current in the generator, and thereby also the electrical power P_{el} and the electrical torque T_{el}, are controlled by the voltage V_t applied at the generator. This voltage is the input voltage from the IGBT based rectifier. The current in the generator is given by

$$emf - V_t = L_s \frac{di_{g,t}}{dt} + R_s i_{g,t}. \tag{5.5}$$

The resulting current $i_{g,t}$ in the generator is multiplied with the induced voltage emf to obtain the electrical power P_{el}. The electrical power is divided by the rotational speed of the rotor w_r to get the electrical torque T_{el} on the low-speed side of the gearbox. As shown in Fig. 5.4, the electrical torque will determine the torque applied at the rotor and thereby control the operating point of the wind turbine as shown in section 6.2. The control of the generator will be achieved by varying the voltage V_t applied at the generator. This is done by varying the ratio n_2 that represents a variation in the duty cycle for the rectifier that controls the generator.

Generator Model in PSCAD/EMTDC

When using PSCAD/EMTDC, there is a built-in model for the induction machine that is used in the simulations. In Fig. 5.8, the simple model in PSCAD is shown where the generator is controlled by three ideal voltage sources, one for each phase.

The main difference for the switching model is the model of the rectifier, as seen in Fig 5.9. Here, the generator is modeled in detail using models of the semiconductor components.

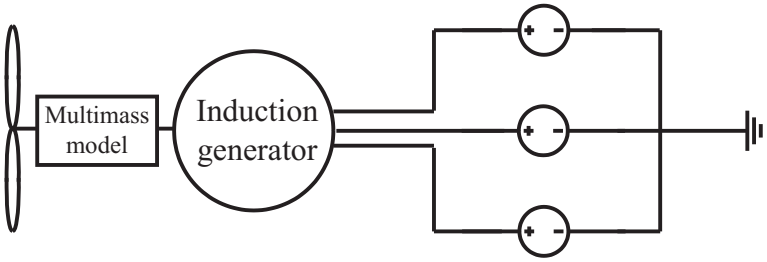

Fig. 5.8 Simple generator model in PSCAD/EMTDC.

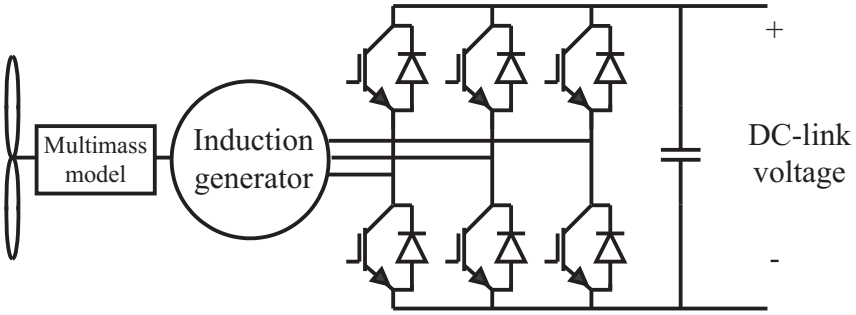

Fig. 5.9 Switching generator model in PSCAD/EMTDC.

5.4 Model of the DC-DC Converters

When modeling the DC/DC converters, the models varies significantly depending on the requirements of the simulation and the used simulation software. When using Simulink, a state space average model is used assuming the fullbridge converter to be an ideal transformer connected to the input and output filters. This model considers the average characteristics of the system and can not be used for detailed investigations of the behavior of the DC/DC converters. Using PSCAD, the DC/DC converter can be modeled in detail using IGBT switches, and thereby also be used for detailed investigations of the DC/DC converters. The disadvantage with the detailed model is that the simulation requires a short time step and will thereby be slow. The simplified model in PSCAD is more similar to the model used in Simulink, and is not considering the switching behavior of the DC/DC converters. It should be noted that even though the output filter is current stiff, there is a capacitor connected to the output to limit the current ripple. This capacitor is not included in the model of the DC/DC converter, instead it is added to the capacitance for the cable connected to the output of the DC/DC converter.

5.4.1 State-Space Model Used in Simulink

Using a program like Matlab, the DC/DC converters can although the non-linear behavior be expressed as a state-space function using state-space averaging [29]. However, the linear state-space averaging will eliminate the ripple caused by the switching operation of

the transistors.

Here, the state-space equations will be shown starting with the main DC/DC converter. The circuit representation of the DC/DC converter used for obtaining the state-space equations is seen in Fig. 5.10. The input to the converter is the voltage V_4 for the HVDC link that is determined by the outer system. The input current $i_{22,c}$ is the sum of the generated currents from the wind turbines in all radials and will thereby also act as an input signal. The states are the voltage across the capacitor V_{31c} and the output current i_{32} that is also the current in the output inductance. As output signals, the voltage V_{31} is applied at the DC bus connecting the wind turbines, the output current i_{32} is forwarded to the model of the HVDC connection and the voltage V_{31c} across the capacitor is only used for monitoring. The variable that controls the circuit is the variable transformer ratio n_3. The variable n_3 is not an input signal but a variable parameter in the state-space equations.

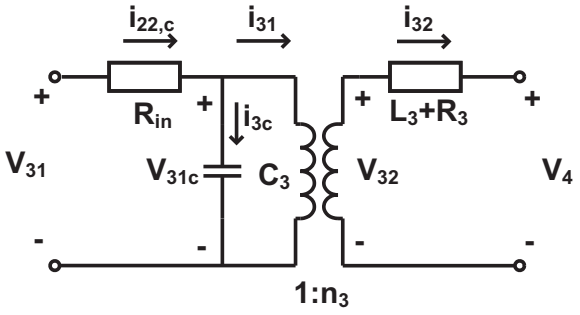

Fig. 5.10 Equivalent circuit for the main converter used for the state space equations.

To obtain the state-space model, the equations for the circuit must be known. Starting with the expression for the voltage V_4, the derivative for the current i_{32} can be calculated as

$$V_4 = V_{31c}n_3 - L_3\frac{di_{32}}{dt} - R_3 i_{32} \Rightarrow \frac{di_{32}}{dt} = V_{31c}\frac{n_3}{L_3} - i_{32}\frac{R_3}{L_3} - \frac{V_4}{L_3}. \tag{5.6}$$

Continuing with the expression for the current i_{3c} in the capacitor gives the expression for the derivative of the voltage V_{31c} across the capacitance C_3 as

$$i_{31c} = C_3\frac{dV_{31c}}{dt} = i_{22,c} - i_{31} = i_{22,c} - i_{32}n_3. \tag{5.7}$$

For the outputs from the state-space model, both i_{32} and V_{31c} are states and V_{31} is given by

$$V_{31} = V_{31c} - i_{22,c}R_{in}. \tag{5.8}$$

Using equations (5.6)-(5.8), the state space equations are shown below.

- Input signals: V_4, $I_{22,c}$
- States: V_{31c}, I_{32}
- Output signals: V_{31}, I_{32}, V_{31c}
- Control variable: n_3

State-space variables X, Input signals U and output signals Y:

$$X = \begin{bmatrix} V_{13c} \\ I_{32} \end{bmatrix}, U = \begin{bmatrix} I_{22,c} \\ V_4 \end{bmatrix}, Y = \begin{bmatrix} V_{31} \\ I_{32} \\ V_{31c} \end{bmatrix} \tag{5.9}$$

State-space equations:

$$\dot{X} = AX + BU \tag{5.10}$$

$$\dot{X} = \begin{bmatrix} 0 & -\mathbf{n_3}/C_3 \\ \mathbf{n_3}/L_3 & -R_3/L_3 \end{bmatrix} \begin{bmatrix} V_{31c} \\ I_{32} \end{bmatrix} + \begin{bmatrix} 1/C_3 & 0 \\ 0 & -1/L_3 \end{bmatrix} \begin{bmatrix} I_{22,c} \\ V_4 \end{bmatrix} \tag{5.11}$$

Output signal:

$$Y = CX + DU \tag{5.12}$$

$$Y = \begin{bmatrix} 1 & 0 \\ 0 & 1 \\ 1 & 0 \end{bmatrix} \begin{bmatrix} V_{31c} \\ I_{32} \end{bmatrix} + \begin{bmatrix} R_{in} & 0 \\ 0 & 0 \\ 0 & 0 \end{bmatrix} \begin{bmatrix} I_{31} \\ V_4 \end{bmatrix} \tag{5.13}$$

If instead the wind turbine converter is used with the rectifier towards the generator, the circuit is seen in Fig. 5.11.

The same state-space equations are used as for the main DC/DC converter, but the ratio n_2 of the inverter has to be taken into account. This affects the values of i_g and V_{11} as

$$\begin{aligned} i_g &= \tfrac{i_{g,t}}{n_2} \\ V_t &= \tfrac{V_{11}}{n_2} \end{aligned} \tag{5.14}$$

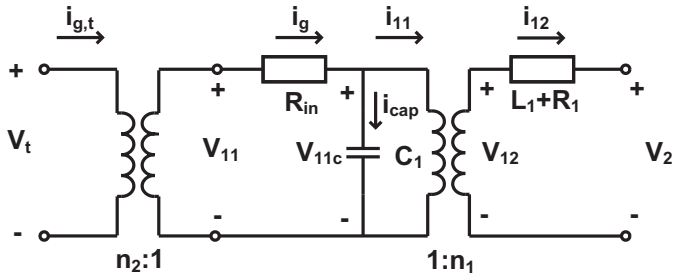

Fig. 5.11 Equivalent circuit for a wind turbine converter used for the state space equations.

5.4.2 Circuit Models Used in PSCAD/EMTDC

When using PSCAD/EMTDC, the circuits are constructed in a circuit simulation software and no state space equations needs to be made. In Fig. 5.12 the circuit models are shown for (a) the switching model and (b) the simplified model.

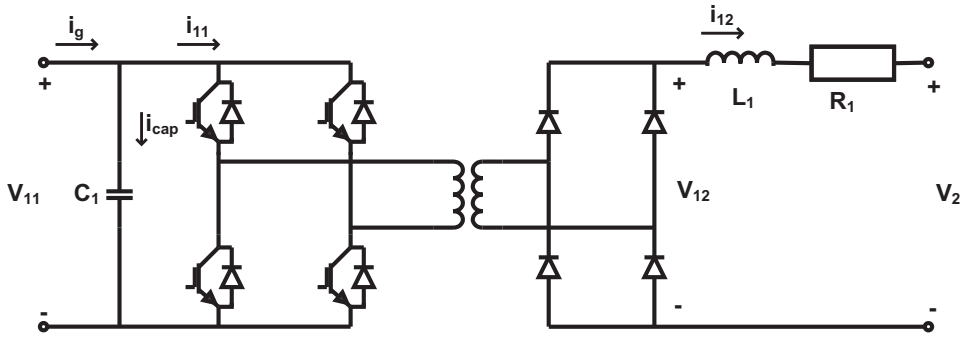

(a) Switching model.

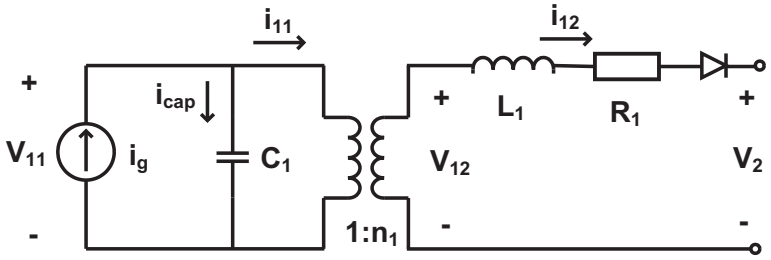

(b) Simplified model.

Fig. 5.12 Circuit models in PSCAD/EMTDC for the DC/DC converter for both the switching model and the simplified model.

As seen in the figure, the switching model is a model including all switches and diodes. The values of the filter components R_1, L_1 and C_1 are the same as for the model in Simulink. This model is connected to the model of the generator and rectifier shown in Fig. 5.9. For the simplified model, the filter components are the same as for the switching

model, but the fullbridge has been removed and replaced with an ideal transformer. As seen in Fig. 5.8, there is no electrical connection to the generator and rectifier. Instead, there is a current source in the model of the DC/DC converter representing the output current from the rectifier. The value of the current is calculated using the electrical power from the rectifier as well as the voltage V_{11} for the DC link. Here, it should be noted that in the Simulink model there was a resistance between the input to the converter and the DC link. Therefore, the voltage V_{11c} at the DC link is not the same as the input voltage V_{11} to the converter. However, in the model in PSCAD, this resistance is neglected and the DC-link voltage V_{11c} is equal to the input voltage V_{11}. Assuming the voltages V_a, V_b and V_c as well as the currents i_a, i_b and i_c in the phases for the rectifier, the current i_g can be calculated as

$$i_g = \frac{P_{el}}{V_{11}} = \frac{i_a V_a + i_b V_b + i_c V_c}{V_{11}} \tag{5.15}$$

5.5 Model of the DC-Cables

5.5.1 Model of the Internal DC Bus

For the DC bus, a cable segment can be modeled with the π-link model as shown in Fig. 5.13 [17].

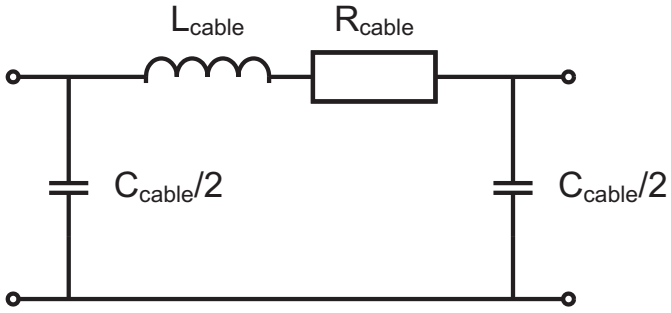

Fig. 5.13 π-link model for the DC bus cable.

When simulating the system, the cable parameters used are shown in Table 4.2. Each cable segment is located between two capacitors, which are the output filter capacitors for the wind turbine DC/DC converters. The filter capacitance is added to the cable capacitance in the π-link model. Since the cable segments are short, the dynamics are very fast and a more detailed cable model consisting of 10 π-links will just affect the results in the case of very fast transients. For a simulation model with a time step longer than a few μs, the model with one π-link and the model with 10 π-links will not give different results.

5.5.2 Model of the HVDC-Connection

The model of the HVDC connection is shown in Fig. 5.14.

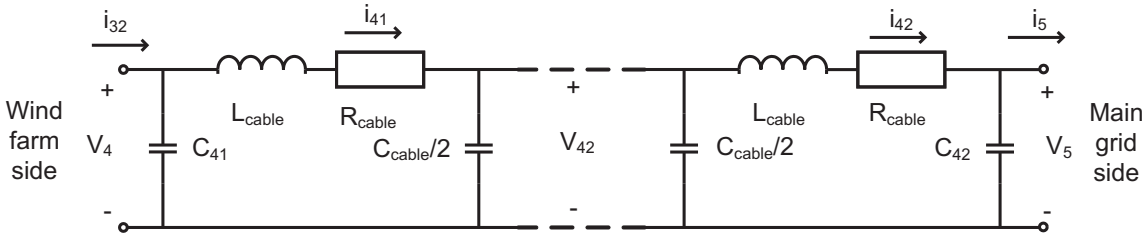

Fig. 5.14 Model for the HVDC cable.

Since the HVDC cable is assumed to the be 40 km, it is modeled by 8 series connected π-models as shown in Fig. 5.14 of 5 km each. Also the parameters for the HVDC cable are shown in Table 4.2.

5.6 Summary

In this chapter, a dynamic model is obtained for the wind farm designed in Chapter 4. A model of the wind turbine and the DC/DC converter is made both in Simulink and PSCAD/EMTDC, while the whole system model is made in PSCAD/EMTDC. This model will be used to evaluate the control during normal operation as well as the handling of fault conditions.

Chapter 6

Control of the Wind Farm with a DC Collection Grid

6.1 Introduction

For the investigated wind farm with a DC collection grid, the design of the wind farm was determined in Chapter 4 and the dynamic model was presented in Chapter 5. In this chapter, the control of the wind farm is developed and evaluated using the obtained simulation models. For the control of the wind farm, the wind turbines should be controlled as well as the DC system. For normal operation, the control of the wind turbines aims at extracting as much power as possible within certain limits. The control of the DC/DC converters aims at keeping the voltages at the DC links at the rated values by controlling the power flow in the system. The control method for the DC/DC converters is verified using a down scaled experimental setup. Also, the startup of the wind farm is investigated.

6.2 Control of the Wind Turbines

6.2.1 Control of the Mechanical System

When controlling the wind turbine, the aim is to extract as much electrical power as possible up to a certain maximum power and then keep the generated power constant at higher wind speeds. Further, in the case of a variable speed wind turbine, the rotational speed should be limited below a maximum value. The control of the wind turbine can therefore be divided into three different operation modes with different control schemes [54]. In [55], two different operating regions are considered with similar control strategies.

- At **low wind speed** ($\sim$4-11 m/s), the control aims at extracting as much power as possible from the wind and the rotational speed of the wind turbine can be adjusted to obtain as large value of C_p as possible and thereby also maximum mechanical

power. The rotational speed of the wind turbine is controlled by adjusting the electrical breaking torque from the generator.

- At **medium wind speed** ($\sim$11-13 m/s), the maximum rotational speed of the wind turbine is reached and is kept constant at that level. However, the controller will still find the value of pitch angle β that gives the maximum mechanical power from the wind and the rotational speed will be kept by controlling the electrical torque.
- At **high wind speed** (above $\sim$13 m/s), the rated power level has been reached and the extracted electrical power is kept constant at the maximum value. Since the rotational speed also should be kept constant at the maximum steady state value, the pitch angle β must be controlled in order to adjust the mechanical torque and keep the rotational speed constant.

In this study, the control scheme should be made as simple as possible to reduce the computational power needed for the simulations. Therefore, the control is simplified to the control of the rotational speed by the electrical torque (including the low and medium wind speeds regions) and the control of the generated power by the pitch angle (in the high wind speed region).

Control of the Electrical Torque

When controlling the wind turbine, the rotational speed of the wind turbine is an important factor. As shown in section 5.3, the extracted mechanical power from the wind is dependent on the power factor C_p. The value of C_p is a function of the ratio λ between the tip speed of the wind turbine and the wind speed. Consequently, the extracted mechanical power from the wind is dependent on the control of the rotational speed of the wind turbine. The rotational speed can be controlled by the torque applied at the turbine rotor (the mechanical torque minus the electrical torque) up to the rated electrical power where the electrical torque can not be increased further to limit the rotational speed. The control for the rotational speed of the turbine is shown in Fig. 6.1.

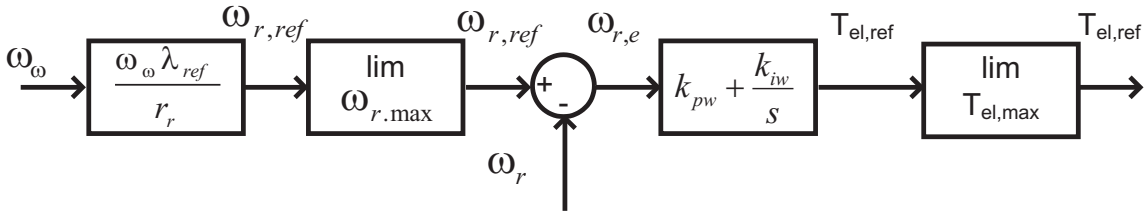

Fig. 6.1 Overview of the speed control of the turbine.

The control of the rotational speed applies when the maximum power is not reached. The

reference rotational speed $\omega_{r,ref}$ is the speed that gives the value of λ_{ref} resulting in the largest value of C_p. This value is calculated as

$$\omega_{r,ref} = \frac{\lambda_{ref}\omega_\omega}{r_r}. \tag{6.1}$$

However, there is a maximum speed for the turbine and therefore a limit is inserted that limits the reference speed to the maximum speed. Knowing the reference value of the speed, the torque applied at the turbine is controlled using a PI-controller. The actual speed ω_r is subtracted from the reference speed and the error signal $\omega_{r,e}$ is the input to the PI-controller. The output of the controller is the reference value for the torque $T_{el,ref}$ applied at the turbine from the generator. However, since the electrical output power is limited, there is a resulting limitation in the electrical torque depending on the speed of the turbine. The reference value of the electrical torque is then the input to the control of the generator.

To validate the control methods and also see the difference between the simulation models during normal operation, simulations are made with the same example wind speed. The used wind signal is shown in Fig. 6.2, showing both the measured wind signal $\omega_{\omega 0}$ and the average value ω_ω seen by the rotor disk as explained in the previous chapter.

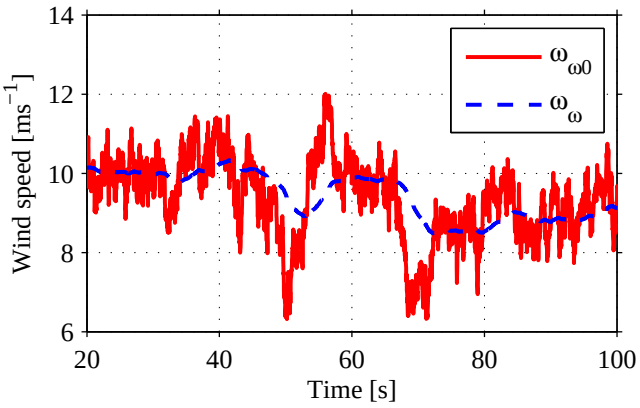

Fig. 6.2 Input wind speed for the simulations.

As stated above, the aim of the torque control is to control the speed of the turbine to follow the reference speed. In Fig. 6.3 (a), the resulting speed is shown for the three simulation models ($\omega_{r,s}$ for the Simulink model, $\omega_{r,e}$ for the simple PSCAD model and $\omega_{r,econv}$ for the switching PSCAD model), together with the reference speed $\omega_{r,ref}$. Also the resulting electrical output power is seen Fig. 6.3 (b)

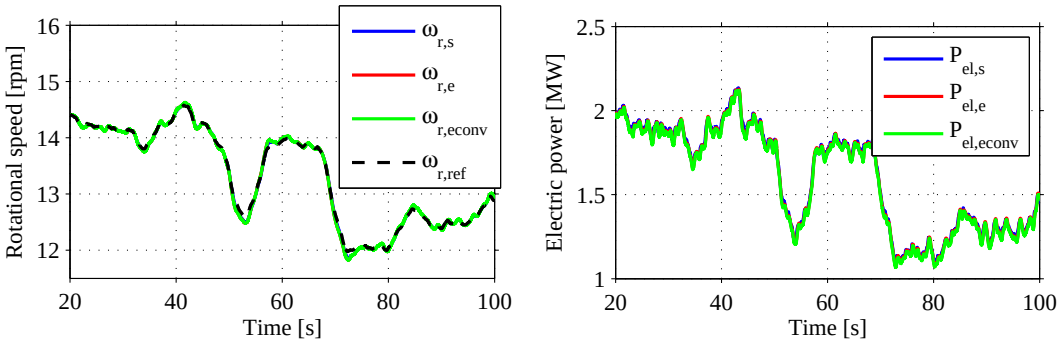

(a) Rotational speed. (b) Electrical output power.

Fig. 6.3 Resulting speed and electrical output power using the control of the electrical torque.

In the figure, it can be seen that both the resulting speed and the electrical output power are very similar for all simulation models and also that the reference value for the speed is followed closely.

Control of the Pitch Angle

The speed control described in the previous section keeps the wind turbine at the desired operating point as long as the electrical power needed to achieve the reference value of the electrical torque does not exceed the maximum electrical power. If the electrical power reaches the maximum value, it is limited and the control of the rotational speed is then achieved by changing the pitch angle to instead control the mechanical torque from the turbine. As seen in Fig. 6.4, there are two different ways to achieve the value of the pitch angle β depending on the wind speed.

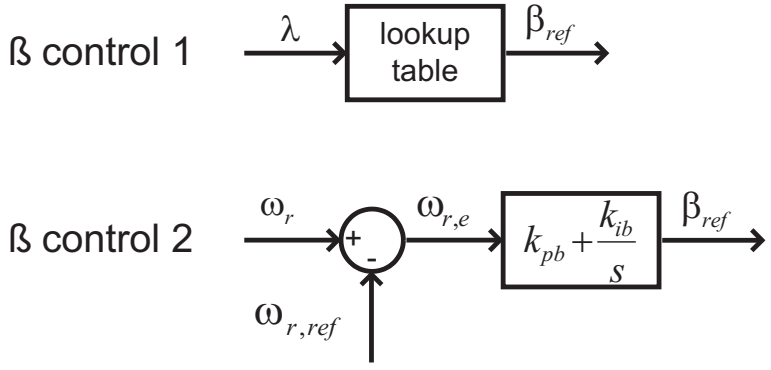

Fig. 6.4 Control methods for the pitch angle β.

The first strategy for the control of β is when the speed control mentioned above is used and the electrical power is below the maximum value. Then, the reference value β_{ref} is

the value that gives the highest C_p for the given tip speed ratio λ.

The second strategy is when the electrical power needed to limit the rotational speed exceeds the maximum value. The electrical torque will be limited and instead the pitch angle β of the rotor blades is used to limit the captured mechanical power. Since the power in this case is kept constant and can not be controlled, the control of β aims at keeping the speed constant. Therefore, the input to the controller is the actual rotor speed ω_r and the reference rotor speed $\omega_{r,ref}$. The error signal $\omega_{r,e}$ is the input to the PI-controller that gives the resulting reference value for β_{ref}. Also for the control of β, the results are compared for the different simulation models. The input wind speed, that is in the high speed wind region, is shown in Fig. 6.5 (a). The resulting rotational speed can be seen in Fig. 6.5 (b), showing that the variations in the rotational speed are small for all simulation models and also that the results from the models agree well.

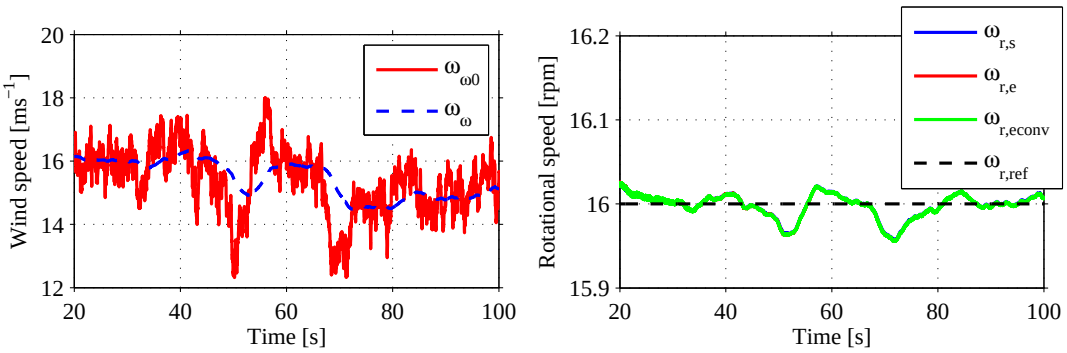

(a) Input wind speed.

(b) Rotational speed.

Fig. 6.5 Input wind speed for the control of the pitch angle β and the resulting speed.

6.2.2 Control of the Generator

As mentioned previously in this chapter, the output from the control of the wind turbine is the pitch angle β and the reference value of the electrical torque $T_{el,ref}$. The reference value of the electrical torque is then the input to the control of the generator. The control of the electrical torque is done in different ways for the Simulink model and the PSCAD models.

Control of the Generator in Simulink

For the generator in Simulink shown in Fig. 6.6, it can be seen that the electrical power from the shaft P_{el} can be obtained from multiplying the current $i_{g,t}$ and the induced voltage emf.

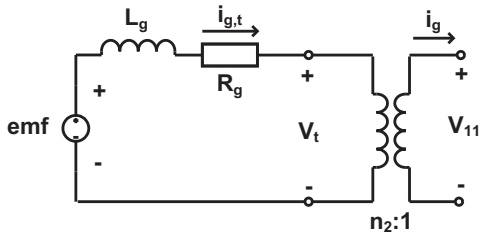

Fig. 6.6 Equivalent circuit for the generator.

Therefore, the reference value of the current $i_{gt,ref}$ can be calculated as

$$i_{gt,ref} = \frac{T_{el,ref}\omega_r}{emf}. \tag{6.2}$$

For the IGBT-based rectifier using the average ratio n_2, the aim is to achieve the generator current in order to control the operating point of the generator. The PWM AC/DC converter for wind turbines has been studied previous literature, in [56] a boost AC/DC conversion system was studied that could keep the DC-link voltage constant during variations in the wind speed (resulting in variations in the input voltage to the rectifier).

By applying a voltage ΔV across the inductance L_g and the resistance R_g in the windings, the generator current $i_{g,t}$ is controlled. An overview of the control scheme is shown in Fig. 6.7.

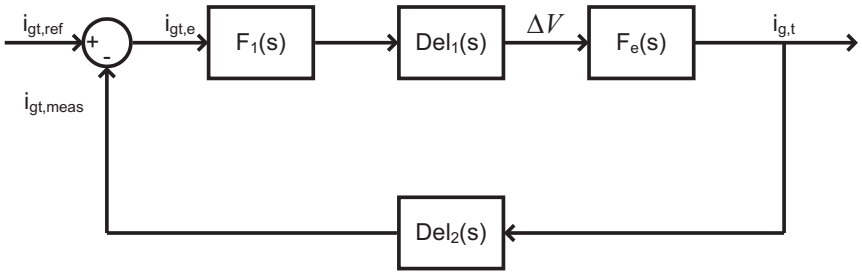

Fig. 6.7 Control of the electrical torque for the generator in Simulink.

The input value to the control is the reference value of the generator current $i_{gt,ref}$ that is obtained from the reference value of the torque which is the output value of the mechanical control of the wind turbine. The measured value of the actual generator current $i_{gt,meas}$ is then subtracted and the error value $i_{gt,e}$ is achieved. This is the input to the PI-controller $F_1(s)$ that has the transfer function

$$F_1(s) = k_{pe} + \frac{k_{ie}}{s}. \tag{6.3}$$

The resulting value of the voltage ΔV is applied across the inductance and resistance as shown in the electrical model described in section 5.3. The transfer function $F_e(s)$ is then used to get the value of the generator current $i_{g,t}$, and is expressed as

$$F_e(s) = \frac{1}{L_g s + R_g}. \tag{6.4}$$

Additionally, there are two time delays inserted into the system, $Del_1(s)$ and $Del_2(s)$ to represent the behavior of the converter. These delays are represented with Padé approximations in the transfer functions $Del_1(s)$ and $Del_2(s)$. When operating a real converter, it can be assumed that there are three major contributions to the time delays in the converter.

- **The computational time for the duty cycle of the converter.** From the measured value of the generator current and the reference value, the desired voltage ΔV should be calculated and also the voltage V_t applied to the generator. This takes some computational time and there is also a delay due to the sampling of the measured values. The time needed for the sampling of the measured values and the calculation of the reference values is assumed to be a half switching period T_s. This time delay is assumed to be a part of $Del_1(s)$.

- **The time for the averaging of the duty cycle.** When obtaining the model of the converter a state-space model is used that simplifies the switching behavior to an average value for the applied voltage for a duty cycle. However, when the duty cycle is changed, it takes half a switching period until the average value of the voltage is changed. Further, the modulation of the transistors should be calculated from the given value of n_2. Consequently, the time delay can be estimated as one switching period T_s. Also this time delay is a part of $Del_1(s)$.

- **The delay for measuring the actual current.** Since the control uses a feedback-loop the resulting current must be measured and used in the control. The measurement also introduces a time delay that is assumed to be a half switching period. This time delay is the delay $Del_2(s)$.

To analyze the system, the closed loop transfer function $G_{ry0}(s)$ is first obtained for the system neglecting the time delays as

$$G_{ry0}(s) = \frac{F_1(s)F_e(s)}{1 + F_1(s)F_e(s)} = \frac{1}{\frac{1}{F_1(s)F_e(s)} + 1}. \tag{6.5}$$

Assume that the closed loop transfer function should be a first order system with the bandwidth α_e and the time constant T_e, it can be expressed as

$$G_{ry0}(s) = \frac{1}{T_e s + 1}. \tag{6.6}$$

Combining functions (6.5) and (6.6) gives

$$T_e s = \frac{1}{F_1(s)F_e(s)} = \frac{L_g s^2 + R_g s}{k_{pe} s + k_{ie}} \Rightarrow k_{pe} s T_e + k_{ie} = L_g s + R_g. \tag{6.7}$$

Identifying the parameters results in the values for k_{pe} and k_{ie} as

$$k_{pe} = \frac{L_g}{T_e} = L_g \alpha_e \tag{6.8}$$

and

$$k_{ie} = \frac{R_g}{T_e} = R_g \alpha_e. \tag{6.9}$$

For the system without time delays, the control parameters are designed to have a rise time t_r of between 0.1 ms and 10 ms and the resulting step responses for the closed loop system $G_{ry0}(s)$ are shown in Fig. 6.8.

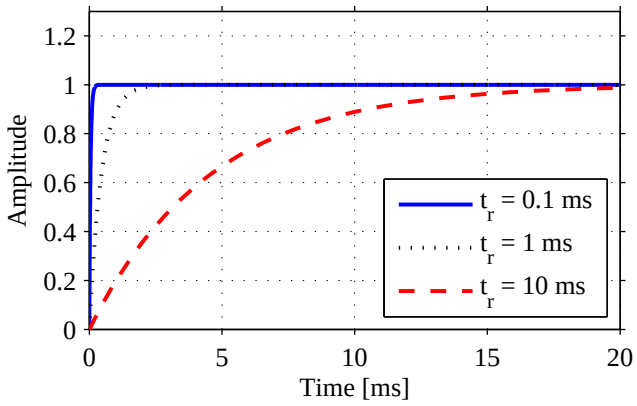

Fig. 6.8 Step response for the transfer function G_{ry0} for different rise times for the closed loop system without time delays.

In the figure, it can be seen that the system is stable even for very short rise times. However, in the real system, time delays are added and the characteristics of the system are

changed. The total time delays in the system $G_{ry}(s)$ are $\approx 2T_s$ = 1 ms (since the switching frequency for the inverter is set to 2 kHz). The rise time of the system should be considerably larger than this delay time in order to maintain a stable system. This can be seen in Fig 6.9 (a), where the step response is plotted for different rise times for the system.

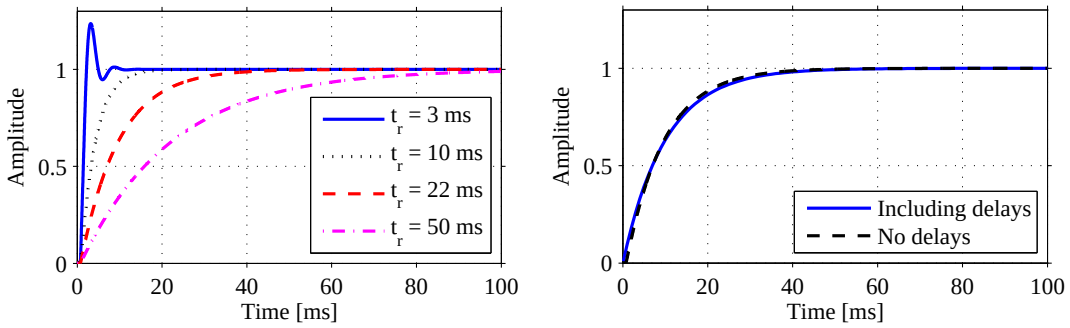

(a) Different rise times for the closed loop system. (b) Rise time 22 ms compared to the system without time delay.

Fig. 6.9 Step response for the transfer function G_{ry} with time delays.

It can be seen that for the rise time 3 ms, the system is stable but poorly damped. If the rise time is increased to 22 ms, the system is well damped and some additional time delay will not give an unstable system. Comparing the characteristics of the system with and without time delays for the chosen rise time gives the results shown in Fig. 6.9 (b).

As can be seen in the figure, there is no major difference between the systems with and without the time delays. Therefore, the time delays can be neglected to lower the complexity of the system in the case of the system time constant 22 ms.

Knowing that the rise time of 22 ms for the control of the inverter gives a stable system, is must also be investigated that the controller is fast enough to control the system. The aim of the current controller is to control the current and thereby also the electrical torque for the generator. In Fig. 6.10 the resulting torque is plotted together with the reference value of the torque for the wind signal that was shown in Fig. 6.2, showing that the electrical torque follows the reference value.

Control of the Generator in PSCAD

In PSCAD/EMTDC, the model of the generator is a three-phase induction generator. The input to the controller of the generator is the reference torque as well as the measured

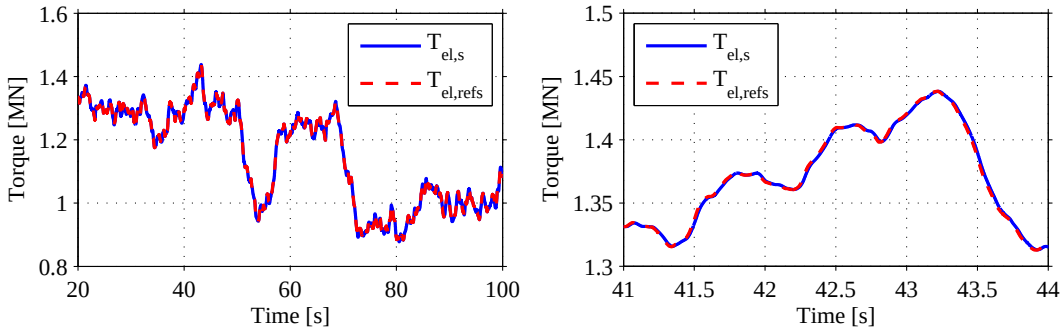

(a) Overview. (b) Zoomed figure.

Fig. 6.10 Resulting electrical torque for the Simulink model.

phase currents and the output is the voltage applied at the generator. To control the generator, vector control is used as described in detail in [57].

For the control of the generator, the induction generator is represented with the inverse Γ model, as shown in Fig. 6.11 (b). This model can be compared to the T model in Fig. 6.11 (a) that the parameters for a generator normally are given for.

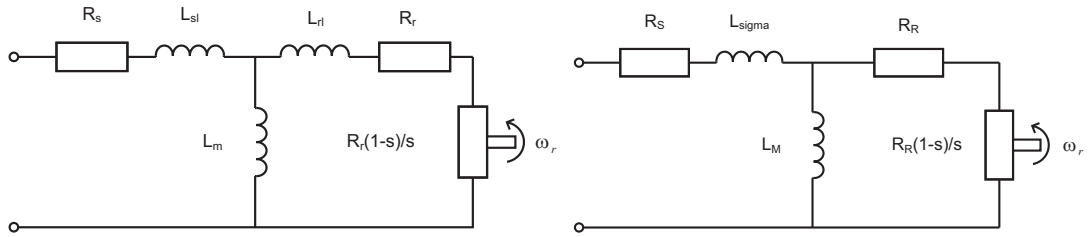

(a) T model. (b) Inverse-Γ model.

Fig. 6.11 Equivalent circuit for the induction generator using both the T model and the inverse-Γ model.

Consequently, since the parameters are given for the T model and the control is made for the inverse-Γ model, the parameters have to be transformed as shown in [57].

$$\begin{aligned} L_s &= L_{sl} + L_m \\ L_r &= L_{rl} + L_m \\ R_R &= \tfrac{L_m}{L_r}^2 \; L_M = \tfrac{L_m^2}{L_r} R_r \\ L_{sigma} &= L_s - L_M \end{aligned} \tag{6.10}$$

The first step in the control of the generator is to calculate the current in the rotating dq-frame. Starting from the measured phase currents i_a, i_b and i_c, the two-phase currents in

fixed coordinates, i_α and i_β are obtained as

$$\begin{bmatrix} i_\alpha \\ i_\beta \end{bmatrix} = K \begin{bmatrix} \frac{2}{3} & -\frac{1}{3} & -\frac{1}{3} \\ 0 & \frac{1}{\sqrt{3}} & -\frac{1}{\sqrt{3}} \end{bmatrix} \begin{bmatrix} v_a \\ v_b \\ v_c \end{bmatrix}, \tag{6.11}$$

where K = $\sqrt{3/2}$. The next step is to transform the current to synchronous coordinates, but then the angle of the flux must be known. The estimated value of the angle Θ is calculated by integrating the estimated rotational speed of the flux $\hat{w_f}$ as

$$\Theta = \frac{1}{s}\hat{w_f}, \tag{6.12}$$

where the rotational speed of the flux is estimated as

$$\hat{w_f} = w_r + \frac{R_R i_q}{\Psi_R}. \tag{6.13}$$

Here, i_q is the current in the q-direction in the stator and Ψ_R is the estimated flux in the rotor.

Knowing the value of the angle Θ, the currents in the rotating frame can be calculated as

$$\begin{aligned} i_d &= i_\alpha \cos\Theta + i_\beta \sin\Theta \\ i_q &= -i_\alpha \sin\Theta + i_\beta \cos\Theta \end{aligned} \tag{6.14}$$

From the input signals, the reference value of the torque is known. The reference current in q-direction $i_{q,ref}$ needed to obtain this torque is calculated as

$$i_{q,ref} = \frac{T_{el,ref}}{\Psi_R}. \tag{6.15}$$

The reference value of the current in the d-direction is determined using the reference value for the flux in the machine as

$$i_{d,ref} = \frac{1}{L_M}\Psi_{R,ref}. \tag{6.16}$$

Knowing the reference values for the currents $\mathbf{i_{dq,ref}} = i_{d,ref} + j \cdot i_{q,ref}$, the closed loop current control gives the voltages that should be applied at the generator. The applied currents in dq-coordinates are calculated as

$$\mathbf{v_{dq}} = (\mathbf{i_{dq,ref}} - \mathbf{i_{dq}})(k_{p,i} + \frac{k_{i,i}}{s}) + \mathbf{i_{dq}}(R_{filt} - R_a + j\omega_r(L_{filt} + L_{sigma})) + j\omega_r\Psi_R. \tag{6.17}$$

Here, in addition to the closed-loop current control, terms are added to compensate for the filter inductance L_{filt} and resistance R_{filt} and also introducing a feed forward term using R_a and L_{sigma}. Finally the term $\omega_r \Psi_R$. compensates for the back-emf. The values of the control parameters R_a, $k_{p,i}$ and $k_{i,i}$ are calculated for the bandwidth α_c of the controller as

$$\begin{aligned} R_a &= \alpha_c L_{sigma} - R_S - R_R \\ k_{p,i} &= \alpha_c L_{sigma} \\ k_{i,i} &= \alpha_c^2 L_{sigma} \end{aligned} \tag{6.18}$$

A voltage limitation is inserted for $\mathbf{v_{dq}}$, depending on the DC link voltage, and also an anti-windup is introduced in the closed loop current control. Then the voltages in dq-coordinates must be transformed back to the phase voltages v_a, v_b and v_c as

$$\begin{aligned} v_\alpha &= v_d \cos\Theta - v_q \sin\Theta \\ v_\beta &= v_d \sin\Theta + v_q \cos\Theta \end{aligned} \tag{6.19}$$

$$\begin{bmatrix} v_a \\ v_b \\ v_c \end{bmatrix} = \frac{1}{K} \begin{bmatrix} \frac{2}{\sqrt{3}} & 0 \\ -\frac{1}{\sqrt{3}} & 1 \\ -\frac{1}{\sqrt{3}} & -1 \end{bmatrix} \begin{bmatrix} v_\alpha \\ v_\beta \end{bmatrix}. \tag{6.20}$$

These voltages are inputs to the ideal voltage sources when using the ideal model, and for the switching model they are inputs to the calculation of the duty cycle for the transistors.

As seen in the previous equations, the value of the flux Ψ_R is used in the calculations. This value is not measured in the machine, instead it is estimated from the measured currents. As seen in [57], there are several ways to estimate the flux. Since it is assumed that the speed is known in this case, the “current model” is used, where the flux can be estimated using the current in d-direction as

$$\Psi_R = \frac{R_R L_M}{L_M s + R_R} i_d. \tag{6.21}$$

In the same way as for the control of the generator in Simulink, the control of the generator must be fast enough for the electrical torque to follow the reference value. As shown for the Simulink model, a rise time for the closed loop system of 22 ms should give sufficient stability for the controller in case of a switching frequency of 2 kHz. The reference value for the torque electrical is plotted as well as the resulting electrical torque in Fig. 6.12 for the simple model and in Fig. 6.13 for the switching model.

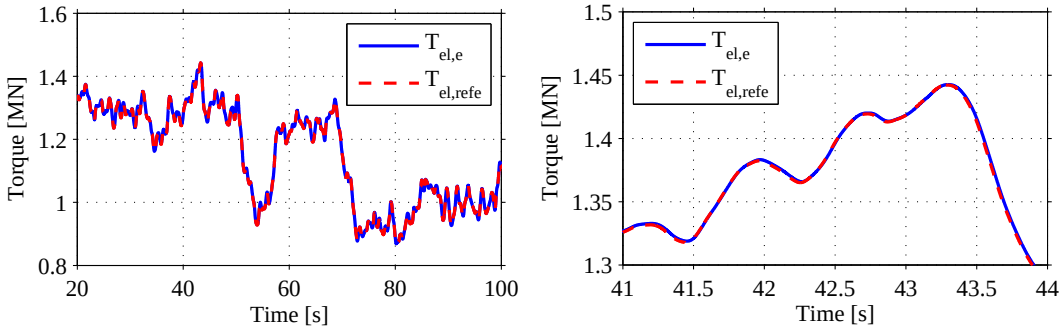

(a) Overview. (b) Zoomed figure.

Fig. 6.12 Resulting electrical torque for the simple generator model in PSCAD/EMTDC.

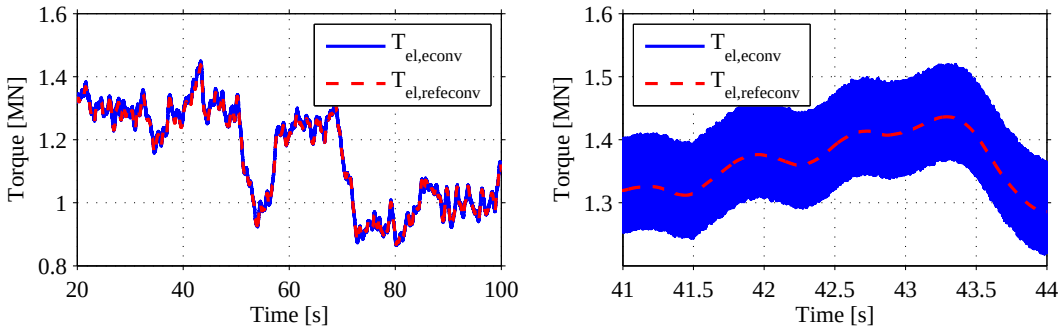

(a) Overview. (b) Zoomed figure.

Fig. 6.13 Resulting electrical torque for the switching generator model in PSCAD/EMTDC.

It can be seen that for both the simple and the switching model, the real value follows the reference value.

6.3 Control of the DC/DC Converters

The control of the DC/DC converters aims at keeping the voltages for the DC links at their rated values. For the DC link in the wind turbine, the DC/DC converter in the turbine should keep the voltage V_{11} within the allowed voltage range by controlling the output power. In the same way, the main DC/DC converter controls the voltage V_{31} for the internal DC collection bus.

The design of the control depends on the conditions for the wind farm. Here, it is assumed that the maximum allowed voltage deviations are 5 % from the rated voltage. Further, there is no communication between the converters and also no restrictions for the variations in the power from the turbines. Consequently, the system must be designed

to handle an immediate increase in the input power from zero to the rated power without exceeding the voltage limitations, and thereby the control is verified for the worst possible situation.

6.3.1 Control Methods for the DC/DC Converters

The control of the DC/DC converters is done in the same way for all simulation models seen in Fig. 6.14. The control aims at controlling the duty cycle D for the switching PSCAD model and the ratio n_1 of the "variable transformer" used in the Simulink model and the simple model in PSCAD. For the models in PSCAD, the resistance R_{in} is neglected and consequently V_{11c} is equal to V_{11}.

For the DC links, the allowed voltage range is ± 5 % from the nominal voltage. Consequently, the voltage band for the DC link in the turbine is from 1425 V to 1575 V, the voltage for the DC bus is from 30.4 to 33.6 kV and the voltage for the HVDC connection is between 123.5 kV and 136.5 kV. At startup of the system, the voltage levels can be lower while the DC links are charged.

As shown in [17], the design of the voltage controller is dependent both on the possible bandwidth and the capacitance for the DC link. Here, the possible bandwidth of the system will be investigated as well as the required DC link capacitances to keep the DC link voltages within the desired voltage levels. First, the control of the voltage level will be investigated assuming an ideal control of the output current. Then, the control of the output current is investigated. These control methods are the same for both the main DC/DC converter and the DC/DC converter in the wind turbine.

Control of the DC link voltage

The control of the DC link voltage in DC systems have been studied previously in [17, 58] for multi terminal DC systems. However, it was assumed that the control of the DC link voltage was achieved by the sources feeding power to the DC bus. In the case with the DC grid for the wind farm, the voltage level is instead controlled by the load converter during normal operation.

For controlling the voltage at the DC link, a droop controller can be used as described in [17], and the principle of the droop controller is shown in Fig. 6.15.

In the figure, it can be seen how the current for the converter controlling the DC link voltage depends on the voltage level. It should be noted that the reference direction of the current is into the DC link. If the regulating converter acts as a load with negative input current, an increased voltage level, resulting from a net increase of the power flow

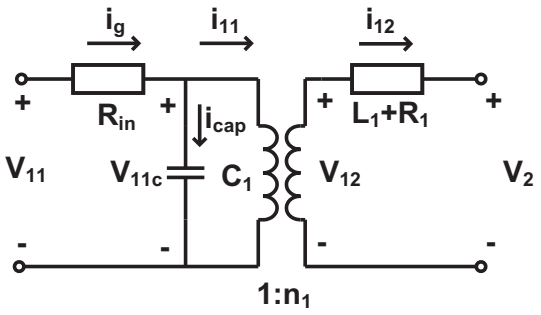

(a) Model in Simulink.

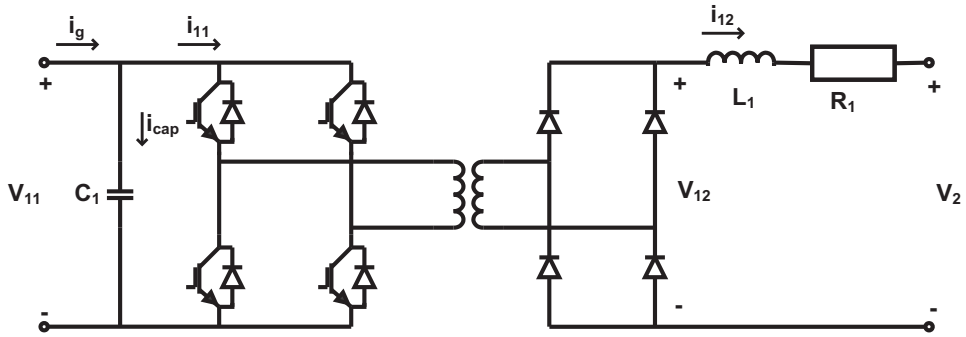

(b) Switching model in PSCAD/EMTDC.

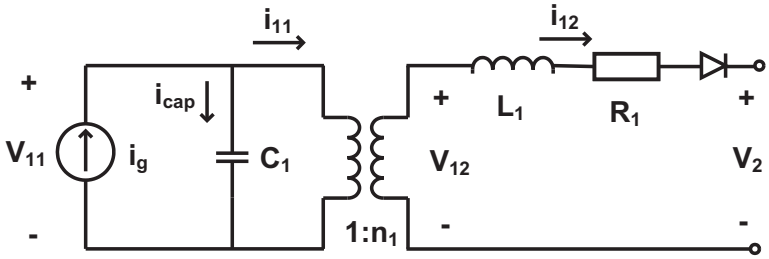

(c) Simple model in PSCAD/EMTDC.

Fig. 6.14 The different simulation models for the DC/DC converter.

into the system, will increase the output current from the DC link. In the same way, a converter acting as a source will decrease the input current due to an increased voltage level. Consequently, the same control is used both when the converters that control the voltage level act as sources and when they act as loads. The difference will be that the deviation from the reference voltage will be negative if the sources control the voltage level and positive if the loads are controlling the voltage level. In [17], the sources control the input power depending on the power to the load, resulting in a voltage level slightly below the reference voltage. For the DC bus in the wind farm, instead the load controls its transferred power depending on the input power from the turbines. The resulting closed loop control system is shown in Fig. 6.16. Here, the negative sign for the gain $K_{p,v}$ is due to the positive value for the output current.

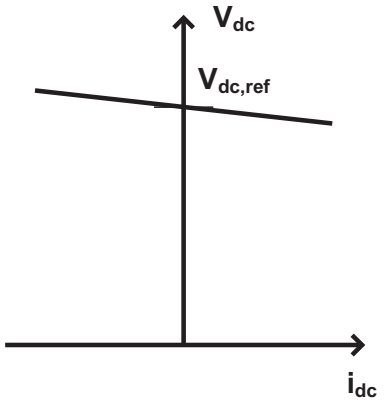

Fig. 6.15 Droop control for controlling the voltage for a DC link.

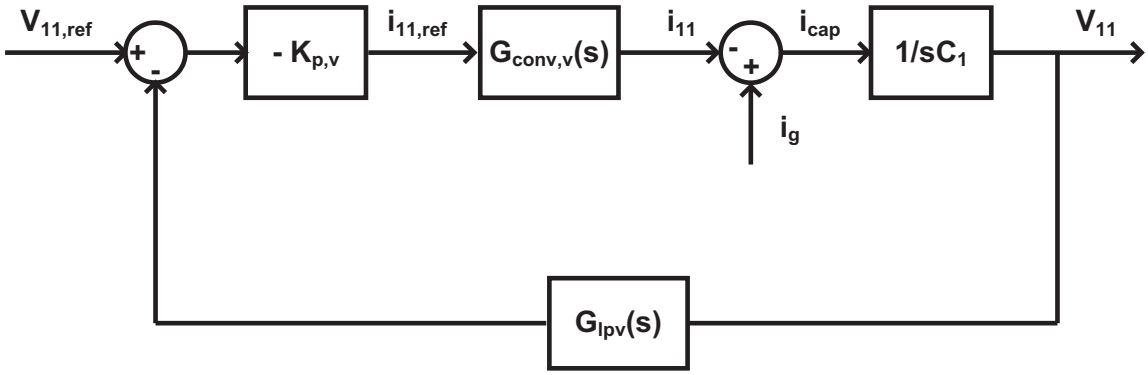

Fig. 6.16 Closed loop control system for control of the DC link voltage V_{11}.

The input value to the controller is the reference value $V_{11,ref}$ for the DC link voltage. Subtracting the measured DC link voltage V_{11}, passed through a low pass filter, gives the error signal. The low pass filter $G_{lpv}(s)$ has the transfer function

$$G_{lpv}(s) = \frac{\omega_{lp,v}}{s + \omega_{lp,v}}. \tag{6.22}$$

The error signal is the input to the controller, which in this case is a P-controller $K_{p,v}$. As previously mentioned, when controlling the voltage with the load converter instead of the source converter, the P-controller must reverse the sign of the error. Since the current that is controlled is the output current from the DC link instead of the input current, the value should increase if the voltage level is too high. The output is the reference value $i_{11,ref}$ for the input current to the converter. The reference input current is the input signal to the current control of the converter $G_{conv,v}(s)$, where the output is the real input current i_{11}. When investigating the dynamics of the voltage control, the current control is assumed to

be ideal and thereby i_{11} is the same as $i_{11,ref}$. Making this assumption, the dynamics of the voltage controller must be chosen to be considerably slower than the dynamics of the current controller. Also in [59], it is stated that the converter dynamics can be neglected if the bandwidth of the converter is considerably higher than the bandwidth of the voltage controller. The current i_{cap} to the capacitor is given by the difference between the current i_g from the generator and the current i_{11} to the converter. From the current i_{cap} to the capacitor, the voltage V_{11} is obtained as

$$V_{11} = i_{cap}\frac{1}{sC_1}. \tag{6.23}$$

Assuming an ideal current controller, the closed loop function of the voltage controller $G_{v,cl}$ can be written as [17]

$$G_{v,cl}(s) = \frac{(s+\omega_{lp,v})(-K_{p,v}/C_1)}{s^2 + s\omega_{lp,v} + \omega_{lp,v}(-K_{p,v}/C_1)}. \tag{6.24}$$

Assuming an input current i_g from the turbine, the DC link voltage V_{11} can be expressed as

$$V_{11}(s) = \frac{(s+\omega_{lp,v})(K_{p,v}/C_1)}{s^2 + s\omega_{lp,v} + \omega_{lp,v}(K_{p,v}/C_1)}V_{11,ref}(s) + \frac{(s+\omega_{lp,v})/C_1}{s^2 + s\omega_{lp,v} + \omega_{lp,v}(K_{p,v}/C_1)}i_g(s). \tag{6.25}$$

Looking at the transfer function $G_{v,cl}$, the characteristic polynomial $p(s)$ is given as

$$p(s) = s^2 + s\omega_{lp,v} + \omega_{lp,v}K_{p,v}/C_1. \tag{6.26}$$

Assuming a bandwidth of $\omega_{n,v}$ and a damping of ζ, the characteristic polynomial can be expressed as

$$p(s) = s^2 + s2\omega_{n,v}\zeta + \omega_{n,v}^2. \tag{6.27}$$

Identifying the coefficients gives an expression for the control parameter $K_{p,v}$ depending on the chosen damping ζ as also shown in [17]

$$K_{p,v} = \frac{\omega_{lp,v}C_1}{(2\zeta)^2}. \tag{6.28}$$

In the same way, the bandwidth of the controller is given by the choice of cut off frequency $\omega_{lp,v}$ for the low pass filter as well as the damping ζ as

$$\omega_{n,v} = \frac{\omega_{lp,v}}{2\zeta}. \tag{6.29}$$

Knowing the parameters for the controller, the steady state behavior of the converter can be investigated. From (6.25), the steady state expression for the DC link voltage V_{11} can be expressed as

$$V_{11} = V_{11,ref} + \frac{i_g}{K_{p,v}}. \tag{6.30}$$

Here, it can be seen that when the current i_g from the turbine is increased, the voltage V_{11} for the DC link is also increased. This steady state increase in the voltage should be controlled to stay within the allowed voltage range. From (6.30), it can be seen that a higher value of $K_{p,v}$ would give smaller variations in the voltage level. However, as can be seen in (6.28), the value of $K_{p,v}$ depends on the bandwidth $\omega_{lp,v}$ for the low pass filter, the damping ζ and the value C_1 of the capacitor. The bandwidth of the low pass filter is limited by the bandwidth of the current controller and also the value for the damping ζ is limited. Consequently, the capacitor is the parameter that can be dimensioned to limit the voltage variations.

As seen in (6.30), the voltage increases with increasing current. Therefore, the limiting operation point for the design of the capacitor is at the rated power P_n. At this power, the voltage droop is denoted δ_n. Also, assume that the power is constant for this operating point. The load resistance R_n at rated power can be calculated as

$$R_n = \frac{V_{11,ref}}{P_n}. \tag{6.31}$$

If the current at rated power with no voltage droop is $i_{g,n}$, then the current with voltage droop $i'_{g,n}$ can be expressed as

$$i'_{g,n} = \frac{P_n}{V_{11,ref}(1+\delta_n)} = \frac{i_{g,n}}{1+\delta_n}. \tag{6.32}$$

The droop resistance, which is the relation between the current and the droop voltage as shown in [17] can then be expressed as

$$R_{droop} = \frac{1}{K_{p,v}} = \frac{V_{11,ref}}{\frac{i_{g,n}}{1+\delta_n}} = R_n(1+\delta_n)\delta_n. \tag{6.33}$$

Inserting the expression for $K_{p,v}$ from (6.28) gives

$$R_n(1+\delta_n)\delta_n = \frac{1}{K_{p,v}} = \frac{(2\zeta)^2}{\omega_{lp,v}C_1}. \tag{6.34}$$

Eliminating C_1 and inserting the expression for R_n gives

$$C_1 = \frac{4\zeta^2}{\omega_{lp,v}(1+\delta_n)\delta_n}\frac{P_n}{V_{11,ref}^2}. \tag{6.35}$$

This equation can then be used to choose the value of C_1 that limits the voltage droop δ_n to a certain value for the rated power P_n.

Further, an integral part $K_{i,v}$ can be added to the controller to eliminate the steady state error, and the resulting control function $F_v(s)$ can then be written as

$$F_v(s) = K_{p,v} + \frac{K_{i,v}}{s}. \tag{6.36}$$

Then, the closed loop transfer function for the system $G_{v,cl}(s)$ can be written as

$$G_{v,cl}(s) = \frac{-(K_{p,v}s + K_{i,v})(s+\omega_{lp,v})/C_1}{s^3 + \omega_{lp,v}s^2 - \frac{K_{p,v}\omega_{lp,v}}{C_1}(s) - \frac{K_{i,v}\omega_{lp,v}}{C_1}}. \tag{6.37}$$

As shown in [16], The close loop transfer function should have a characteristical polynomial given by

$$p(s) = s^3 + \omega_{lp,v}s^2 - \frac{K_{p,v}\omega_{lp,v}}{C_1}s - \frac{K_{i,v}\omega_{lp,v}}{C_1} = (s^2 + 2\zeta\omega_{n,v}s + \omega_{n,v}^2)(s+\omega_{n,v}). \tag{6.38}$$

The parameters will then be

$$\omega_{n,v} = \frac{\omega_{lp,v}}{1+2\zeta}, \quad K_{p,v} = \frac{\omega_{lp,v}C_1}{1-2\zeta}, \quad K_{i,v} = \frac{\omega_{n,v}^3 C_1}{\omega_{lp,v}}. \tag{6.39}$$

Control of the output current

As seen in Fig. 6.16, the voltage control assumes that the real value of the current in the output inductor of the converter follows the reference value. To be able to obtain this, a current controller is needed that is considerably faster than the voltage controller. The aim of the current controller is to control the current i_{12} as seen in Fig. 6.14 (a). In Fig. 6.17, the closed loop transfer function of the current controller is shown.

The input value to the current controller is the reference value $i_{12,ref}$, which is obtained from the reference current $i_{11,ref}$ as

$$i_{12,ref} = \frac{i_{11,ref}}{n_1}. \tag{6.40}$$

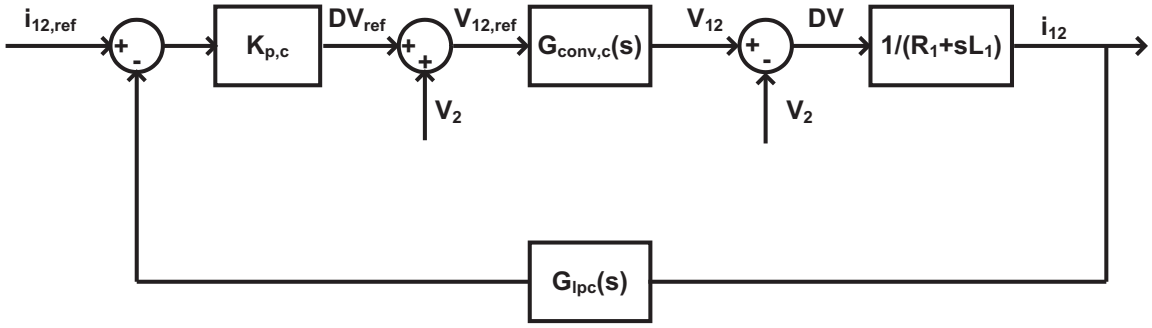

Fig. 6.17 Closed loop control system for control of the current i_{12} in the filter inductance.

The controller is designed in the same way as the voltage controller. The difference between the reference current $i_{12,ref}$ and the real current i_{12} is the error signal in to the controller $K_{p,c}$. The output is the reference value DV_{ref} for the voltage DV applied across the inductor L_1 and the resistor R_1. Here, the transfer function $G_{conv}(s)$ represents the characteristics of the converter from the reference value DV_{ref} of the voltage across R_1 and L_1 to the real value DV. Also for the current control, the low pass filter $G_{lpc}(s)$ has the transfer function

$$G_{lpc}(s) = \frac{\omega_{lp,c}}{s + \omega_{lp,c}}. \tag{6.41}$$

Assuming the converter to be ideal ($G_{conv,c}(s)$ = 1), the closed loop transfer function $G_{c,cl}(s)$ for the current control can be written as

$$G_{c,cl}(s) = \frac{K_{p,c}s + \omega_{lp,c}K_{p,c}}{L_1 s^2 + (R_1 + L_1\omega_{lp,c})s + \omega_{lp,c}(R_1 + K_{p,c})}. \tag{6.42}$$

For this transfer function, the characteristic polynomial $p(s)$ is given by

$$p(s) = L_1 s^2 + (R_1 + \omega_{lp,c})s + \omega_{lp,c}(R_1 + K_{p,c}). \tag{6.43}$$

Assuming a bandwidth of $\omega_{n,c}$ and a damping of ζ, the characteristic polynomial can be expressed as

$$p(s) = s^2 + s2\omega_{n,c}\zeta + \omega_{n,c}^2. \tag{6.44}$$

Set the coefficients equal, the bandwidth of the low pass filter $\omega_{lp,c}$ is given by

$$\omega_{lp,c} = 2\zeta\omega_{n,c} - \frac{R_1}{L_1}, \tag{6.45}$$

and the control parameter $K_{p,c}$ can be expressed as

$$K_{p,c} = \frac{\omega_{n,c}^2 L_1}{\omega_{lp,c}} - R_1. \tag{6.46}$$

6.3.2 Design of the Controller and the DC Link Capacitance

In the previous section, the choice of control parameters is discussed based on the desired bandwidths $\omega_{n,c}$ and $\omega_{n,v}$ as well as the damping ζ of the controllers assuming that the converter is ideal. This designs of the controllers are valid if the controllers are slow compared to the dynamics of the converter. For the current controller, the voltage DV must follow the reference value fast compared to the control of the converter, and in the same way the current controller must be fast compared to the voltage controller. Here, first the current controller is investigated to determine the speed of the controller. Knowing the bandwidth of the current controller, the possible bandwidth of the voltage controller can be determined. This is done both for the DC/DC converter in the wind turbine and the main DC/DC converter for the whole wind farm.

Design of the Current Controller

Starting with the current controller, it is assumed that the average voltage applied across the inductor L_1 and the resistor R_1 follows the reference voltage immediately. However, as discussed for the control of the generator, this is not true for the real converter. First, there is a delay of half a switching period since PWM control is used and then there is also some additional delay for measuring the real current and calculating all values. Assuming that the total delay for the converter is one switching period (1 ms), the transfer function $G_{conv,c}(s)$ can be assumed to be a delay of 1 ms as

$$G_{conv,c}(s) = e^{-sT_d}, T_d = 1ms. \tag{6.47}$$

To find suitable control parameters, the step response of the system is studied both with the ideal converter model and with the delay inserted (using Padé approximation). Starting with the damping, it is assumed that $\zeta = 1/\sqrt{2}$ is a suitable value. Regarding the bandwidth of the controller, the low pass filter should be able to filter the ripple from the switching of the converter at 1 kHz. As shown above, the bandwidth of the low pass filter $\omega_{lp,c}$ for the current controller is given by

$$\omega_{lp,c} = 2\zeta\omega_{n,c} L_1 - R_1. \tag{6.48}$$

Starting with the DC/DC converter in the wind turbine, choosing $\omega_{n,c}$ = 800 rad/s as

the bandwidth for the current controller, the resulting bandwidth of the low pass filter is $\omega_{lp,c}$ = 1131 rad/s using L_1 = 0.3 H and R_1 = 0.03 Ω. Using (6.46), the resulting control parameter is $K_{p,c}$ = 170 for the wind turbine DC/DC converter. Both the bandwidth of the low pass filter and the control parameter are the same for the main DC/DC converter since the output inductance is the same for both converters. The resulting time step is plotted in Fig. 6.18 for both the ideal model and the model with the time delay.

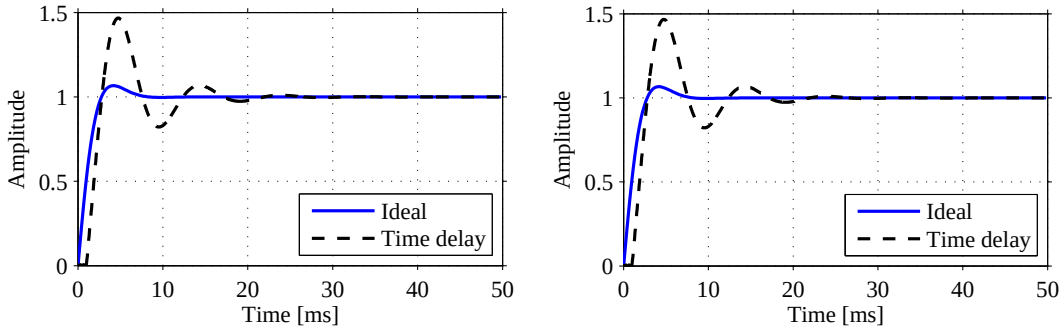

(a) Wind turbine DC/DC converter.

(b) Main DC/DC converter.

Fig. 6.18 Step response for the closed loop current controller using $\omega_{n,c}$ = 800 rad/s.

In the figure, it can be seen that for the ideal converter, the step response has a rise time of just below 3 ms and is well damped. However, for the system with the time delay of 1 ms, the overshoot for the current is 1.5, which is considered to be too high.

Decreasing the bandwidth of the system to $\omega_{n,c}$ = 500 rad/s results in $\omega_{lp,c}$ = 707 rad/s and $K_{p,c}$ = 106 for both converters. This gives the step responses for both the ideal system and the system with the delay as shown in Fig. 6.19.

Here, it can be seen that the overshoot of the current is decreased from almost 1.5 using $\omega_{n,c}$ = 800 rad/s to below 1.3 for $\omega_{n,c}$ = 500 rad/s.

The choice of control parameters for the current controller should aim at a closed loop control that is as fast as possible but still stable. From the figures, it can be seen that the controller using $\omega_{n,c}$ = 500 rad/s gives a stable control with limited overshoot.

The control described above is dependent on that the reference value of the voltage applied across L_1 and R_1 is followed closely. For the real converter, this is not the case and the controller will not have the same characteristics as shown in the figures above. Using the switching model will give different results compared to using an ideal transformer with ratio n_1 equal to the reference value of the duty cycle. For the real converter, there

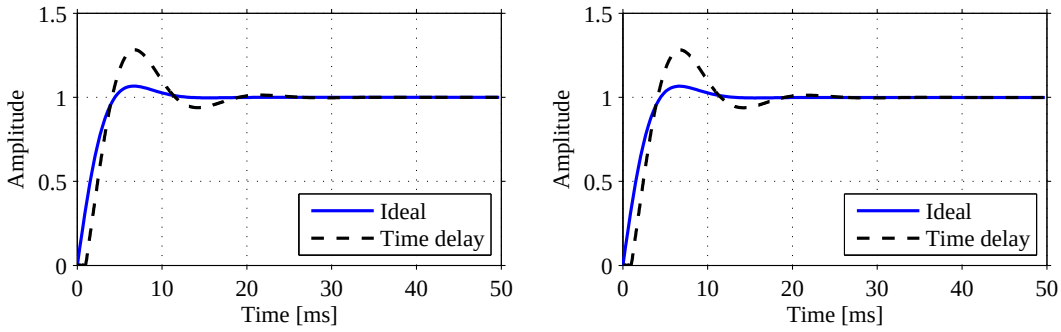

(a) Wind turbine DC/DC converter.

(b) Main DC/DC converter.

Fig. 6.19 Step response for the closed loop current controller using $\omega_{n,c}$ = 500 rad/s.

will be some loss in duty cycle due to blanking times and the time for reversing the current in the transformer. These factors will result in a ratio between voltages V_{12} and V_{11} that deviates from n_1. Using the measured voltages, the reference value of the duty cycle can be adjusted so the real value of n_1 follows the reference value more closely for the switching model. However, there will still be deviations from the ideal model and therefore an integral part has to be inserted into the controller. The transfer function $F_c(s)$ for the current controller will change from $K_{p,c}$ to

$$F_c(s) = K_{p,c} + \frac{K_{i,c}}{s}. \tag{6.49}$$

Using the value $K_{i,c}$ = 1000 will not change the step response noticeable, but will eliminate remaining errors due to non-ideal parameters of the converter.

Design of the Voltage Controller

The next step is to determine the parameters for the voltage controller. As seen above, the parameters for the current controller was chosen to give a bandwidth of 500 rad/s for the closed loop system. Therefore, the ideal converter model $G_{conv,v}$ in the voltage controller can be replaced with a low pass filter with the bandwidth of $\omega_{n,c}$ = 500 rad/s as

$$G_{conv,v} = \frac{\omega_{n,c}}{s + \omega_{n,c}}. \tag{6.50}$$

As noted previously, the capacitor value of the DC link should be determined to limit the droop voltage, and it is calculated by

$$C_1 = \frac{4\zeta^2}{\omega_{lp,v}(1+\delta_n)\delta_n} \frac{P_n}{V_{11,ref}^2}. \tag{6.51}$$

Here, the same damping $\zeta = 1/\sqrt{2}$ is used as for the current controller and the bandwidth of the system is set to $\omega_{n,v}$ = 500 rad/s. Further, the rated power is P_n = 2.3 MW, the rated voltage is $V_{11,ref}$ = 1.5 kV and the maximum droop is δ_n = 0.05 for the DC/DC converter in the wind turbine. The bandwidth of the low-pass filter is then $\omega_{lp,v}$ = 707 rad/s. The resulting capacitor value is then C_1 = 61 mF and $K_{p,v}$ = 21.5. For the main DC/DC converter, the rated power is P_n = 110 MW, the rated voltage is $V_{31,ref}$ = 32 kV and the maximum droop is δ_n = 0.05. The resulting capacitor value is then C_3 = 6.4 mF, and the control parameters are $K_{p,v}$ = 2.27 and $\omega_{lp,v}$ = 707 rad/s. The resulting step response is seen in Fig. 6.20.

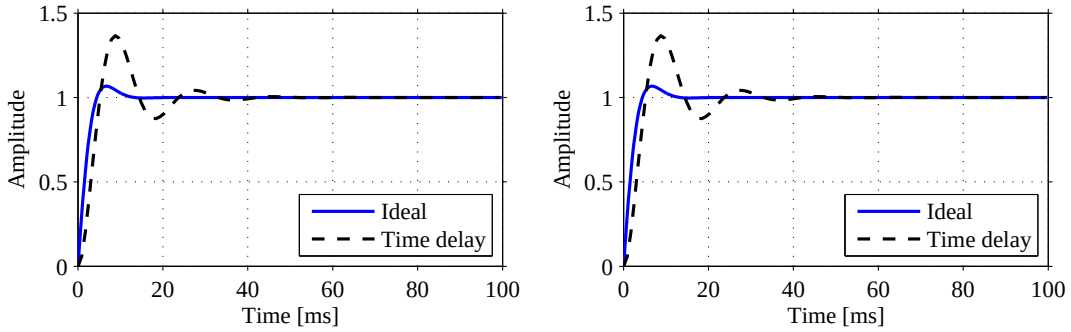

(a) Wind turbine DC/DC converter.

(b) Main DC/DC converter.

Fig. 6.20 Step response for the closed loop voltage controller using $\omega_{n,v}$ = 500 rad/s.

Here, the overshoot of the voltage is 1.4, which is considered to be to high. Further, the bandwidth of the system is lowered to $\omega_{n,v}$ = 200 rad/s and the bandwidth of the low pass filter is $\omega_{lp,v}$ = 283 rad/s. The resulting capacitor value for the DC/DC converter in the wind turbine is C_1 = 152 mF and the value of $K_{p,v}$ = 21.5. For the main converter, the resulting capacitor value C_3 = 16 mF and the value of $K_{p,v}$ = 2.27. Using these values for the capacitances, the stored energy in the DC links corresponds to 74 ms transferred power at full load. The resulting step response can be seen in Fig. 6.21.

For the bandwidth of $\omega_{n,v}$ = 200 rad/s for the current controller, the resulting over shoot in the voltage is limited to 1.2. Choosing the bandwidth of the voltage controller to be $\omega_{n,v}$ = 200 rad/s, the resulting DC link voltages when the output power from each turbine is increased from 400 kW to 2.3 MW are shown in Fig. 6.22.

Here, it can be seen that the steady-state voltage is kept within 5 % deviation (1575 V) from the rated voltage for steady state operation for the DC/DC converter in the wind turbine. The slope seen in the voltage is due to the integral part of the current controller.

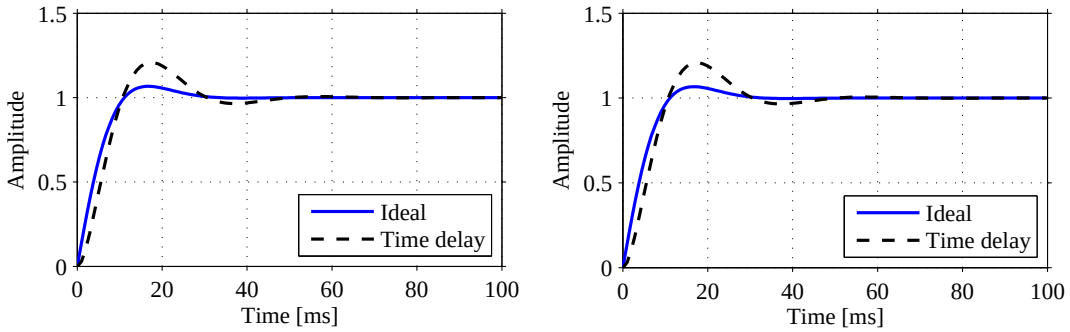

(a) Wind turbine DC/DC converter.

(b) Main DC/DC converter.

Fig. 6.21 Step response for the closed loop voltage controller using $\omega_{n,v}$ = 200 rad/s.

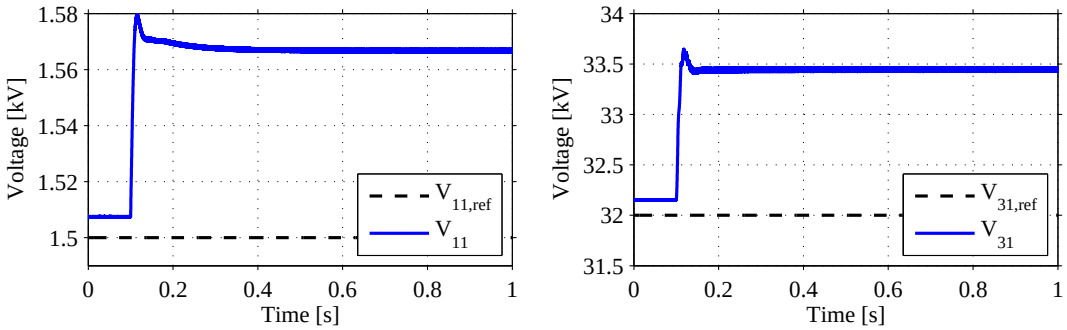

(a) DC link voltage V_{11} for the wind turbine DC/DC converter.

(b) DC bus voltage V_{31} for the main DC/DC converter.

Fig. 6.22 DC link voltage at a step in the power from 400 kW to 2.3 MW for each turbine without integral part.

Also for the main DC/DC converter, the voltage is kept below 33.6 kV that is 5 % above the rated voltage. Further, looking at the voltages at the connection point to the turbines in a radial during the sudden increase in the power, the resulting values can be seen in Fig. 6.23. Here, the voltage at turbine 1 is denoted $t1$ and similarly for turbines 4, 7 and 10 in the same radial.

It can be seen that the voltage is over the allowed 33.6 kV at the turbines in the end of the radial. However, the voltage is still below 35.2 kV that is 10 % above the reference value of the voltage, at which the converters are designed to maintain the controllability.

Further, adding an integral part to the voltage controller, the control parameters are given by

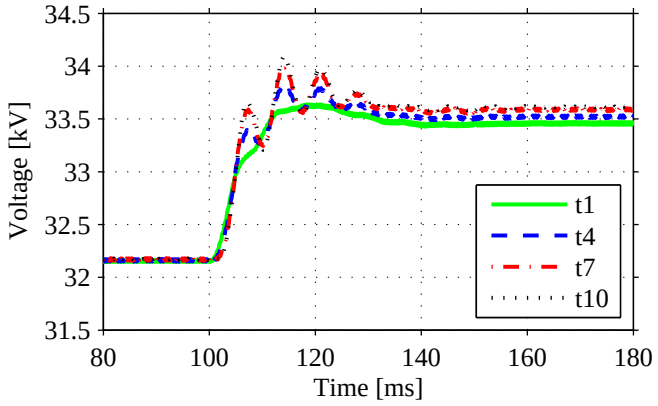

Fig. 6.23 DC bus voltage V_2 at turbines 1, 4, 7 and 10 in a radial at a step in the power without integral part.

$$\omega_{n,v} = \frac{\omega_{lp,v}}{1+2\zeta}, \quad K_{p,v} = \frac{\omega_{lp,v} C_1}{1-2\zeta}, \quad K_{i,v} = \frac{C_1 \omega_{lp,v}^2}{(1+2\zeta)^3}. \tag{6.52}$$

Having the damping ζ = 0.5 as stated in [16], the bandwidth for the controller $\omega_{n,v}$ is half of the bandwidth $\omega_{lp,v}$ of the low pass filter. For the case without integral part, $\omega_{n,v}$ is $1/\sqrt{2}$ times $\omega_{lp,v}$. However, here the bandwidth $\omega_{lp,v}$ for the low pass filter is kept constant when the integral part is added and thereby the bandwidth of the closed loop voltage controller will be larger when having the integral part. Consequently, for this controller, using the bandwidth $\omega_{lp\ ,v}$ = 283 rad/s gives $\omega_{n,v}$ = 141 rad/s, $K_{p,v}$ = 21.5 and $K_{i,v}$ = 1522. The resulting step response for the system is shown in Fig. 6.24 (a). However, since the overshoot for the step response is large, the integral part $K_{i,v}$ is lowered by a factor of 10 to $K_{i,v}$ = 152, where the resulting step response is seen in Fig. 6.24 (b). Also, the resulting voltage in the case of a step in the input power from 400 kW to 2.3 MW is shown in Fig. 6.25.

Comparing the peak values of the voltage for the case without integral part in the controller in Fig. 6.22 with the voltage using a controller with an integral part shown in Fig. 6.25, it can be seen that the peak value is slightly decreased due to the integral part. However, there is just a small decrease and therefore it can be concluded that the proportional part of the controller determines the over voltage and the capacitor value calculated for the controller without integral part can not be reduced. Consequently, choosing the controller with bandwidth $\omega_{n,v}$ = 200 rad/s, the required DC link capacitance for the wind turbine converter is C_1 = 152 mF.

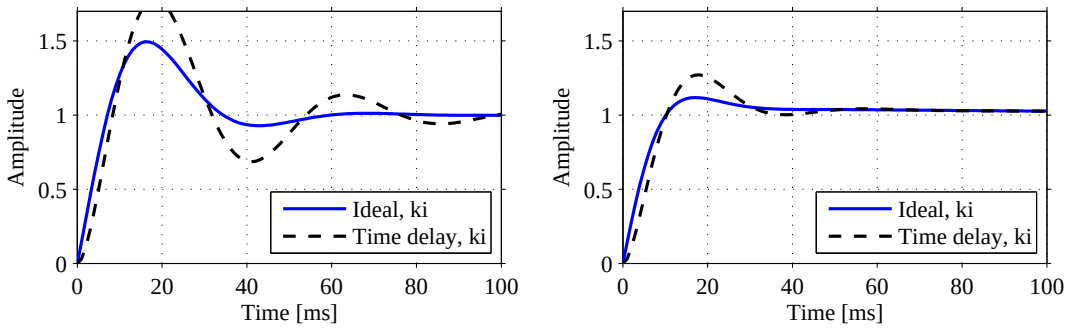

(a) $K_{i,v}$ = 1522. (b) $K_{i,v}$ = 152.

Fig. 6.24 Step response for the DC/DC converter in the wind turbine closed loop voltage controller using $\omega_{lp,v}$ = 282 rad/s.

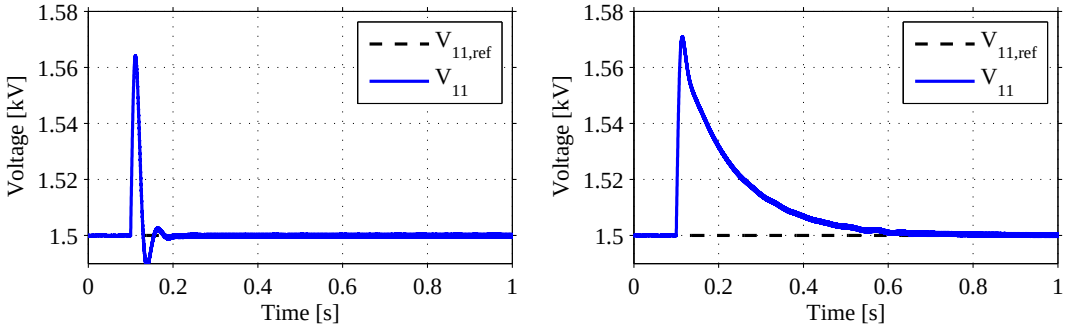

(a) $K_{i,v}$ = 1522. (b) $K_{i,v}$ = 152.

Fig. 6.25 DC link voltage V_{11} for the DC/DC converter in the wind turbine at a step in the power with integral part using $\omega_{lp,v}$ = 282 rad/s.

Inserting an integral part in the controller for the main DC/DC converter using the bandwidth $\omega_{lp\ ,v}$ = 283 rad/s results in $\omega_{n,v}$ = 141 rad/s, $K_{p,v}$ = 2.27 and $K_{i,v}$ = 160 giving the step response in Fig. 6.26 (a). Lowering $K_{i,v}$ to 16, the resulting step response is shown in Fig. 6.26 (b).

Further, the resulting DC bus voltage V_{31} is shown in Fig. 6.27, when the total power is increased from 19 MW to 110 MW. It should be noted that the total input capacitance of 16 mF for the main converter is distributed with 100 μF at the output of each wind turbine and the remaining 11.2 mF is located at the input of the main converter.

Also for the main converter, it can be seen in Fig. 6.27 that the peak value of the voltage just decrease slightly with increasing integral part. Therefore, the capacitor value calculated for the controller without the integral part should be used. Also, the lower value

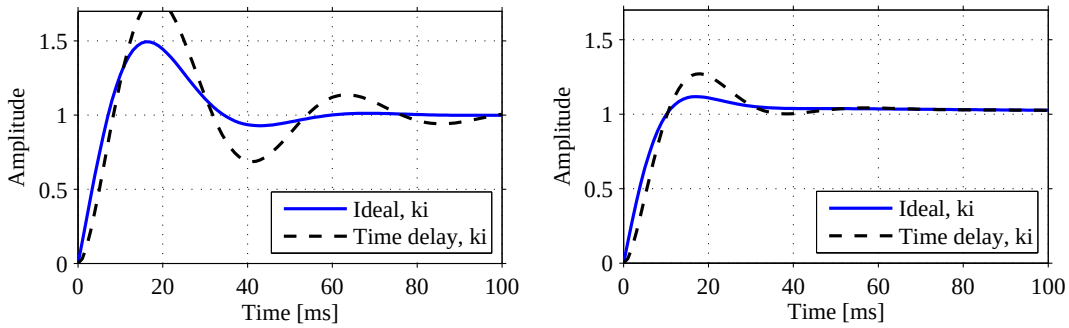

(a) $K_{i,v}$ = 160. (b) $K_{i,v}$ = 16.

Fig. 6.26 Step response for the main DC/DC converter closed loop voltage controller using $\omega_{lp,v}$ = 282 rad/s.

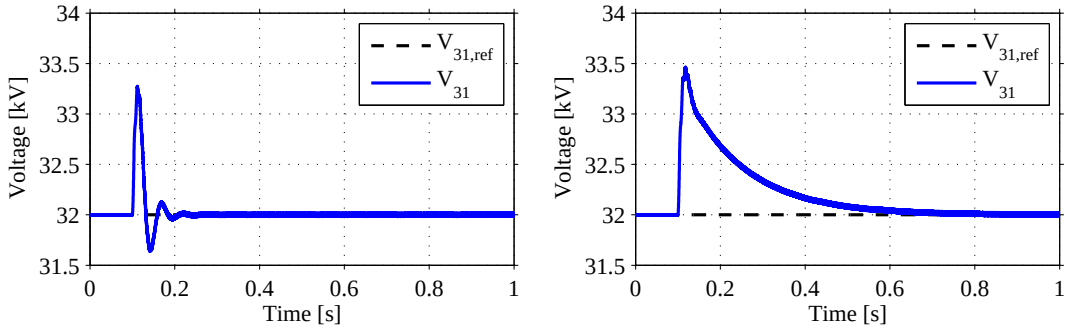

(a) $K_{i,v}$ = 160. (b) $K_{i,v}$ = 16.

Fig. 6.27 DC bus voltage V_{31} for the main DC/DC converter at a step in the power with integral part using $\omega_{lp,v}$ = 282 rad/s.

of the integral part for the controller is used as shown in Figs. 6.25 and 6.27. Finally, in Table. 6.1, the control parameters for the converters are shown.

6.3.3 Evaluation of the Controller

Evaluation for Normal Operating Conditions

For evaluating the controllers for operation in normal wind farm conditions, the input wind speed shown in Fig. 6.2 is used. It is also assumed that the same wind speed hits all turbines. In the real case, different wind speeds for the different turbines will result in smaller variations in the total input current for the main converter. The simulations are made both with and without integral part for the voltage controllers. The resulting current from one radial is shown in Fig. 6.28.

Table 6.1: Control parameters for the converters.

	Current control			Voltage control			
	$K_{p,c}$	$K_{i,c}$	$\omega_{lp,c}$	$K_{p,v}$	$K_{i,v}$	$\omega_{lp,v}$	C
Main conv.	106	100	707 rad/s	2.27	16	283 rad/s	16 mF
Turbine conv.	106	100	707 rad/s	21.5	152	283 rad/s	152 mF

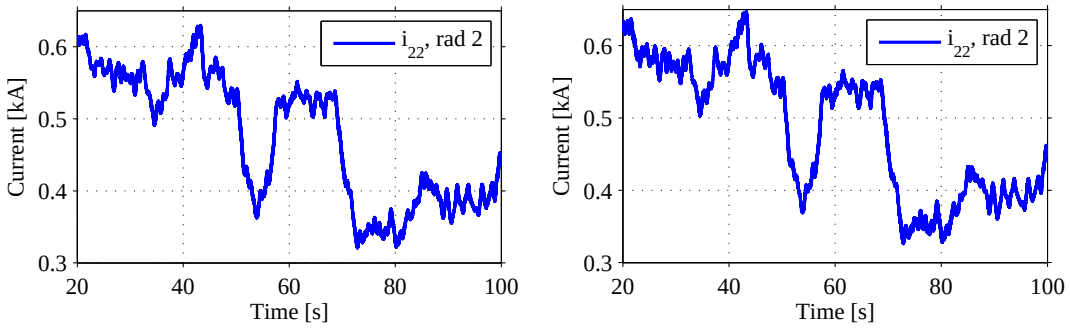

(a) Without integral part for the voltage controllers.

(b) With integral part for the voltage controllers.

Fig. 6.28 Output current i_{22} from radial 2 during normal operation.

Here, it can be seen that the current is basically the same, the small variations are depending on the different voltage levels since the power is the same. The current from one turbine is 10 % of the current from the radial.

Looking at the voltage V_{11} for the DC link in the turbine, the resulting voltage is shown in Fig. 6.29. Here, it can be seen that without the integral part, there are variations in the DC link voltage. However, the voltage stays within the limited 5 % from the rated voltage (below 1.575 kV).

In the same way, the voltage for the internal bus, controlled by the main DC/DC converter is shown in Fig. 6.30. Here, the voltage V_{31} at the main converter is shown as well as the output voltage V_2 at turbines 5 and 10.

Here, it can be seen that the voltage V_{31}, controlled by the main converter, varies depending on the current if no integral part is used. Adding the integral part eliminates these variations. The voltages at the turbines are slightly larger than the voltage at the main converter, due to the voltage drop in the cable. The further out the turbine is, the larger

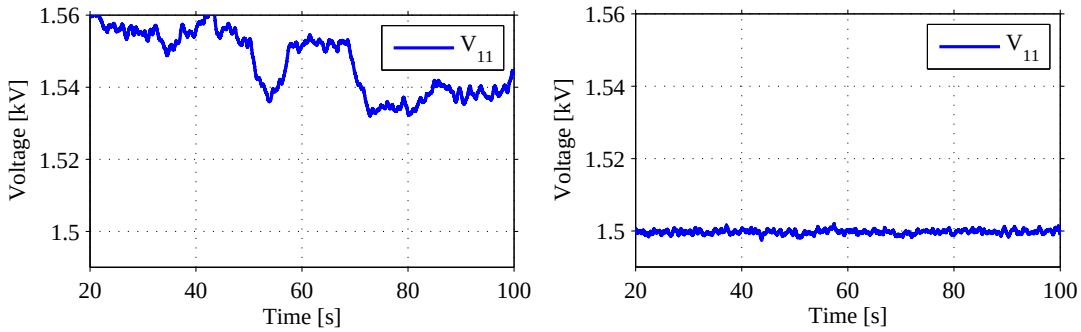

(a) Without integral part, $K_{i,v}$ = 0. (b) With integral part, $K_{i,v}$ = 152.

Fig. 6.29 Voltage V_{11} for the DC link in a turbine during normal operation.

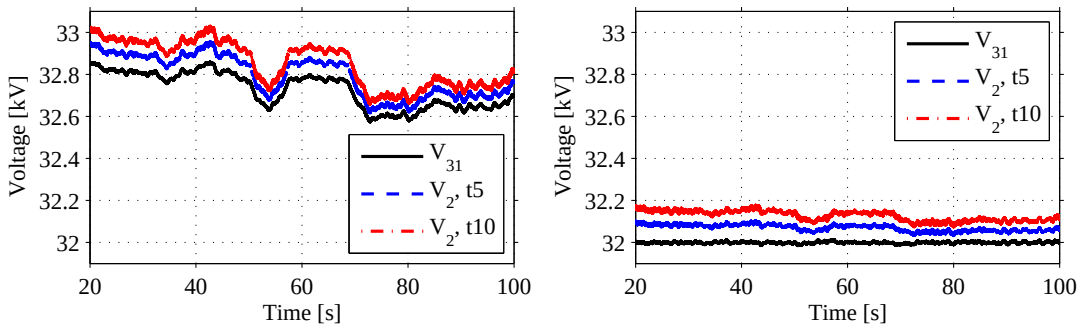

(a) Without integral part, $K_{i,v}$ = 0. (b) With integral part $K_{i,v}$ = 16.

Fig. 6.30 Voltages V_2 and V_{31} for the DC bus during normal operation.

is the voltage drop in the cable. However, this voltage drop is below 200 V for the last turbine in the radial and is then just 0.5 % of the rated voltage.

Possible Improvements of the Controller

For the voltage controller to be stable and keep the voltage variations within 5 % from the reference value, it has been shown in this section that large capacitors are needed; 16 mF for the internal DC bus in the wind farm and 152 mF for the DC link in the wind turbine with the stored energy of 74 ms of transferred rated power. These values can be lowered by increasing the bandwidth of the controller, but then the stability margin is decreased.

The control has been designed without communication between the sources and the load converter controlling the voltage for a DC link. Using communication within the wind farm and then introducing a possible feed forward between the sources and the load converter can reduce the needed capacitances for the DC links.

As stated previously, the aim of the controller is to limit the voltage within 5 % from the reference value. Assume a feed forward of the current from the sources to the load, the DC link capacitance must be designed to store the excess power during the delay before the load converter has followed a change in the input power. This delay time Δt, is the sum of the delay for the communication Δt_{com} and the time constant for the closed loop current controller Δt_{cont} as

$$\Delta t = \Delta t_{com} + \Delta t_{cont}. \tag{6.53}$$

As seen previously, the closed loop bandwidth of the current controller is $\omega_{n,c}$ = 500 rad/s, giving a rise time of less than 3 ms as shown in Fig. 6.19.

To determine the capacitance needed, the worst case is considered where the input power changes instantly from almost zero to full power. Before the increase, the DC link has the nominal voltage V_n and the nominal stored energy W_n, and the relation is depending on the value of the capacitance C as

$$W_n = \frac{1}{2} C V_n^2. \tag{6.54}$$

During the time Δt before the power flow in the load has increased, the excess energy ΔW is accumulated in the DC link capacitance. This excess energy can be expressed using the nominal power P_n as

$$\Delta W = P_n \Delta t. \tag{6.55}$$

The total energy W_{tot} can then be expressed as

$$W_{tot} = W_n + \Delta W = \frac{1}{2} C V_n^2 + P_n \Delta t = \frac{1}{2} C V_{tot}^2. \tag{6.56}$$

Eliminating the value of the capacitance gives

$$C = \frac{2 P_n \Delta t}{V_{tot}^2 - V_n^2}. \tag{6.57}$$

Assuming that V_{tot} is 5 % above V_n, the value of the capacitance C can be calculated as a function of the delay time for the communication Δt_{com}. The results are shown in Fig. 6.31.

Here, it can be seen that the DC link capacitance for each turbine is larger than for the DC

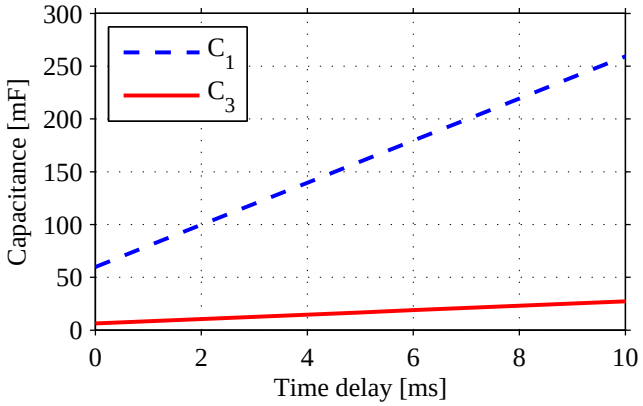

Fig. 6.31 Required value of the DC link capacitances C_1 for the wind turbine and C_3 for the DC bus as a function of the communication delay.

bus. In Table 6.2, the needed DC link capacitances are shown as a function of the communication delay. Also, the values for the needed capacitance without communication is shown. Here, it can be seen that a fast control can reduce the needed capacitance signifi-

Table 6.2: Required value of the DC link capacitances C_1 for the wind turbine and C_3 for the DC bus as a function of the communication delay.

Δt_{com}	C_1	C_3
1 ms	80 mF	8.4 mF
5 ms	160 mF	16.8 mF
10 ms	260 mF	27.2 mF
no comm.	152 mF	16 mF

cantly. If the communication is faster than 4.5 ms, the capacitance can be lower than for the case without communication between the sources and the load converter.

There is also a possibility to reduce the required DC link capacitance by using the integral part of the controller. As seen in Figs. 6.25 and 6.27, an integral part reduces the steady state voltage deviations but the peak voltage is still high. One possibility to reduce the DC link capacitance is to temporarily allow peak voltages up to 10 % above the reference value during very fast variations in the input power. If also the variations in the input power from the wind turbines are limited, the peaks in the voltage are eliminated and the value of the capacitor can be further reduced. Another option can also be to have a breaker resistance to reduce peak over voltages. However, it should be noted that the integral part of the controller is suitable when just one converter controls the voltage of the DC link. If

instead the power flow is limited for the HVDC link and the wind turbines must control the power for the DC bus, it is more complicated to use an integral part for the controller.

Large Signal Stability for the DC Bus

For distributed converters supplying a constant load, the large signal stability is shown in [16, 58, 60], and a simplified figure of the system with one load is seen in Fig. 6.32.

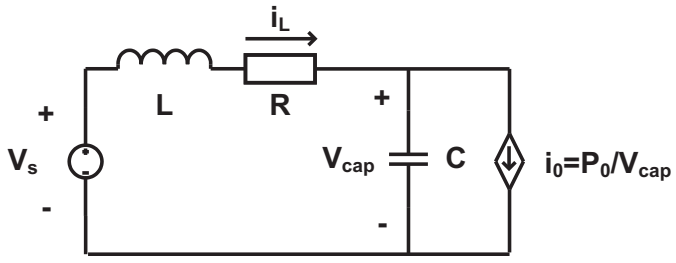

Fig. 6.32 Circuit used in the derivation of the large signal analysis.

In this circuit, a constant voltage source V_s is connected to a DC bus with an input inductance L and resistance R in series and then a shunt capacitance C supplying a constant load P_0. As shown in [58], the equilibrium point for the circuit is found using the state equations

$$\frac{dV_{cap}}{dt} = \frac{1}{C}\left(i_L - \frac{P_0}{V_{cap}}\right) \tag{6.58}$$

$$\frac{di_L}{dt} = \frac{1}{L}\left(V_s - Ri_L - V_{cap}\right). \tag{6.59}$$

Using these equations and eliminating the state variables i_L and V_{cap}, the result is

$$V_{cap} = \frac{V_s}{2} \pm \sqrt{\frac{V_s}{2}^2 - RP_0} \tag{6.60}$$

$$I_L = \frac{P_0}{V_{cap}}. \tag{6.61}$$

Here, the operating point is real if RP_0 is small enough, leading to the upper limit of R as

$$R < \frac{V_{cap}^2}{4P_0}. \tag{6.62}$$

In [58], a safety factor of two is inserted, giving a resulting limit for the resistance as

$$R < \frac{V_{cap}^2}{8P_0}. \tag{6.63}$$

Also, a lower limit of the value for the resistance is found in [58] using the mixed potential criterion. Using the circuit shown in Fig. 6.32, the lower limit for the resistance, as shown in [16, 58], is given by

$$R > \sqrt{\frac{L}{C}}. \tag{6.64}$$

For the case with the DC grid for the wind farm, a single turbine connected to the main converter is considered. Instead of a constant power load as the case shown in Fig. 6.32, the turbine can be seen as a constant power source. Since the current in the output inductance is controlled for each wind turbine DC/DC converter, it can be seen as a current source. Further, the turbine is connected to the output capacitance and then connected by the DC bus to the main capacitance. However, since the voltage at the input capacitance to the main converter is voltage controlled, it can be assumed to be a constant voltage source.

Comparing the circuit in Fig. 6.32 to the DC grid in the wind farm, shown in Fig. 6.33, the same circuit can be used if the power P_0 is negative. Then assuming that the output current from the wind turbine DC/DC converter i_{12} is the same as i_0, the capacitor C has the value C_{21} and the cable parameters R and L are equal to R_2 and L_2. Further, the voltage V_s is the input voltage V_{31} for the main converter.

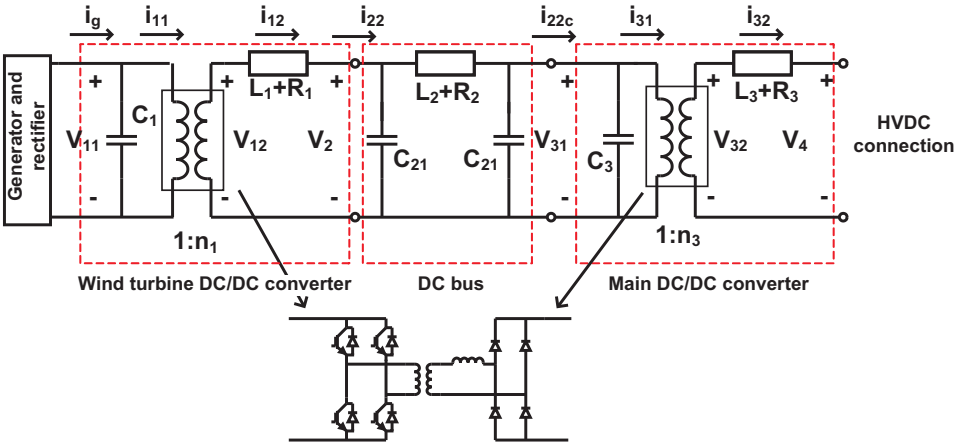

Fig. 6.33 The equivalent circuit of the internal DC grid.

Starting with the upper limit for the cable resistance, it was originating from the real state condition for the voltage v as

$$V_{cap} = \frac{V_s}{2} \pm \sqrt{\frac{V_s}{2}^2 - RP_0}. \tag{6.65}$$

However, for the DC grid system, the power P_0 is negative, and therefore the voltage V_{cap} is real for all values of the cable resistance R.

Continuing with the lower limit of the cable resistance, it is given by

$$R > \sqrt{\frac{L}{C}}. \tag{6.66}$$

The resistance in the radial from a turbine to the main converter is depending on the location of the turbine in the radial. Here it is assumed that there is 500 m between each turbine and 1000 m between the first turbine and the main converter. For the first turbine in the radial, the resistance is just 48 mΩ, while the resistance for the last turbine is 650 mΩ. Also, the inductance varies between 170 nF and 695 nF. Looking at one turbine that each have an output capacitance of 100 μF, the minimum value for the cable resistance is for the first turbine

$$R > \sqrt{\frac{L}{C}} = \sqrt{\frac{170 \cdot 10^{-9}}{100 \cdot 10^{-6}}} = 41m\Omega, \tag{6.67}$$

and for the last turbine

$$R > \sqrt{\frac{L}{C}} = \sqrt{\frac{695 \cdot 10^{-9}}{100 \cdot 10^{-6}}} = 83m\Omega, \tag{6.68}$$

Here, it can be seen that the cable resistance is large enough for both the first and the last turbine.

6.4 Experimental Verification of the Control

The design of the controllers for the DC/DC converters in the wind farm is here verified using the down scaled experimental setup presented in Section 3.4. The aim is to design a controller for the experimental setup and verify the simulations against measurements. Using state-space averaging of the switching period for the converter shown in Fig. 3.14, the simplified circuit shown in Fig. 6.34 is obtained.

In the simplified circuit, the input voltage source and capacitance C_{in} is replaced with the ideal voltage source V_{in}. Further, the leakage inductance for the transformer is neglected.

The controller of the circuit is designed in the same way as the controller for the full-scale converter with an outer voltage control and an inner current control loop as shown

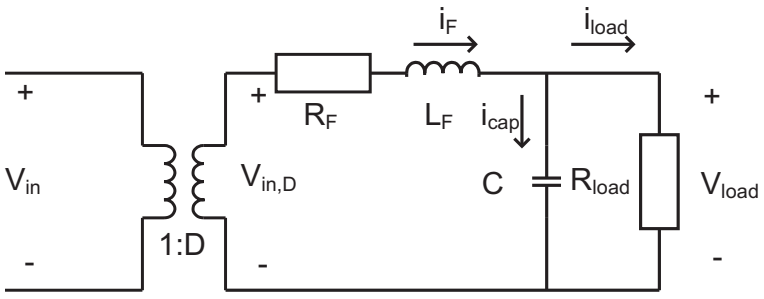

Fig. 6.34 Simplified circuit for the experimental converter using state space averaging.

in Section. 6.3.1. Looking at Fig. 6.34, the load voltage V_{load} is controlled by controlling the current that is charging/discharging the capacitance C. The output from the current controller is the reference value for the filter current i_F, which is controlled by the inner current control loop. Since the current control loop determines the conditions for the voltage controller, the design of the current controller will be determined first.

Using the voltage V_{load} across the load resistance and the input voltage on the secondary side of the H-bridge $V_{in,D}$, the current can be expressed as

$$DV = V_{in,D} - V_{load} = i_F R_F + L_F \frac{di_F}{dt}. \tag{6.69}$$

The transfer function from DV to i_F can then be expressed as

$$i_F = DV \frac{1}{L_F s + R_F}. \tag{6.70}$$

Using a closed loop control of the output voltage V_{load} with a low pass filter for the measured signal, the resulting control system is shown in Fig. 6.35.

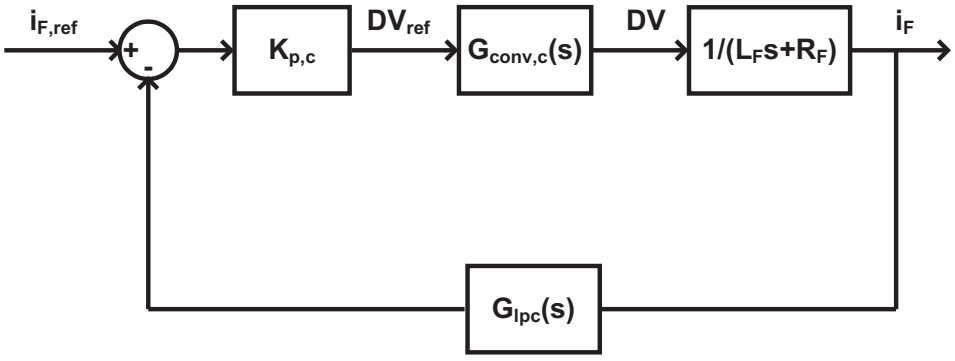

Fig. 6.35 Closed loop control system for control of the filter current i_F.

The input value to the controller is the reference value $i_{F,ref}$ for the filter current. Subtracting the measured filter current, passed through a low pass filter, gives the error signal that is the input to the controller. The low pass filter $G_{lpc}(s)$ has the transfer function

$$G_{lpc}(s) = \frac{\omega_{lp,c}}{s + \omega_{lp,c}}. \tag{6.71}$$

The transfer function for the closed loop control $G_{cl,c}(s)$, from the reference current $i_{F,ref}$ to the actual filter current i_F is given by

$$G_{cl,c}(s) = \frac{(s + \omega_{lp,c})(K_{p,c}/L_F)}{s^2 + s(\omega_{lp,c} + \frac{R_F}{L_F}) + \frac{\omega_{lp,c}}{L_F}(K_{p,c} + R_F)}. \tag{6.72}$$

For the transfer function $G_{cl,c}$, the characteristic polynomial $p(s)$ is given as

$$p(s) = s^2 + s(\omega_{lp,c} + \frac{R_F}{L_F}) + \frac{\omega_{lp,c}}{L_F}(K_{p,c} + R_F). \tag{6.73}$$

Assuming a bandwidth of $\omega_{n,c}$ and a damping of ζ, the characteristic polynomial can be expressed as

$$p(s) = s^2 + s2\omega_{n,c}\zeta + \omega_{n,c}^2. \tag{6.74}$$

Identifying the coefficients gives an expression for the control parameter $K_{p,c}$ depending on the chosen damping ζ, the control parameters are given by

$$\omega_{lp,c} = 2\omega_{n,c}\zeta - \frac{R_F}{L_F} \tag{6.75}$$

and

$$K_{p,c} = \frac{\omega_{n,c}^2 L_F}{\omega_{lp,c}} - R_F. \tag{6.76}$$

Assuming $\zeta = 1/\sqrt{2}$ and $\omega_{n,c}$ = 500 rad/s (the same bandwidth as for the current control for the full scale converter), the control variables are given by

$$\omega_{lp,c} = 2\omega_{n,c}\zeta - \frac{R_F}{L_F} = \frac{2 \cdot 500}{\sqrt{2}} - \frac{0.05}{0.02} = 705 rad/s, \tag{6.77}$$

and

$$K_{p,c} = \frac{\omega_{n,c}^2 L_F}{\omega_{lp,c}} - R_F = \frac{500^2 \cdot 0.02}{705} - 0.05 = 7.04. \tag{6.78}$$

As seen in Fig. 6.35 the transfer function $G_{conv,c}(s)$ models the dynamics of the converter from the reference signal of the applied voltage to the real voltage for the output of the converter. Assuming both an ideal converter and a converter that can be approximated by a time delay of 1 ms, the resulting step response for the current control can be seen in Fig. 6.36.

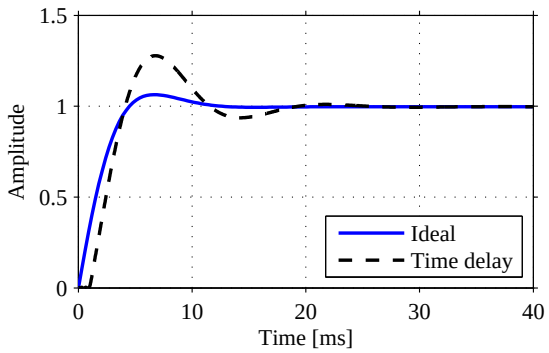

Fig. 6.36 Step response for the current controller for the experimental converter.

Continuing with the voltage controller, the voltage across the capacitance C can be expressed as

$$C\frac{dV_{load}}{dt} = i_{cap} = i_F - i_{load}, \tag{6.79}$$

which gives the transfer function

$$V_{load} = \frac{i_{cap}}{sC}. \tag{6.80}$$

The closed loop controller for the voltage is seen in Fig. 6.37.

In the same way as for the current controller, the low pass filter $G_{lpv}(s)$ has the transfer function

$$G_{lpv}(s) = \frac{\omega_{lp,v}}{s + \omega_{lp,v}}. \tag{6.81}$$

The transfer function for the closed loop control $G_{cl,v}(s)$, from the reference voltage $V_{load,ref}$ to the actual load voltage V_{load} is given by

$$G_{cl,v}(s) = \frac{(s + \omega_{lp,v})(K_{p,v}/C)}{s^2 + s\omega_{lp,v} + \frac{\omega_{lp,v}K_{p,v}}{C}} \tag{6.82}$$

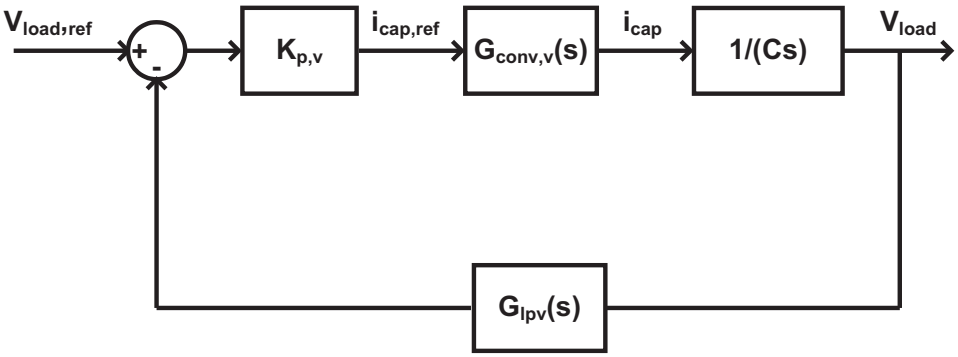

Fig. 6.37 Closed loop control system for control of the load voltage V_{load}.

For the transfer function $G_{cl,v}$, the characteristic polynomial $p(s)$ is given as

$$p(s) = s^2 + s\omega_{lp,v} + \frac{\omega_{lp,v} K_{p,v}}{C}. \tag{6.83}$$

Assuming a bandwidth of $\omega_{n,v}$ and a damping of ζ, the characteristic polynomial can be expressed as

$$p(s) = s^2 + s2\omega_{n,v}\zeta + \omega_{n,v}^2. \tag{6.84}$$

Identifying the coefficients gives an expression for the control parameter $K_{p,v}$ and the bandwidth of the low pass filter $\omega_{lp,v}$ depending on the chosen damping ζ, and the bandwidth $\omega_{n,v}$ of the closed loop controller, the control parameters are given by

$$\omega_{lp,v} = 2\omega_{n,v}\zeta, \tag{6.85}$$

$$K_{p,v} = \frac{\omega_{n,v} C}{\omega_{lp,v}}. \tag{6.86}$$

Choosing the damping $\zeta = 1/\sqrt{2}$ and the bandwidth $\omega_{lp,v}$ = 200 rad/s, the resulting control parameters are

$$\omega_{lp,v} = 2\omega_{n,v}\zeta = 2 \cdot 200/\sqrt{2} = 283 rad/s, \tag{6.87}$$

$$K_{p,v} = \frac{\omega_{n,v} C}{\omega_{lp,v}} = \frac{200 \cdot 3.3 \cdot 10^{-3}}{283} = 0.47. \tag{6.88}$$

The resulting step response is shown in Fig. 6.38, assuming both an ideal transfer function for the converter $G_{conv,v}$ and that $G_{conv,v}$ is a low pass filter with the same bandwidth as the current controller $\omega_{n,c}$ = 500 rad/s.

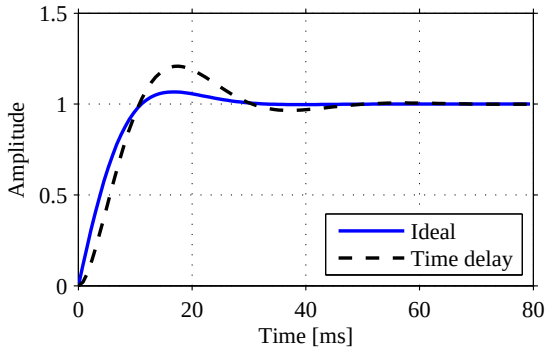

Fig. 6.38 Step response for the voltage controller for the experimental converter.

The closed loop voltage control for the converter is implemented both in PSCAD/EMTDC, using a similar model as for the full-scale converter, and for the experimental setup. The resulting voltage and current waveforms in the case of a step in the reference voltage from 30 V to 70 V are seen in Figs. 6.39 and 6.40. Here, it can be seen that there is a good agreement between the simulated model and the experimental converter.

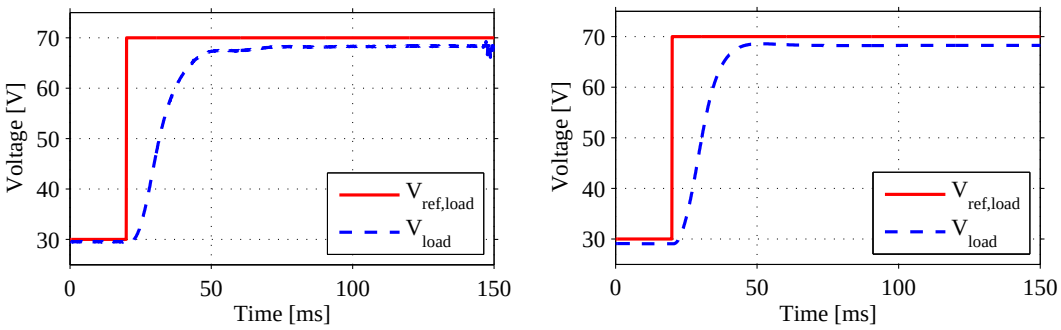

(a) Measured voltages.

(b) Simulated voltages.

Fig. 6.39 Simulated and measured load voltage at a step in the reference voltage.

Comparing the measured and simulated waveforms is made in Fig. 6.41.

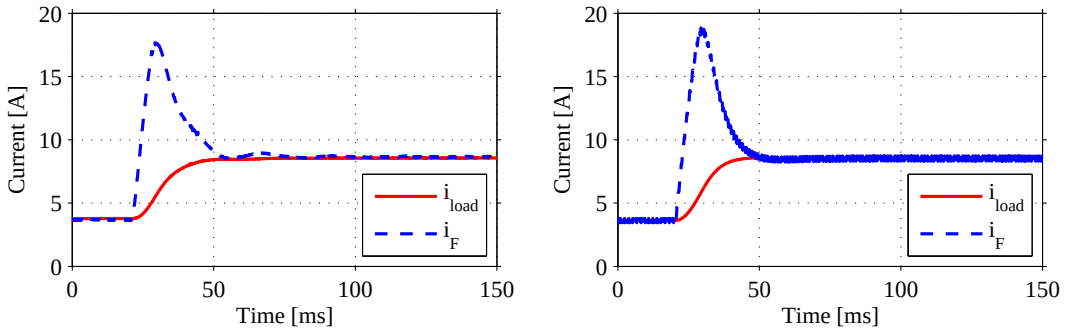

(a) Measured currents. (b) Simulated currents.

Fig. 6.40 Simulated and measured load current and filter current at a step in the reference voltage.

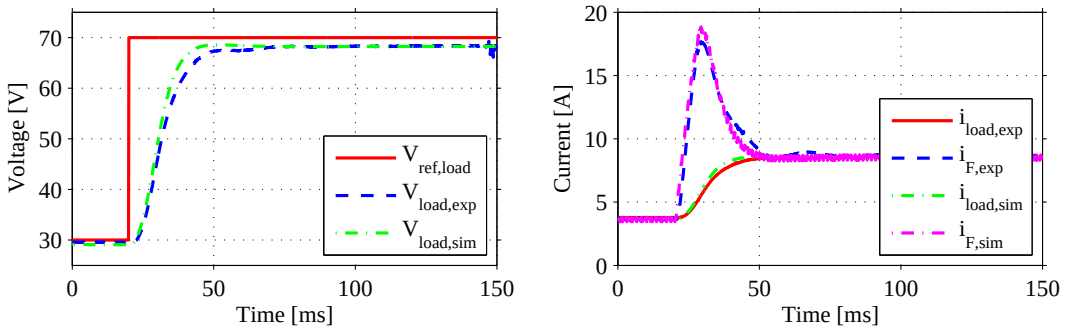

(a) Load voltages. (b) Load currents and filter currents.

Fig. 6.41 Comparison of simulated and measured voltages and currents at a step in the reference voltage.

6.5 Startup of the Wind Farm

For the startup of the wind farm with an internal DC grid, the startup of the turbine must be considered as well as the startup of the whole wind farm and energizing the internal grid. One important issue for the start of the system using an internal DC grid is if the DC/DC converters are unidirectional or bidirectional. Here, the DC/DC converters are unidirectional and consequently power can just be transferred from the turbines to the HVDC connection and not the other way. Therefore, the DC link in the turbine must be energized from the generator and the internal DC bus in the wind farm must be energized from the turbines. For starting the wind turbines, some additional energy source is needed to change the pitch angle for the blades and magnetize the generator. This can either be an energy storage in the turbine, or an auxiliary power supply from the HVDC cable since the grid side HVDC converter is bidirectional. The rated DC link voltage in the turbine is 1.5 kV during normal operation, but during startup it is favorable if the DC-link voltage

can be lower since the auxiliary voltage source then can have a lower voltage. Here, an auxiliary 500 V power supply is assumed with enough energy to change the pitch angle as well as to magnetize the generator. When simulating start of a turbine and the whole wind farm, the switching model in PSCAD/EMTDC must be used since the simple models do not consider the limitations of the DC/DC converters.

6.5.1 Startup of a Turbine

The first case that is considered is the startup of a single turbine. Then, the wind farm is already in operation and the turbine should connect to the DC bus that has its nominal voltage.

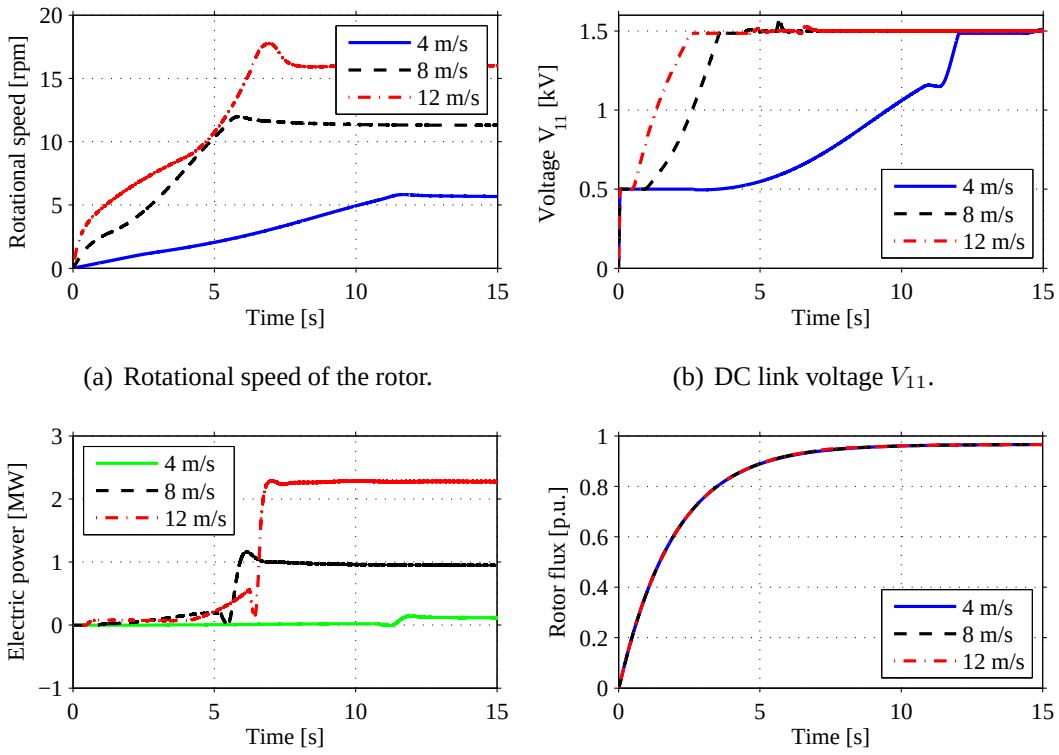

(a) Rotational speed of the rotor.

(b) DC link voltage V_{11}.

(c) Electrical power from the generator.

(d) Rotor flux.

Fig. 6.42 Rotational speed, voltage, power and rotor flux during the startup of a single turbine.

For the startup of a single turbine, the waveforms are plotted in Figs. 6.42-6.44. When the turbine is started, the rotor is unlocked and the wind gives a torque that is accelerating the rotor. The pitch angle is then decreased as seen in Fig. 6.43 (a) when the turbine accelerates to give as high torque as possible according to the C_p curve as described in Section 5.3.1. During the same time as the turbine accelerates, the flux is built up in the

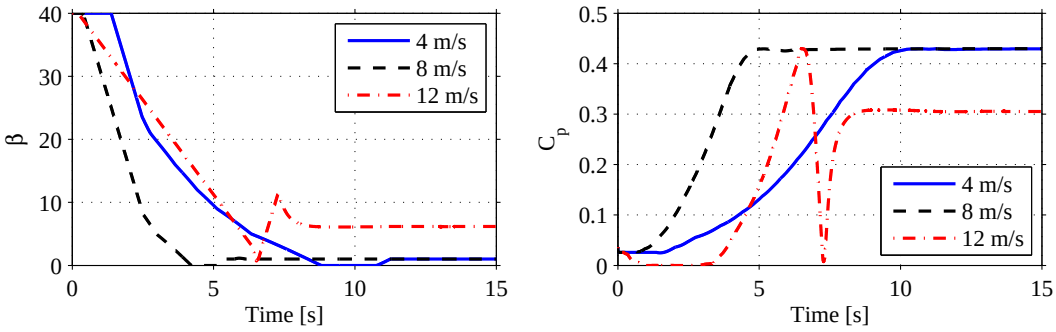

(a) Pitch angle β. (b) Power coefficient C_p.

Fig. 6.43 Pitch angle and power coefficient during the startup of a single turbine.

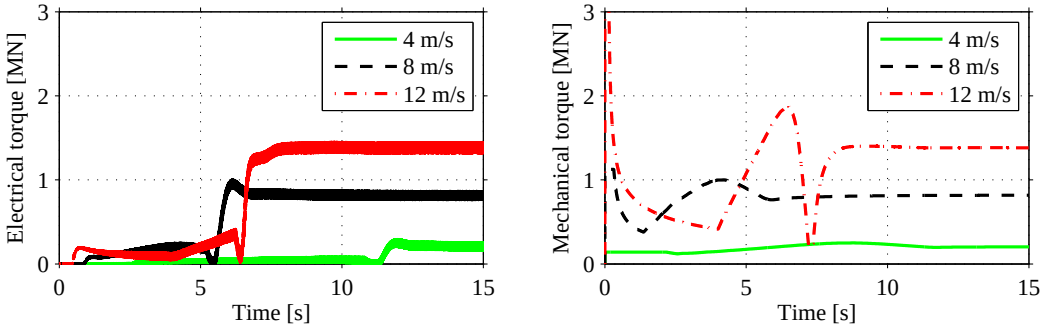

(a) Electrical torque. (b) Mechanical torque.

Fig. 6.44 Torque during the startup of a single turbine.

turbine as seen in Fig. 6.42 (d). It can be seen in Fig. 6.42 (a) that the time for the turbine to accelerate to the rated speed depends on the wind speed. For high wind speeds there is more energy available in the wind and the rotor will accelerate faster. The time for the rotor to accelerate depends on the mechanical properties of the wind turbine. It should also be noted that for high wind speeds (here 12 m/s), the pitch angle β is decreased with a limited rate to give a smooth startup.

During the acceleration of the turbine, the electrical output power is low and is first of all used to increase the voltage for the DC link in the wind turbine as shown in Fig. 6.42 (b). When the DC link voltage has reached the rated value, the DC/DC converter is turned on in order to control the DC link voltage as described in Section 6.3.1. When the speed has increased to the rated speed, the turbine should be kept at that speed by braking the turbine with the electrical torque. The torque control of the turbine described in Section 6.2.1 is then used. It is shown in Fig. 6.44 (a) that the electrical torque is increased at this point and eventually stays at the same level as the mechanical torque shown in Fig. 6.44 (b) to

keep the rotational speed constant. It should be noted that for the wind speed 12 m/s the available electrical torque is not enough to brake the mechanical torque using the pitch angle that gives the highest mechanical torque. Therefore, the pitch angle has to be increased both to stop the acceleration and also to keep the speed at steady state operation as seen in Fig. 6.43 (a), resulting in a lower power coefficient as shown in Fig. 6.43 (b). This is also the reason for the overshoot in the speed shown in Fig. 6.42 (a) for 12 m/s. For the cases with lower power, the electrical torque is increased to brake the turbine, while the pitch angle has to be used for wind speed 12 m/s. The control of the pitch angle is slower and is not started until the speed has increased above the rated speed, resulting in the overshoot in the rotational speed.

6.5.2 Startup of the Wind Farm

During the startup of the whole wind farm, the internal DC bus and the input capacitor to the main DC/DC converter must be energized. As mentioned earlier, the DC/DC converters have unidirectional power flow and the DC link must therefore be energized from the turbines. As seen in the design of the wind farm, the main capacitances for the DC link are the input capacitor for the main converter as well as the output capacitors for the converters in the wind turbines.

When starting the wind farm, either just a few turbines can start and energize the internal DC bus and the input capacitor of the main converter, or a larger number of turbines can start at the same time. Here, both options will be considered. First the case where just a few wind turbines are started, where the number of turbines are depending on the wind speed, and then the case when all wind turbines in the grid are started almost simultaneously. However, when starting just a few turbines, the limitation for the number of turbines is that the power in the wind farm should be enough to make the main converter work properly. To obtain continuous conduction for the main converter, 24 turbines at wind speed 4 m/s are used. The resulting power at this operating point is then 2.6 % of the rated power of the converter (when all turbines are operating at the rated power). Having a lower power level, the control of the converter will not have the same performance and the losses will be high compared to the transferred power. The needed number of turbines operating at start of the wind farm will be 24 for wind speed 4 m/s, 3 for 8 m/s and 2 for 12 m/s. In Fig. 6.45, the waveforms during startup is shown for all three cases. For the cases with 2 and 3 turbines, it is assumed that these turbines are in different radials. The turbine for which the waveforms are shown in Fig. 6.45 is the last turbine in a radial with 10 turbines. For the case with wind speed 4 m/s, the waveforms are shown for the same turbine and it is assumed that 4 additional turbines are started in that radial.

At the start of the wind farm, each turbine will be started in the way described for the

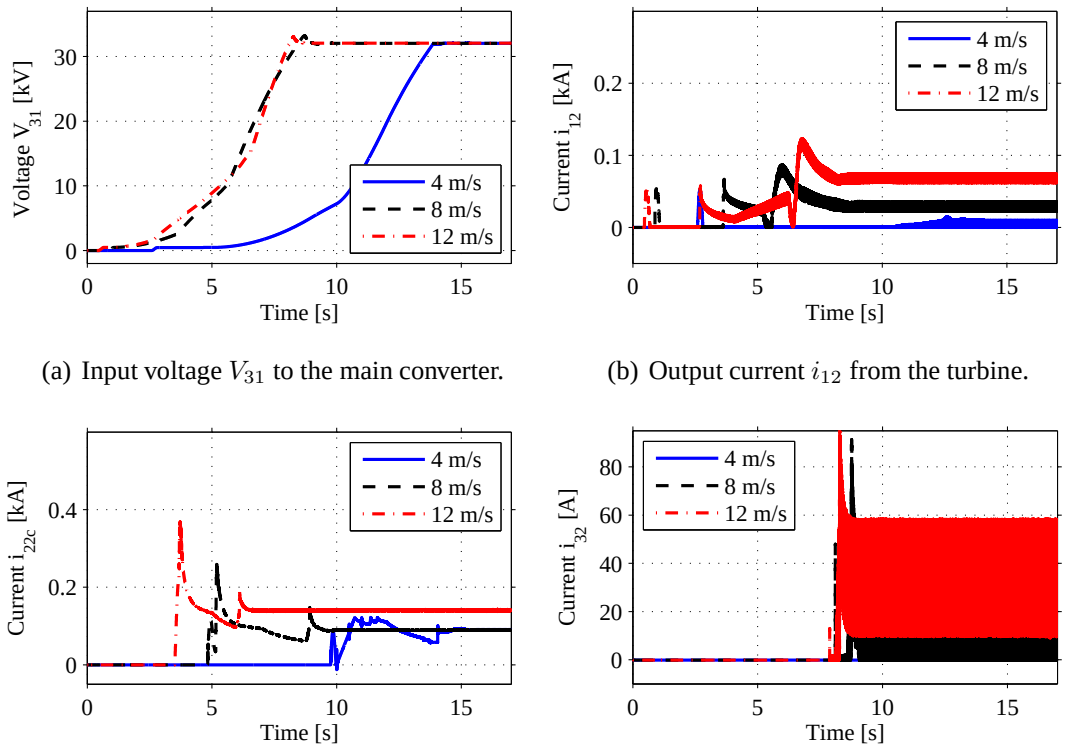

(a) Input voltage V_{31} to the main converter.

(b) Output current i_{12} from the turbine.

(c) Input current i_{22c} to the main converter.

(d) Output current i_{32} from the main converter.

Fig. 6.45 Waveforms for startup of a wind farm at 12 m/s, 8 m/s and 4 m/s using 2, 3 and 24 turbines respectively.

startup of a single turbine by releasing the rotor and pitching the blades to accelerate the turbine. During the acceleration of the turbine, the DC link voltage V_{11} in the turbine is increased as shown for the startup of a turbine. At the same time, the DC/DC converter in the wind turbine is turned on and also the DC bus is charged as seen in Fig. 6.45 (a). When the rated voltage is reached for the DC bus, the main DC/DC converter is turned on and the excess power is fed to the HVDC connection as seen in Fig. 6.45 (d).

Another option for the turn on of the wind farm is to start all turbines more or less simultaneously as shown in Fig. 6.46. Here, the results are shown when all turbines are started evenly distributed within 2 seconds.

As seen in the figure, the start of the wind farms works in the same way as for the case with a lower number of turbines shown in Fig. 6.45. The difference between the cases is the higher total current for the main converter in Figs. 6.46 (c) and (d). Also, the DC link voltage shown in Fig. 6.46 (a) increases faster due to the larger number of turbines.

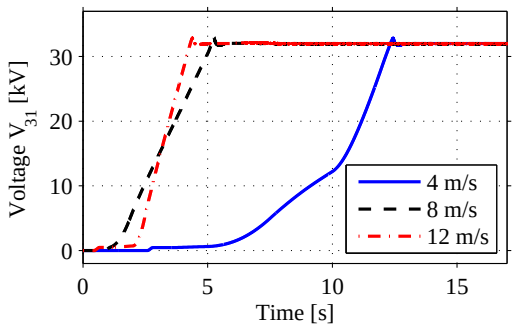

(a) Input voltage V_{31} to the main converter.

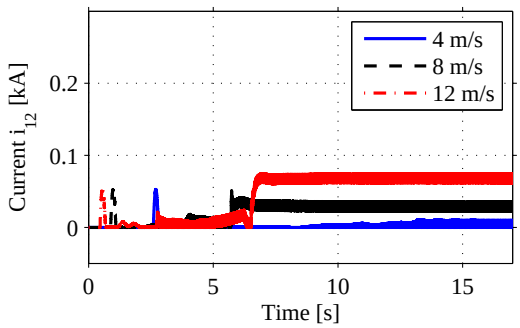

(b) Output current i_{12} from the turbine.

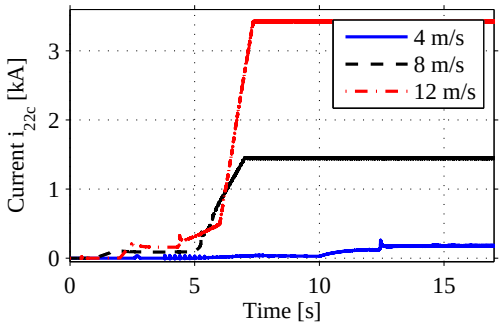

(c) Input current i_{22c} to the main converter.

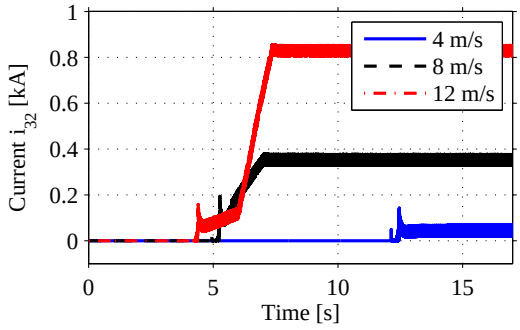

(d) Output current i_{32} from the main converter.

Fig. 6.46 Waveforms for startup of a wind farm at 12 m/s, 8 m/s and 4 m/s using all turbines.

6.6 Summary

In this chapter, the control of the wind farm has been investigated. For the wind turbines, the control method was obtained and it was shown that the reference speed and power could be followed closely. For the control of DC/DC converters, the design was based on the assumptions of no communication and no limitations for the power variations. Given the maximum voltage variations of 5 % and the switching frequency 1 kHz, the needed DC link capacitance for stable operation is 16 mF for the DC collection bus and 152 mF for the DC link in the turbine. This corresponds to an energy storage of 74 ms of transferred rated power. The control method for the DC/DC converters was verified using a down scaled experimental setup. Also, it was shown that the wind farm can be started using auxiliary power sources of 500 V in the turbines.

Chapter 7

Evaluation of Fault Condition Handling

7.1 Introduction

In the previous chapters, the wind farm with a DC collection grid has been designed, a dynamic model has been obtained and the control of the system has been determined during normal operating conditions. However, also the fault handling of the wind farm must be considered including the required protection devices.

Due to the increase of the wind power penetration, the requirements on the operational behavior of wind farms from the main grid side has during the last years been reinforced. The wind farm should be able to stay connected during shorter grid faults (the fault ride through properties) [7], and it is also an aim that the consequences for the main grid due to internal faults should be minimized. Further, it is desirable that the wind farm can support the main grid [7]. Compared to a wind farm with an AC connection, the HVDC connection allows asynchronous operation of the internal wind turbine grid, eliminating the propagation of some faults between the grids [8].

In this chapter, the fault ride through properties for the wind farm with an internal DC grid are studied as well as the handling of internal faults in the wind farm. For the operation during faulted conditions, the time constants for the occurrence of the fault, the detection and the clearing of the fault are very short from a general wind turbine operation point of view. Therefore, a simplified model of the wind turbine can be used since the operating conditions for the wind turbine can be assumed to be constant during the fault.

7.2 Fault Ride Through Operation during External Faults

Even though an HVDC connection for a wind farm or a full power converter for a wind turbine decouples the generators from the grid, the ride through properties are still im-

portant [8, 61]. When a fault in the external grid occurs, the power transmitted from the HVDC connection is lowered and in the worst case stopped [61]. Consequently, the power produced in the wind turbines must be dissipated somewhere. Since the requirement from the grid is that the wind farm should not disconnect during the fault, the wind turbines can not be shut down since there is a significant time delay when the turbines are to be turned on again.

The fault ride through properties of a wind farm with an internal AC grid connected by a VSC HVDC connection have been studied in [6, 7, 62]. For a drastically reduced power transmission capability to the main grid for a VSC HVDC connected to a wind farm, there are two methods to avoid tripping of the wind farm and prevent an over voltage [6]. Either the wind turbines can reduce their output power, or a breaker resistance can be used at the input of the inverting VSC towards the grid. Using a breaker resistance at the HVDC link is the most robust solution and the wind farm will continue to operate at normal operation during grid faults. Since the DC collection grid will not be affected using this option, it will not be investigated here. Instead, the option of dissipating the power in the turbines will be investigated further. Using this solution, the first step is to detect the fault, which can be done by detecting an over voltage at the HVDC connection. Then, the power flow in the wind farm has to be stopped which, depending on the capacitance for the converters, has to be done within 5 to 10 ms [6]. Normally, the protection level for a fault is set to 30 % over voltage [6]. When the fault has been detected, there are several different ways to reduce the output power. One solution is to use a breaker resistance to dissipate the power in the wind turbine [61, 63, 64]. Another possibility is to stop the power transfer from the turbine and let the excess energy be stored as rotational energy. In this case, the voltage control for the DC link in the turbine is done by the generator side converter instead of the grid side converter in the wind turbine [61]. Over speed is then prevented by pitching the blades.

The focus in this study will be on the behavior of the internal DC grid during a grid fault, including both DC/DC converters and the HVDC connection. Also, the detection and clearing of the fault will be investigated as well as the reconnection of the wind farm. In the occasion of a grid fault, the disconnection and the reconnection are assumed to be the same and not depending on the length of the fault, and are therefore treated as two different occasions. The length of the fault determines the dimensioning of the breaker resistance. If the fault is longer than the required time for fault ride through, the turbines are shut down. Here, the case where the output power is completely stopped is investigated to show the performance and the limitations of the DC system. However, if the power flow is just limited and not stopped, the control of the voltage at the DC bus is instead achieved by the wind turbine DC/DC converters while the main DC/DC converter towards the HVDC link is controlling its output power depending on the output power towards the main grid.

7.2.1 Fault Detection for the HVDC Link

When the fault occurs in the connecting main grid, the gride side VSC for the HVDC link shown in Fig. 7.1 detects the grid fault and reduces the power to the grid. Here, the worst case is considered where the wind turbines are running at full power and the power delivery to the grid is stopped completely. The resulting voltage for the HVDC connection will then depend on the capacitance for the HVDC link and also the time delay until the fault is detected by the main converter and the power to the HVDC link is stopped.

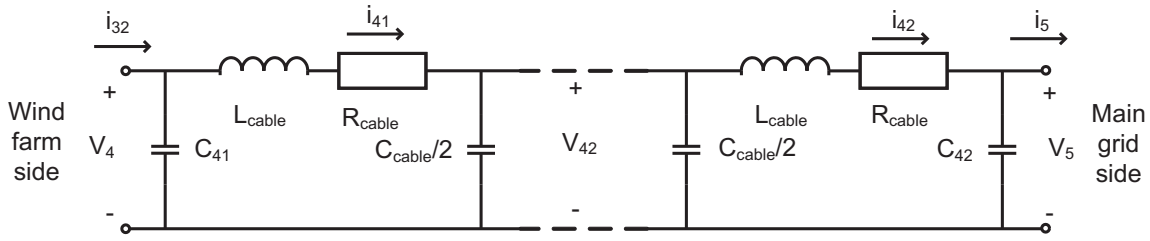

Fig. 7.1 The equivalent circuit of the HVDC link.

The detection of the fault can be done either by communication between the gride side VSC and the main DC/DC converter connected to the wind farm or by measuring the voltage level at the main converter. If the voltage V_4 at the main converter should be measured, it should be noted that the voltage along the cable is different due to the cable parameters and depends on the length of the cable. Assuming that the over voltage is detected at the output of the main converter when the output voltage is increased 10 % from the reference value, the resulting voltage waveforms along the cable can be seen in Fig. 7.2 for different values of the total HVDC link capacitance (C_{41} + C_{42}), and the current waveforms can be seen in Fig. 7.3. In this case, the length of the HVDC link is 40 km and the model of the HVDC connection consists of 8 connected π-models of 5 km each.

Normally, the DC link capacitance in an HVDC connection has a stored energy of 2 ms transferred power [65]. In this case, the resulting capacitance will be 26 μF distributed to two capacitors, one in each end of the cable. It can be seen that if the requirement for the HVDC link is that the main converter in the wind farm should be able to detect the fault at 10 % (143 kV) over voltage and then stop the power flow without having an over voltage of more then 30 % (169 kV) at the grid side VSC, the required DC link capacitance is 50 μF. However, to have some safety margin and allow a possible delay in the detection of the over voltage, a suitable value for the DC link capacitor is 100 μF, distributed with 50 μF in each end of the HVDC link. It should also be noted that in the case of a longer cable, the delay between the rise of the voltage at the grid side converter and the detection of the over voltage at the main converter would be longer and the required DC link capacitance will be increased.

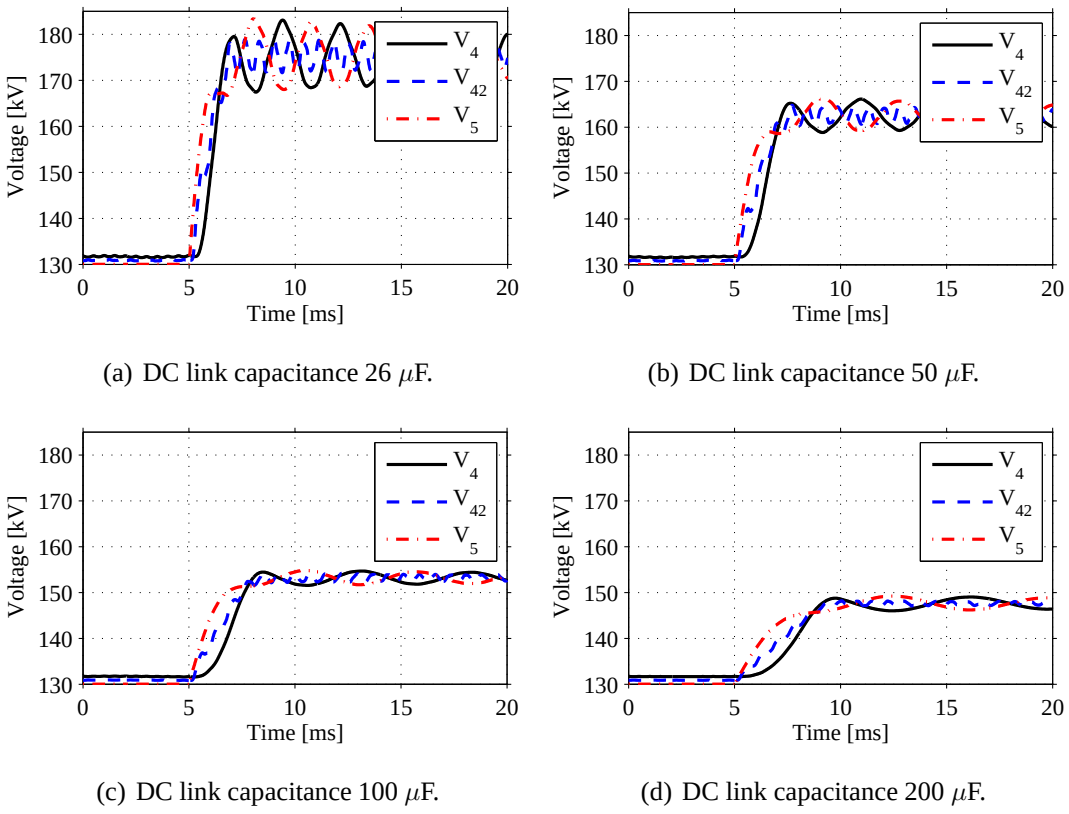

(a) DC link capacitance 26 μF.

(b) DC link capacitance 50 μF.

(c) DC link capacitance 100 μF.

(d) DC link capacitance 200 μF.

Fig. 7.2 Voltage at the HVDC link at a fault in the main grid for different DC link capacitances.

From Fig. 7.3, it can be seen that from the point when the power flow is stopped in the IGBTs of the DC/DC converter connected to the wind farm, there is a certain time before the current i_{32} in the inductance L_3 has decreased to zero. The reason for this is the time to reduce the current in the inductance from the value at full load to zero. Having the voltage V_n = 130 kV and the current I_n = 850 A at normal operation, the time Δt_L required for the decrease of the current can be calculated as

$$\Delta t_L = \frac{L_3}{V_n} I_n = \frac{0.3}{130 \cdot 10^3} 850 \approx 2ms. \tag{7.1}$$

This energy limits the minimum value of the capacitance for the HVDC link. Even if the main converter in the wind farm is turned off instantaneously when the fault has been detected by the grid side converter, there is a certain capacitance needed for limiting the over voltage.

Using telecommunication between the grid side converter and the main converter, there is also a delay between the detection of the fault by the grid side converter and the main

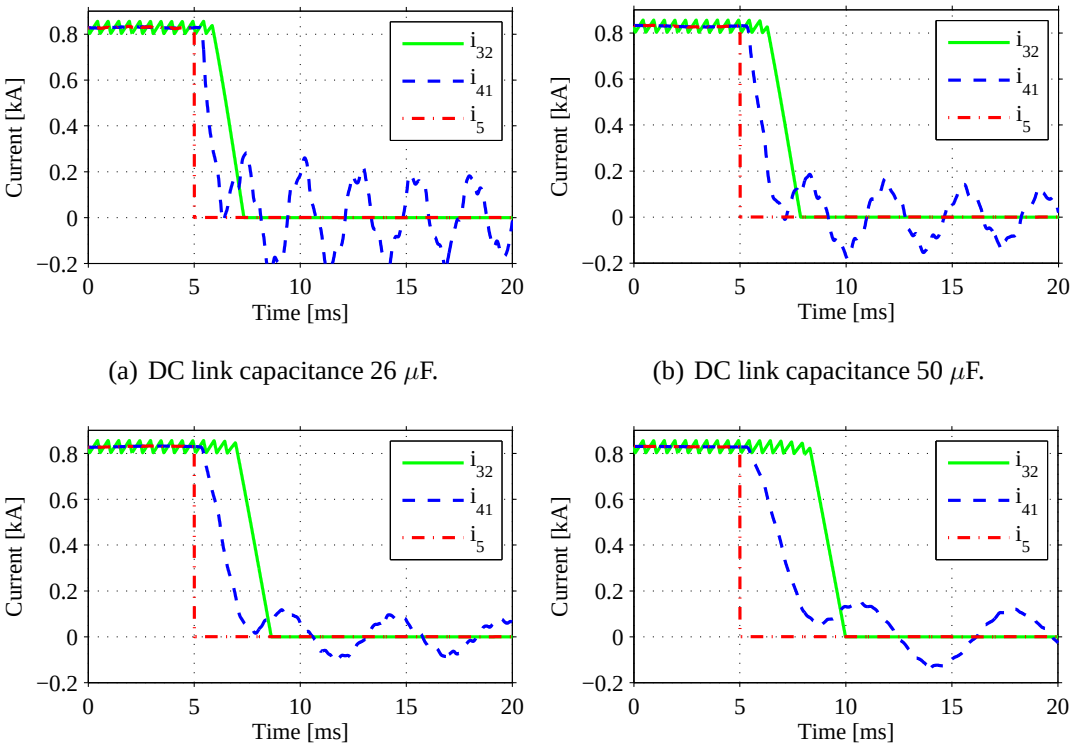

(a) DC link capacitance 26 μF.

(b) DC link capacitance 50 μF.

(c) DC link capacitance 100 μF.

(d) DC link capacitance 200 μF.

Fig. 7.3 Current in the HVDC link at a fault in the main grid for different DC link capacitances.

converter. However, this delay is not as dependent on the length of the HVDC link. Knowing the delay in the communication, the required DC link capacitance can be calculated. It should also be noted that there are oscillations in the over voltage and having a steady-state over voltage of 20 % will give larger peak voltages due to oscillations, especially at low value of the DC link capacitance. Here the required capacitance is calculated based on a steady-state over voltage of 10 %, 20 % and 30 %. During the delay time Δt, the energy ΔW is accumulated in the DC link capacitance. This accumulated energy is calculated using the power flow P_{WF} from the wind farm as

$$\Delta W = P_{WF}\Delta t. \tag{7.2}$$

The energy stored in the capacitances before the fault W_n is calculated using the voltage V_n at the HVDC link at normal operation as

$$W_n = \frac{1}{2}CV_n^2. \tag{7.3}$$

It should also be noted that there is some energy stored in the output inductance L_3 of the

main converter. This energy W_L can be expressed as

$$W_L = \frac{1}{2} L_3 I_n^2. \tag{7.4}$$

The energy stored in the capacitors after the fault W_{tot} is then the sum of the energy W_n before the fault, the energy ΔW accumulated during the fault and the energy W_L stored in the inductance. The total energy can be expressed as a function of the total voltage after the fault V_{tot} as

$$W_{tot} = \Delta W + W_n + W_L = \frac{1}{2} C V_{tot}^2. \tag{7.5}$$

Inserting the expressions for ΔW, W_n and W_L and eliminating the capacitance C gives

$$C = \frac{L_3 I_n^2 + 2 P_{WF} \Delta t}{V_{tot}^2 - V_n^2}. \tag{7.6}$$

Assuming that the wind farm is operating at full power, P_{WF} = 110 MW, V_n = 130 kV and I_n = 850 A. Further, for the possible increase in the voltage of 10 %, 20 % and 30 %, the required value of the DC link capacitance as a function of the time delay can be seen in Fig. 7.4.

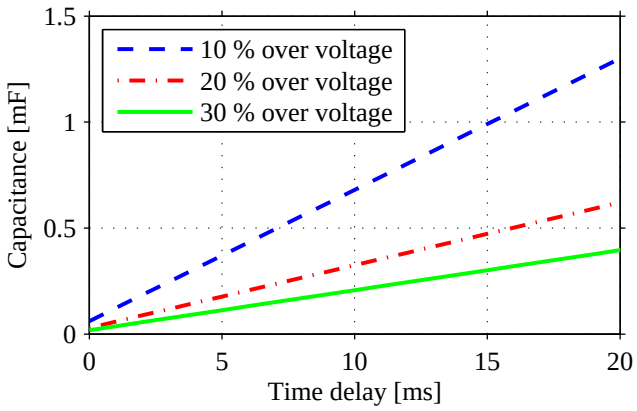

Fig. 7.4 Required DC link capacitance for the HVDC link as a function of the time delay in the communication at a grid fault.

As seen in the figure, the needed capacitance is increased with the time delay for the communication. Assuming that the time delay for the telecommunication is at least 5 ms, the required DC link capacitance is 372 μF, 177 μF and 110 μF respectively for the over voltages 10 %, 20 % and 30 %. Without communication, the required capacitance is 100 μF

so there is no benefit having a telecommunication between the terminals. In the case of a faster communication, the required capacitance can be decreased. Also, in the case of a very long cable, telecommunication between the terminals might give a faster detection of the voltage. In that case, the required capacitance for the DC link is depending on the time delay as shown in Fig.7.4.

Further, there are other solutions for fault ride through than those stated above. In [6], it is stated that a small breaking resistor can improve the performance during grid faults. Using a small breaking resistor, some of the excess power can be dissipated at the inverter end of the HVDC link and the required capacitance can then be reduced.

7.2.2 Fault Handling for the Internal DC bus

The first step when the power flow to the HVDC link should be stopped in the case of a grid fault is to stop the power in the DC/DC converter connecting the wind farm and the HVDC link, as described in the previous section. After the main DC/DC converter has been turned off, the voltage at the internal DC bus is increasing, since power is still delivered from the turbines. In the same way as for the main converter, the power from the turbines can be turned off either when an over voltage is detected at the connection to the DC bus or when a fault signal is received from the main converter. For the DC bus, the value of the capacitance is given by the control of the voltage level as shown in Section 6.3.2 and is in total 16 mF.

In a similar way as for the HVDC link, there is a connection between the over voltage and the time delay for turn off of the power from the turbines. Assuming a steady state voltage V_n, the total over voltage V_{tot}, the total output power P_{WF} from the turbines and the capacitance C, the allowed time delay Δt can be calculated as

$$\Delta t = \frac{C(V_{tot}^2 - V_n^2)}{2P_{WF}}. \tag{7.7}$$

For the output power P_{WF} = 110 MW and the voltage V_n = 32 kV, the resulting time delays are 15.6 ms, 32.8 ms and 51.4 ms respectively for the allowed over voltages 10 %, 20 % and 30 %. Just as for the main converter, there is a finite time Δt_L for the output current in the wind turbine converter to decrease to zero, which is calculated as

$$\Delta t_L = \frac{L_1}{V_n} I_n = \frac{0.3}{32 \cdot 10^3} 72 \approx 0.7ms. \tag{7.8}$$

Here, it can be seen that the time for the current to reach zero is considerably shorter than the allowed delay time, and there should not be any difficulties to stop the power flow

within the allowed time to limit the power level. Here, it is assumed that each turbine stops the output power in the DC/DC converter when an over voltage of 10 % (35.2 kV) is detected. In Fig. 7.5, the voltages and currents for the turbines in a radial are shown.

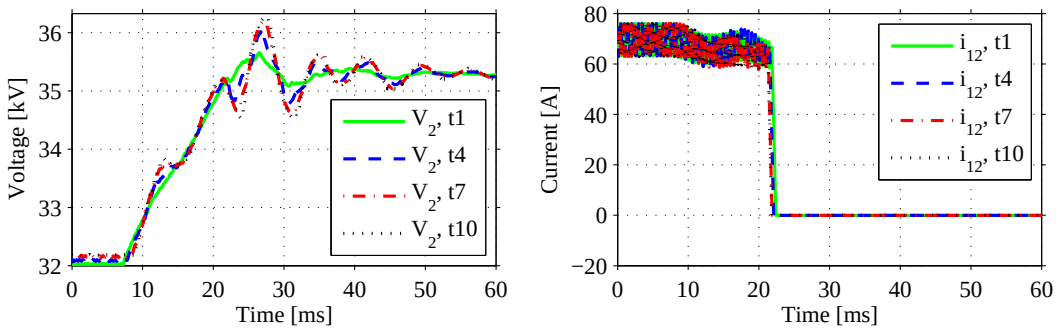

(a) Voltages at the connection to the turbines.

(b) Currents from the turbines.

Fig. 7.5 Voltage and current for the turbines during a grid fault.

Here, it can be seen that the increase in the voltage level is relatively slow and the peak over voltage is just slightly above 35.2 kV at which the over voltage is detected.

7.2.3 Reconnection of the Wind Farm

When the fault is cleared, the inverter towards the grid can start to transmit power again and should resume the output power before the fault as fast as possible. The first step in the reconnection is for the main DC/DC converter in the wind farm to detect the clearing of the fault and start transferring power, and then also the wind turbine DC/DC converters need to detect the fault clearing and start the power transfer. In the same way as when the fault is detected, the detection of the clearing of the fault can be made either by measuring the voltage level or by communication between the converters. Assume that there is no communication available, the voltage for the DC link must decrease for the main DC/DC converter in the wind farm to detect the clearing of the fault. In Fig. 7.6, the current at the HVDC link can be seen during the clearing of the fault and in Fig. 7.7, the voltage at the DC bus can be seen.

The fault is cleared at t = 5 ms and the initial current is depending on the control of the grid side VSC. Here, it is assumed that the grid side inverter controls the voltage at the HVDC link and the resulting current in Fig. 7.6 (b) is then the current needed for the reduction of the DC link voltage to the nominal value with a reasonable slope as seen in Fig. 7.7 (b). When the voltage is decreased, there are some oscillations and the over voltage protection for the main converter should be temporarily disabled not to detect a

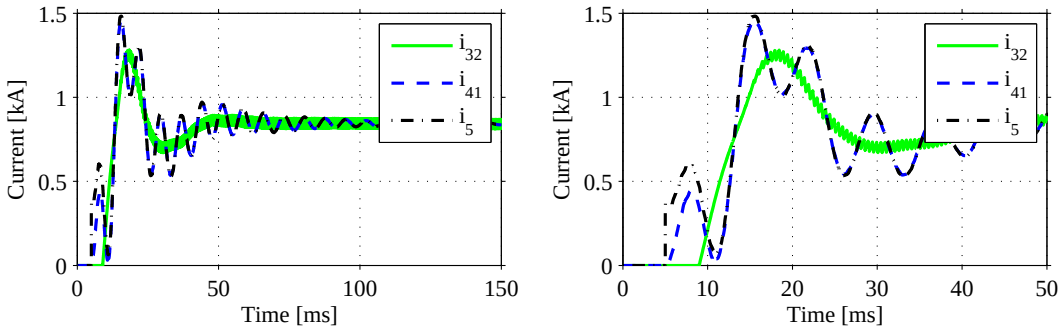

(a) Overview. (b) Zoomed figure.

Fig. 7.6 Current at the HVDC link during the reconnection after a grid fault.

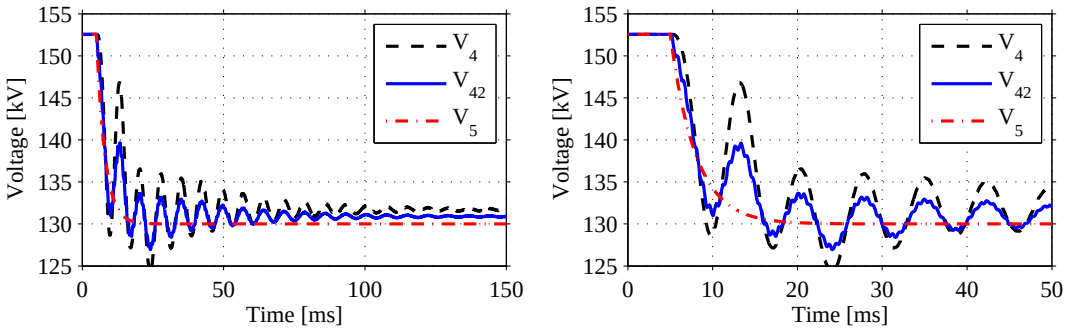

(a) Overview. (b) Zoomed figure.

Fig. 7.7 Voltage at the HVDC link during the reconnection after a grid fault.

new fault at the oscillations following the reconnection.

At t = 9 ms (4 ms after the clearing of the fault) the voltage has reached the value 132 kV at which the fault is detected as cleared by the main converter. Then, the main converter is turned on and the current is increased to the nominal value 850 A within 5 ms after the turn on of the converter (at t = 14 ms). Then, there is an overshoot in the current when the main converter decreases the over voltage at the internal DC bus, and at t = 70 ms, the steady state value is reached.

In [7], it is stated that the German and Irish grid codes allows the power from the wind farm to drop during a grid fault, but the output power must recover to 90 % of the available power within one second. Further, it is stated in [66] that in the English grid codes for offshore generation, the wind farm should recover to 90 % of the pre fault value within 0.5 seconds after the fault has been cleared. Consequently, since the full power is available after 14 ms of the clearing of the fault and the steady state condition has been reached

within 70 ms, the grid code can be followed also when the excess energy is dissipated in the turbines during a grid fault.

Continuing with the reconnection of the internal DC bus, the current from all turbines in a radial can be seen in Fig. 7.8 and the voltage at the turbines in a radial can be seen in Fig. 7.9.

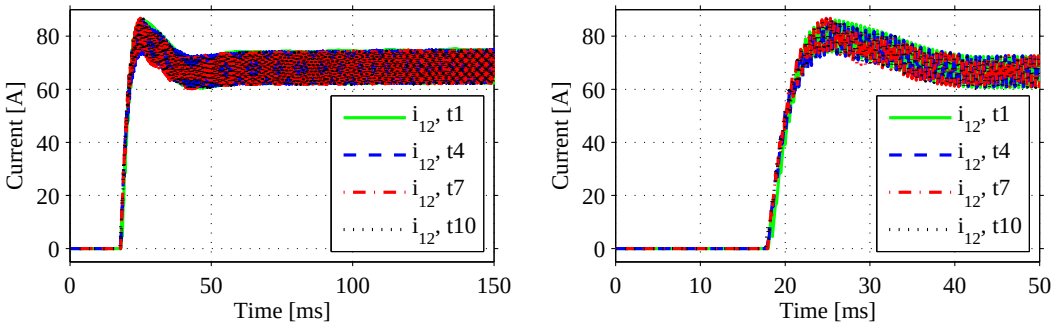

(a) Overview. (b) Zoomed figure.

Fig. 7.8 Current from the turbines in a radial during the reconnection after a grid fault.

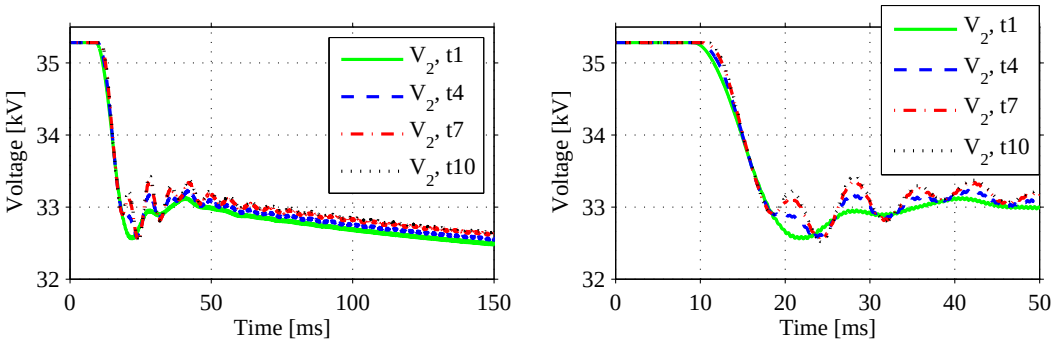

(a) Overview. (b) Zoomed figure.

Fig. 7.9 Voltage at the connection of the turbines to the radial during the reconnection after a grid fault.

When the main converter has been turned on, the voltage for the internal DC bus is decreased as seen in Fig. 7.9 (b). At t = 18 ms (approx. 9 ms after the main converter was turned on), the voltage has decreased to 33 kV and the clearing of the fault is detected by the turbines. Then, the current in the turbines is increased during 4 ms and there is an overshoot before the current reached the steady state value at t = 70 ms. Looking at

the voltage in the radial, there is an overshoot when the turbines are reconnected as seen in Fig. 7.9 (a). Then, due to the integral part of the voltage controller, the voltage will eventually reach the steady state voltage 32 kV.

7.3 Internal Faults in the Wind Farm

For a multi-terminal DC system, fault detection and finding the location of a fault are critical issues. The availability of a wind farm with an internal DC grid can be increased by having a reliable system for detection and localization of faults as well as a flexibility in the possibility of disconnection of the faulted parts.

There are several papers considering fault detection for multi terminal DC systems. Fault detection and clearing of the faults in a multi terminal DC system have been studied in [16, 67]. In [67], both line-to-line faults and line-to-ground faults are investigated. The systems presented in these papers are based on a number of converters connecting several AC loads/sources to a DC bus and there is a possibility to stop the power flow at the AC side of the converters. In [67], the IGBTs are turned off in the case of a line-to-line fault and a large DC current is flowing in the antiparallel diodes before the fault is cleared on the AC side. However, before the converter is turned off, the fault current is measured in order to find the location of the fault. Moreover, in [67, 68] the detection of the fault is investigated as well as the identification of the faulted line and also the reconnection of the non-faulted lines. This investigation is made for a ring bus connecting three converters. The detection of a DC fault is defined in [68] as the simultaneous increase of the current into the DC network and the reduction of DC voltage at the network node. Another issue for a multi terminal DC system is to maintain operation even if a single converter fails as described in [9].

In this system, the wind farm with 48 turbines is considered that was shown in Chapter 4. Here, a fault is assumed to occur in one of the 5 radials. Due to size limitations of the simulations, the radial with the fault is modeled including the DC/DC converter for each wind turbine while the other radials have current sources as models of the wind turbines.

In this section, first the different possible internal faults for the wind farm are listed and the protection devices needed for clearing a fault on the DC bus are discussed. Then, the procedure for disconnection of a faulted part is shown. In the end, the behavior of the wind farm is shown in the case of different internal faults, and the methods for detection of the faults are shown as well as the procedures to determine the locations of the faults.

7.3.1 Possible Fault Conditions in a Wind Farm

In a wind farm with an internal DC grid connected to an HVDC connection, there are several possible faults that must be considered. Examples of these faults are:

- Internal faults in the DC/DC converters.
- Faults in the wind turbines.
- Faults in the HVDC connection.
- Faults in the DC bus.

Starting with the **internal faults in the DC/DC converters**, it is assumed that there is an internal monitoring system for each converter that can detect a fault. The design of the converter is made with redundancy, so a failure of a single semiconductor module will not stop the operation of the converter. If there is a severe fault for a converter, the remaining IGBTs will be blocked and the power transmission will be interrupted. For a fault in the wind turbine converter, the turbine will stop and the DC collection grid will just see a decrease in the input power. In the case of a fault in the main converter, the power flow from the internal DC bus to the HVDC link is stopped and the wind farm will shut down. For the DC/DC converters, it can be assumed that the operation is similar to a VSC used for HVDC transmission and the failure rate should therefore also be similar. In [51], it is stated that for a VSC HVDC pole (excluding the cables) the failure rate is 1-2 outages/year. This can then be assumed to also be the case for the DC/DC converters in the wind farm.

For the **faults in a wind turbine**, it is assumed that there are existing fault detection schemes for the turbines in operation today. When an internal fault is detected, the operation is stopped and the power flow through the wind turbine DC/DC converter will decrease to zero. Consequently, the fault detection of the wind turbine is not investigated further. For a wind turbine, a typical failure rate is less than 0.5 failures/year, but for turbines with high power rating the failure rate can be slightly higher [69].

Also for the **faults for the HVDC link**, the technology is already existing today and it is therefore assumed that there is an available fault detection scheme. In the case of a fault and the following shut down of the HVDC link, the internal DC bus will experience the same conditions as in the case of a grid fault. For the faults in the HVDC link, there is an average of 1-2 outages per year for the VSC HVDC pole excluding the cables [51]. Including the cable, the possibility for a fault is increasing with about 1-2 faults/100 km/year [70].

For the **faults in the internal DC bus**, the fault detection scheme is more difficult since it is a multi terminal DC system. For the operation of the wind farm, it is important to both be able to detect and to find the location of the fault. The faulted part can then be disconnected and the rest of the wind farm can continue operating. The possibility for cable faults can be found in [70] and is in the magnitude of 1 fault/100 km/year. Since the total cable length in the wind farm is about 100 km there will be approximately one failure per year for the internal DC bus.

Summing up the different possible faults in the wind farm grid, the possibility for the different faults are similar, around once a year for each unit. For the faults in a turbine or a DC/DC converter in a wind turbine, the turbine must be shut down and the wind farm can operate as usual with the other turbines, just sensing the loss of the power from a turbine. However, if there is a fault in the main converter or in the HVDC link, the transmission to the main grid must be turned off and the operation of the wind farm stopped in the same way as for a grid fault. In the case of a fault in the internal DC bus, the fault must be located and detected so the faulted part can be disconnected. The operation of the wind farm during faults on the internal DC bus, which is a multi terminal DC system, will be investigated in this section.

7.3.2 Protection Devices for Fault Clearing

The protection devices that can be used for the system are traditional AC breakers on the AC side of the system as well as DC disconnecters and DC circuit breakers. DC disconnecters can not interrupt a fault current, but when the fault is cleared and the system is de-energized, the DC disconnecters can be opened to isolate the DC line [67, 71]. DC circuit breakers can disconnect a fault current on the DC side, but have the disadvantage of a higher cost than the AC circuit breakers [67]. In [71], it is stated that using circuit breakers is economically feasible for DC micro-grids with voltage levels lower than 600 V. Also, breaker resistances are needed for de-energizing the system before isolating the faulted parts with DC disconnecters, and can also be used in the turbines for ride-through operation during grid faults.

For the protection of the DC bus, there are several possibilities to use the above stated devices. In the case of a short circuit fault, the energy fed into the faulted parts of the system needs to be stopped. One possibility is to stop all turbines and to also stop the power transfer in the main converter. In the case of non faulted converters, both the power transfer from the DC/DC converters in the wind turbines can be stopped as well as the power transfer from the main DC/DC converter. When there is no more input power to the system, the DC grid can be de-energized and the faulted parts can be isolated using the DC disconnecters. Consequently, all power transfer from the wind farm will be stopped

and the whole DC bus will be de-energized before the fault can be isolated and the wind farm can be turned on again. Another possibility is to have a DC circuit breaker at the connection to each radial. In the case of a fault, the faulted radial can be detected and disconnected from the main converter while the remaining four radials can continue to operate during the fault. In the faulted radial, the power from the wind turbines will be stopped, the faulted part of the radial will be isolated and the turbines between the main converter and the fault can be reconnected.

Considering the protection devices for the wind farm, there must be a DC disconnecter between each turbine to be able to isolate faulted parts of the system. Also, if continuous operation of the non faulted radials is considered, a DC circuit breaker in each radial is needed that is located at the connection to the main converter. If no DC circuit breakers are used, they are replaced with disconnecters. In Fig. 7.10, the locations of the DC disconnecters and circuit breakers are shown for the DC bus.

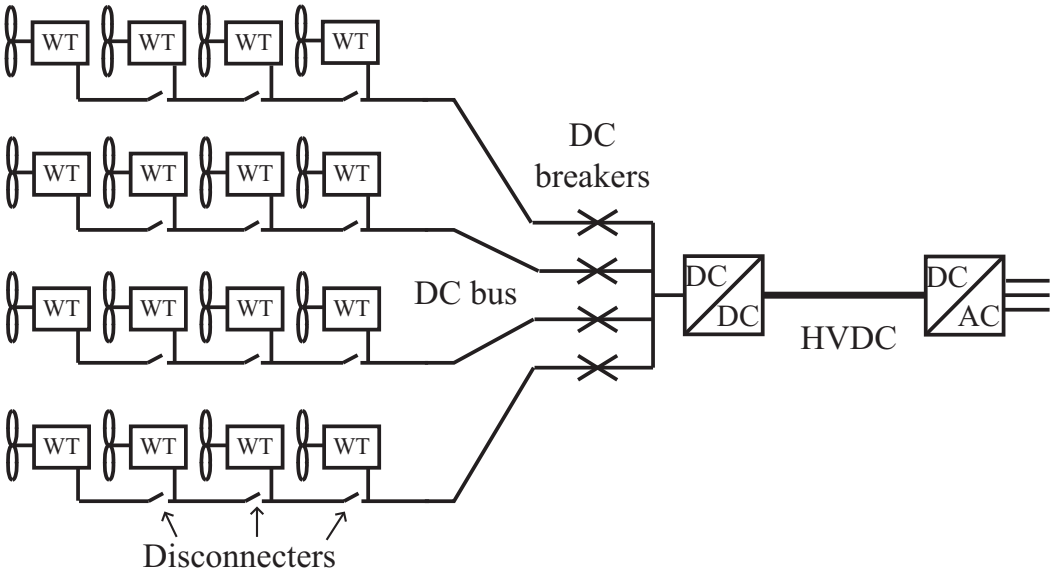

Fig. 7.10 Location of the disconnecters and DC circuit breakers (optional) for the DC bus.

Further, the protection devices for all components in the DC based wind farm is shown in 7.11.

7.3.3 Disconnection of a Faulted Part

When a fault occurs in the system, the fault must be detected and located and the faulted part must then be disconnected from the rest of the system for continued operation. However, since DC circuit breakers are very expensive and therefore not used between all

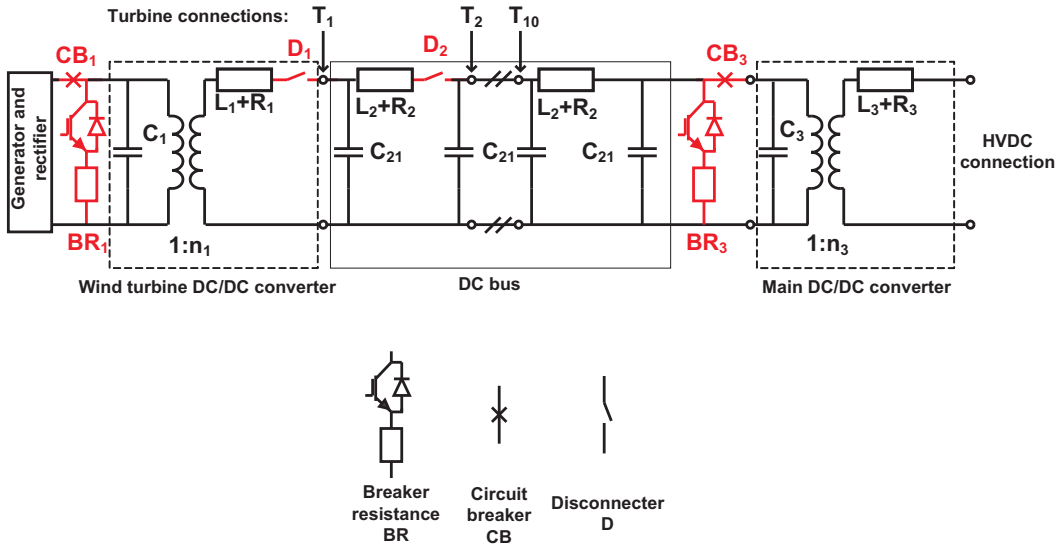

Fig. 7.11 Location of the protection devices for the wind farm.

turbines, the faulted part can not simply be disconnected, instead the system must be discharged before the disconnecters (DC switches) can be opened. The disconnection of a faulted part and the resulting disturbance for the output power depends on if there is a DC circuit breaker for each radial. Here, the detection and location of the fault is discussed as well as the disconnection of a faulted part, with and without DC breakers.

Detect and Find the Location of the Fault

The disconnection of a faulted part is just possible if the fault can be both detected and located. In Sections 7.3.4 and 7.3.5, the detection of the faults will be studied in detail both for line-to-line cable faults and ground faults.

When a fault occurs, it is detected somewhere in the system, but then also the location of the fault must be determined. Therefore, for each fault, a method of detecting the location of the fault must be obtained. This fault detection is depending on the communication between the turbines, and can basically be divided into three different options.

- Fault detection using full monitoring of all turbines by an overall control system simplifies the procedure of locating the fault, but requires communication of large quantities of data.

- Reducing the communication between the turbines, each turbine will send/recieve a fault signal as well as communication of the direction of the fault from each turbine to an overall controller or the neighbor turbines. Then, the faulted cable is the cable between the turbines with different directions of the fault and the signal

to disconnect can come either from the overall controller or from communication with the neighbor turbines.

- Eliminating the communication between the turbines, the “handshaking” method as described in [67] can be used. Then the turbine determines the direction of the fault and all disconnecters are opened in the faulted radial. Then, the turbines that see a fault further out in the radial increases the voltage on the cable towards the main converter. The next turbine then see the increase in the voltage and connects the turbine. However, if the turbine see a fault towards the main converter, the turbine is not restarted and no signal for reconnection is sent to the turbine towards the main converter.

For the detection and location of the faults in Sections 7.3.4 and 7.3.5, it is stated if the faults need full communication to be detected and located, if limited communication is sufficient or if the handshaking method can be used without communication. However, it should be noted that a limited communication is still needed to disconnect all turbines in the case of a fault. As shown in these sections, for low impedance short circuit faults, the fault can be detected and the direction of the fault can be determined in each turbine. Thereby, the overall controller just needs to handle two status signals from the turbines for these faults; the signals showing the detection of the fault and also the direction of the fault. Also high impedance ground faults can be detected in each turbine and the direction can be determined. However, the fault detection is slower compared to the low impedance faults since integration is needed for accurate detection of the fault. On the other hand, the detection of high impedance short circuit faults requires communication between the turbines, since the fault is detected by the resulting additional power loss.

Disconnection of a Fault without DC Breakers

When a fault has been detected, the DC bus must be discharged before the faulted part can be disconnected and the rest of the system can be restarted. If no DC breaker is available, the whole DC bus must be discharged, including the input capacitance to the main converter. The currents and voltages for the system during the disconnection of the fault without DC breakers can be seen in Fig. 7.12

When the fault has been detected at t = 0.12 s, a signal is sent to the turbines to be turned off and to operate in the same stand-by mode as during a grid fault. The input currents to the DC bus from the turbines are then decreased to zero as seen in Fig. 7.12 (b). When the inputs to the DC bus have been turned off, the DC bus is discharged by a breaker resistance located at the input of the main converter. This breaker resistance is dimensioned to take the rated output power from the system. Consequently, the voltage for the DC bus is decreased as seen in Fig. 7.12 (c) and the currents in the radials are decreasing rapidly

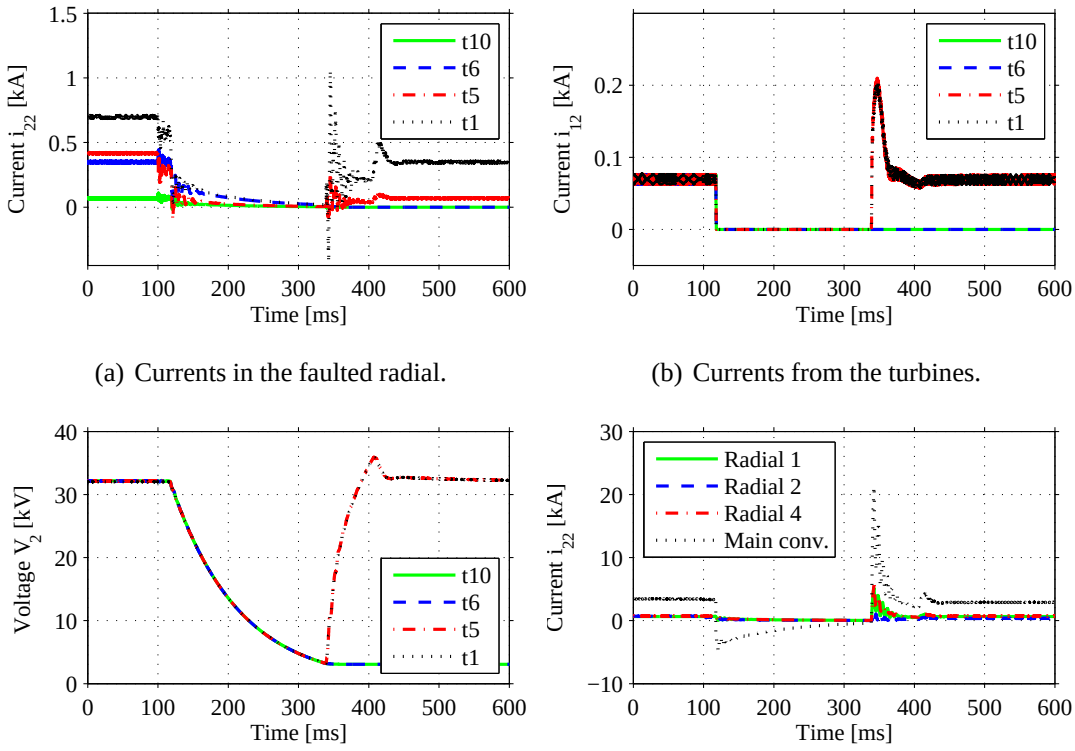

(a) Currents in the faulted radial.

(b) Currents from the turbines.

(c) Voltages in the faulted radial.

(d) Currents from the radials.

Fig. 7.12 Voltage and current waveforms for the internal DC bus during the disconnection of a fault without DC breakers.

with the decreasing voltage as seen in Fig. 7.12 (a). Also the currents from the radials are decreasing as seen in Fig. 7.12 (d), and the current from the main converter has changed direction since the breaker resistance is located before the main converter.

The voltage is decreasing until just 10 % of the rated voltage is remaining, and then the disconnecter is opened as seen in Fig. 7.12 (c). After the opening of the disconnecter and isolating the faulted part (the fault is between turbines 5 and 6 in radial 2), the system can be recharged again, and then the wind farm can reconnect to the main converter and the HVDC link. As seen in Fig. 7.12 (b), the output currents from the turbines are increased and also the currents in the radials to the main converter. The reason for the high currents in the beginning of the reconnection is the low voltage at the DC bus. When the rated voltage for the DC bus has been reached, the main converter is turned on and after an overshoot in the voltage, the main converter keeps the DC bus voltage at the rated value.

The input current and voltage for the HVDC link during the reconnection are seen in Fig. 7.13. Here, it can be seen that the main converter is turned off when the discharging starts for the DC bus. Consequently, the input current decreases as seen in Fig. 7.13 (a)

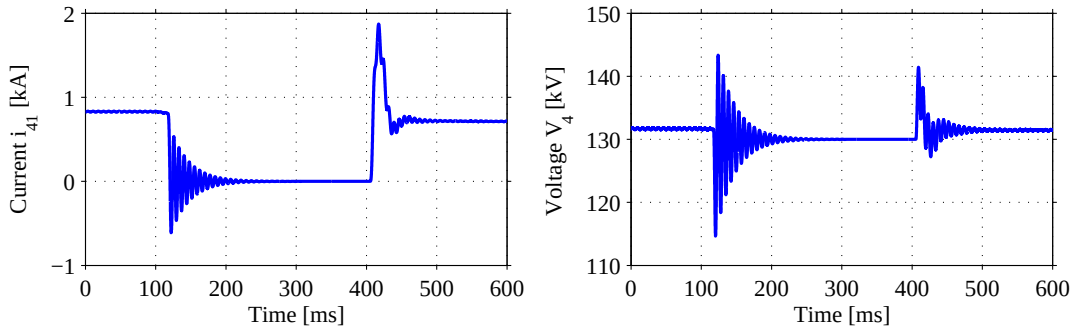

(a) Input current to the HVDC link.

(b) Voltage at input of the HVDC link.

Fig. 7.13 Voltage and input current for the HVDC link during the disconnection of a fault without DC breakers.

and after some oscillations the current goes to zero. At the reconnection, there is an over current when the main converter eliminates the over shoot in the voltage. Also the voltage for the HVDC link seen in Fig. 7.13 (b) have some oscillations resulting from the current oscillations during turn on and turn off.

Looking at the time for the disconnection of the faulted part, it can be seen that the slowest part is the discharge of the system, which takes 220 ms. The charging of the system takes 46 ms, and the total time for disconnection of a faulted part and the reconnection of the non-faulted part are thereby just below 300 ms. However, if the over current from the turbines in Fig. 7.12 (b) is limited to the rated current, the time for charging increases to 163 ms. The time for the disconnection can be decreased considerably if a breaker resistance allowing a larger current is used.

Disconnection of a Fault Using DC Breakers

In the case when a DC breaker is available at the connection between each radial and the main converter, the faulted radial is disconnected immediately when a fault has been detected. The voltage and current waveforms during the disconnection can be seen in Fig. 7.14.

As seen in Fig. 7.14 (d), the non-faulted radials stay connected, and there is just a decrease by 20 % in the current to the main converter. For the faulted radial, the procedure for the disconnection is the same as for the fault without the DC breaker. When the fault has been detected, the DC breaker is opened to isolate the faulted radial. This radial is then discharged with a breaker resistance as shown in Fig. 7.14 and when the voltage has been reduced to 10 % of the original voltage, the disconnecter to the faulted part is opened. The time for the discharge is faster, even though the maximum discharge current

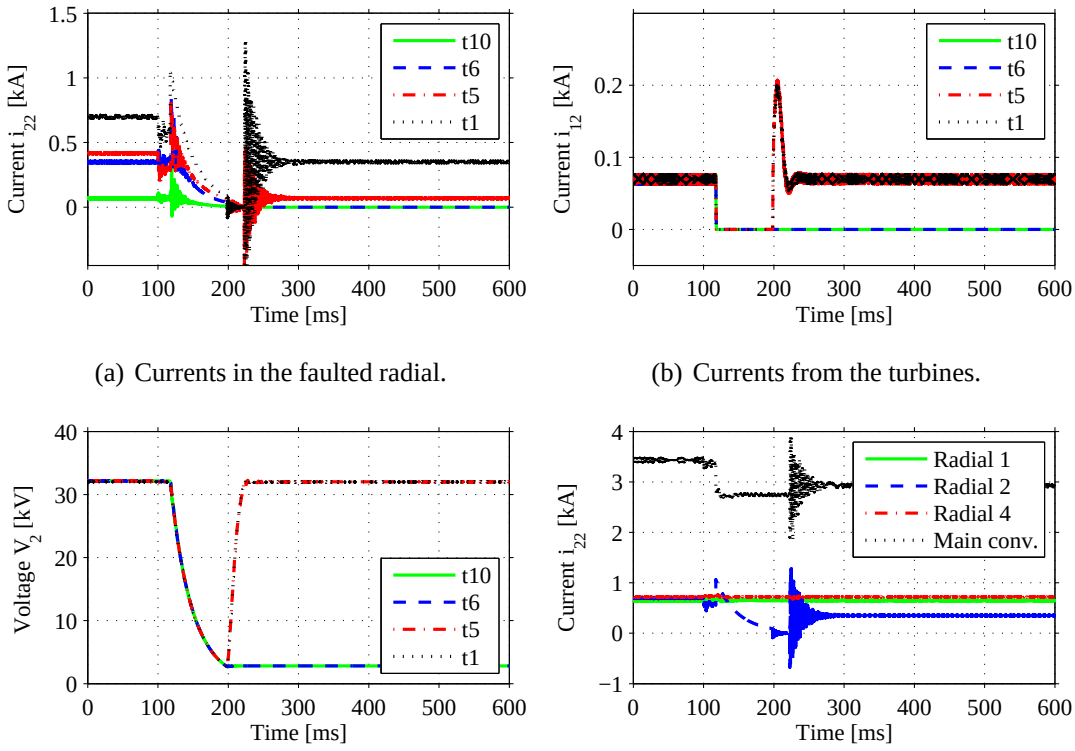

(a) Currents in the faulted radial.

(b) Currents from the turbines.

(c) Voltages in the faulted radial.

(d) Currents from the radials.

Fig. 7.14 Voltage and current waveforms for the internal DC bus during the disconnection of a fault using DC breakers.

is the same as the rated current for the disconnected part, just as in the case without the DC breakers. However, the radial is disconnected from the main capacitance at the input of the main converter, and just the capacitances in the radial have to be discharged. The time for discharge is 80 ms compared to 220 ms for the case without the DC breaker. When the faulted part has been disconnected, the capacitances for the part that should be reconnected are charged again. This charging is also faster than for the case without DC breakers, 25 ms compared to 46 ms for the system without DC breaker. The total time for the disconnection of the faulted part and the reconnection of the non-faulted parts is then just above 100 ms, which should be compared to 300 ms in the case without DC breakers. Further, if the over current from the turbines during the charging is eliminated, the time for charging the radial increases to 45 ms.

Looking at the input to the HVDC link, the current and voltage waveforms are shown in Fig. 7.15.

Here, it can be seen that the current is not decreased to zero as in the case without DC

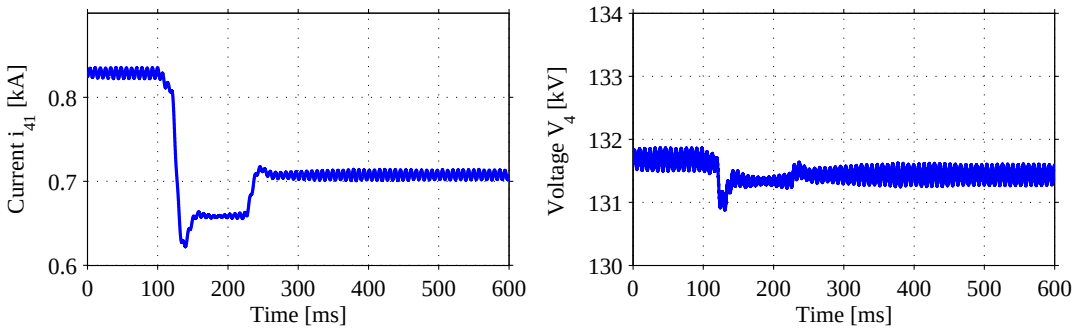

(a) Input current to the HVDC link.

(b) Voltage at input of the HVDC link.

Fig. 7.15 Voltage and input current for the HVDC link during the disconnection of a fault using DC breakers.

breakers. During the disconnection, the current from the faulted radial is removed, and after the disconnection the current from the non-faulted part is reconnected. This results in much less disturbances for the HVDC link, and also the voltage have significantly less oscillations than in the case without a DC breaker.

7.3.4 Detection of Line-to-Line Cable Faults in the DC Grid

For line-to-line short circuit faults, the detection of the fault is depending on the impedance of the fault. For a low impedance fault, the detection is quite easy due to the large fault currents. Also, a fast detection is important to lower the stresses for the components during the fault. In the case of a short circuit fault for the DC bus, a large fault current will discharge all capacitors connected to the DC bus. For a low impedance fault, the fault will be harder to detect since there is no large fault current. However, the detection is not as critical as for low impedance faults since there will not be that large stresses for the system. When a fault occurs in the system, the fault must be detected and the faulted part must be disconnected if the non-faulted parts of the system should continue to operate. Here, both the detection of the fault and the procedure to find the location of the fault are described.

For the line-to-line short circuit faults, it is stated in [16] that short circuit faults can be detected by an over current, and the direction of the fault can also be determined by the fault current. For the simulation of these faulted conditions, a line-to-line fault is inserted between turbines 5 and 6 in radial 2 in the wind farm, as shown in Fig. 7.16 with the resulting fault currents.

As can be seen in the figure, when a short circuit fault occurs there is a fault current discharging the DC link capacitors, which size depends on the fault impedance.

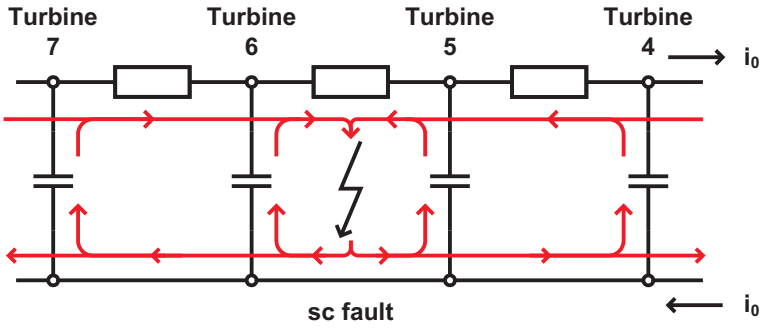

Fig. 7.16 Location of the short circuit fault between turbines 5 and 6 in radial 2 with the resulting fault currents.

Low Impedance Line-to-Line Faults

In the case of a low impedance fault, the voltage at the DC bus will be decreased when the capacitors are discharged. This gives high fault currents, and if the fault has not been detected and the turbines are still in operation, this current will be added to the steady state current. The resulting currents in the faulted radial are plotted in Fig. 7.17 and the currents from all 5 radials to the main converter are shown in Fig. 7.18. It should be noted that the currents from radials 1 and 3 are the same as well as the currents from radials 4 and 5.

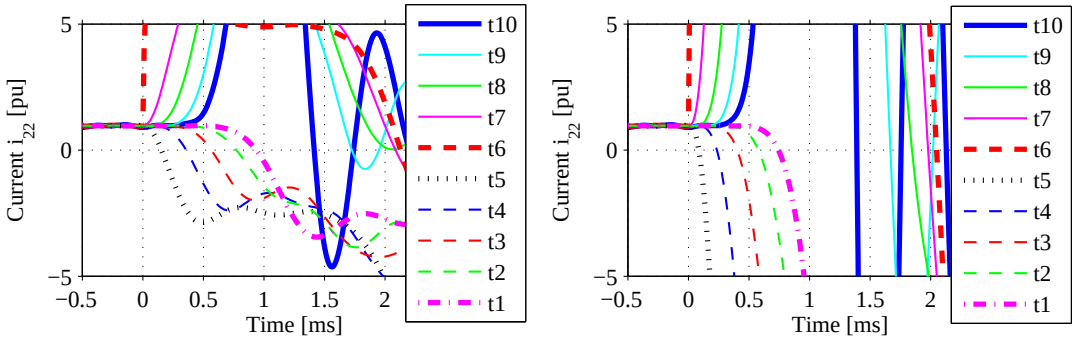

(a) Fault resistance 10 Ω. (b) Fault resistance 1 Ω.

Fig. 7.17 Current in radial 2 in the case of a low impedance short circuit fault between turbines 5 and 6.

In these figures, the currents are plotted in pu of the current at full power. It can be seen that there are large over currents in the case of a short circuit fault when the capacitances in the system are discharged. Also, there will be a large current flowing into the faulted radial in the case of a short circuit fault.

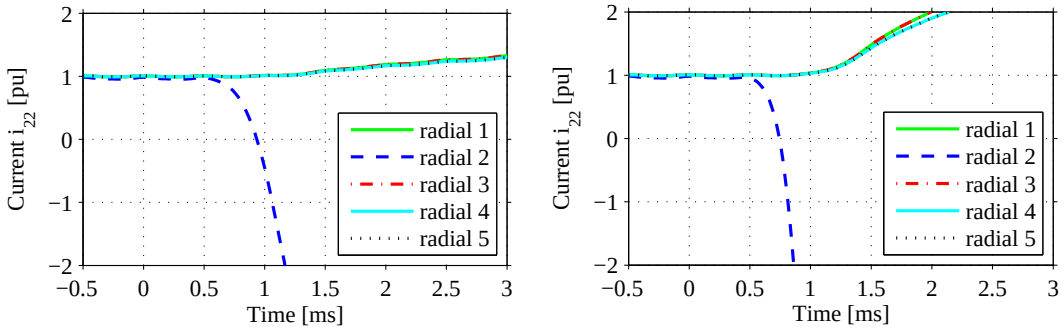

(a) Fault resistance 10 Ω. (b) Fault resistance 1 Ω.

Fig. 7.18 Current from all radials in the case of a low impedance short circuit fault between turbines 5 and 6 in radial 2.

Starting with the detection of the fault, it can be seen in Figs. 7.17 and 7.18 that there is an obvious over current that can be detected as well as the reversal of the direction of the current from radial 2, which should not occur during normal steady-state operation.

When the fault has been detected, the fault must also be located if the faulted part should be disconnected. Looking at the currents in the faulted radial in Fig. 7.17, it is obvious that the fault is between turbines 5 and 6 since turbines 1-5 have negative fault currents and turbines 6-10 have positive faults currents. Each turbine then knows the direction of the fault current, but to be able to locate the fault, the direction of the fault current must be compared for the different turbines. To avoid a complicated communication, each turbine finds the direction of the fault current that is sent to either an overall controller for the wind farm or to the turbine next to each other. If two turbines have the same direction for the fault current, the fault is not between the turbines and they can stay connected. However, if two turbines have different directions of the fault current, there is probably a fault in between them, and the turbine closest to the main converter will then disconnect the cable to the next turbine. Here, also the “handshaking” method can be used since the turbines can determine the direction of the fault without using communication between the turbines.

High Impedance Line-to-Line Faults

For high impedance short circuit faults, there is no fault current large enough to detect the fault and there are no large stresses for the system. However, detecting a fault with high impedance can prevent the fault to develop into a low impedance fault with resulting over currents. Also, it is desirable that the fault is detected if there is a personal accident in the wind turbine. If a person is causing a short circuit, the aim is to detect and clear the fault as soon as possible. The fault resistances used in the simulations are 3 kΩ of a dry person

and 1 kΩ of a wet person [72].

As previously mentioned, a fault with a high resistance does not cause high over currents due to the discharge of the DC link. In Fig. 7.19, the current in the faulted radial is shown in the case of a short circuit fault between turbines 5 and 6. Here, the highest current is at turbine 1 closest to the main converter and the lowest current is at turbine 10 which is the last turbine in the radial.

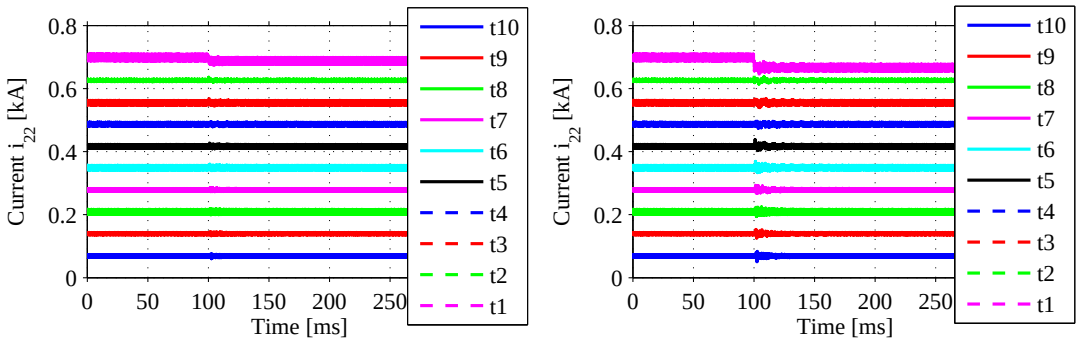

(a) Fault resistance 3 kΩ.

(b) Fault resistance 1 kΩ.

Fig. 7.19 Current in the radial in the case of a high impedance short circuit fault between turbines 5 and 6.

In the figure, it can be seen that turbines 6-10 have the same current before and after the fault, but the current for turbines 1-5 are decreasing. For the short circuit fault, the fault current i_{fault} can be expressed as

$$i_{fault} = \frac{V_2}{R_{fault}}, \tag{7.9}$$

where V_2 is the DC link voltage and R_{fault} is the fault resistance. For the rated voltage V_2 = 32 kV and the fault resistances 3 kΩ and 1 kΩ, the resulting fault currents are 10.7 A and 32 A. Consequently, the power P_{fault} is dissipated in the fault, which can be calculated as

$$P_{fault} = i_{fault} V_2 = \frac{V_2^2}{R_{fault}}. \tag{7.10}$$

For the fault resistances 3 kΩ and 1 kΩ, the power dissipated in the fault is 340 kW and 1024 kW. Depending on the location of the fault in the radial and the operating point of the wind farm, the power dissipated in the fault can be a significant part of the transmitted power. In Fig. 7.20, the fraction of the losses in the fault compared to the transmitted

power in the cable is shown for all turbines in the radial for the fault resistances 3 kΩ and 1 kΩ. The turbines are operating at full power, and a lower power level would increase the fraction of the losses.

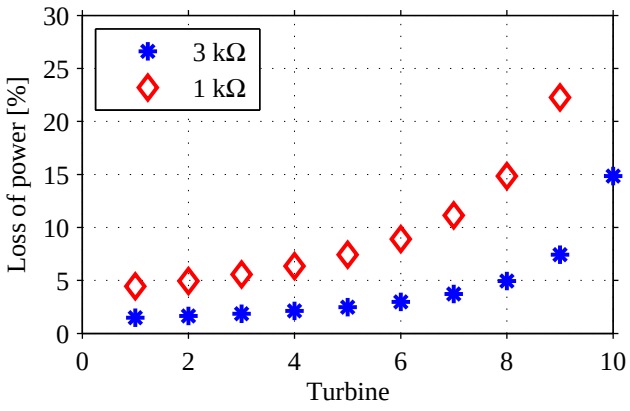

Fig. 7.20 Fraction of the losses dissipated at a short circuit fault depending on the location in the radial.

As seen in the figure, the relative power losses caused by a high impedance fault differs depending on the location in the radial. For the last turbine in the radial, the power loss is 15 % for a 3 kΩ fault and 45 % for a 1 kΩ fault. For the turbine closest to the main converter, the power for the fault is just 1.5 % for a 3 kΩ fault and 4.5 % for a 1 kΩ fault. Measuring the power sent from one turbine and the power received at the next turbine, the power losses in the cable can be calculated. A significant increase in the power losses in the cable will then indicate a fault. Consequently, in the case of ideal measurements, all faults can be easily detectable. However, if there are deviations in the measurements, the faults with highest impedance close to the main converter can be hard to detect.

To detect the high impedance short circuit faults, communication is needed between the turbines in order to calculate the power loss between the turbines. Thereby, the fault detection is slower since data of the power flow must be processed by the overall controller, and not just signals stating the occurrence and direction of a fault from the turbines.

7.3.5 Detection of Line-to-Ground Faults

At the connection point of each turbine to the DC bus, grounding is inserted using grounding capacitors as suggested in [16]. In the case of a ground fault at the DC bus, all grounding capacitors contribute to the fault current [16]. The fault current will then be lower compared to the short circuit fault where all DC link capacitors are contributing. The main fault currents during the discharge of the grounding capacitors are shown in

Fig. 7.21.

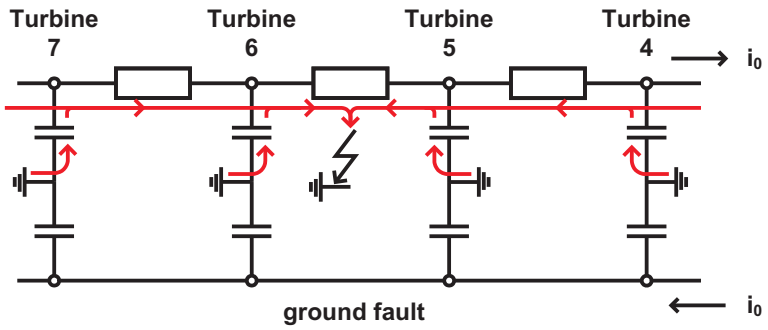

Fig. 7.21 Location of the positive ground fault between turbines 5 and 6 in radial 2 with the resulting fault currents.

The fault can either be detected by an over current or by the changed potentials for the lines. For low impedance ground faults that could be detected by an over current, the first over current at the discharge should be detected and the direction of the fault current should be determined. When the fault current is not high enough to detect an over current, the second option for fault detection is to detect the deviation in the potential for the lines. Then, integrating the difference between the positive and negative line currents can show the location of the fault.

Here, ground faults with both low and high impedance will be investigated and the detection and location of the faults will be shown. Further, the grounding capacitors as well as the series resistance will be dimensioned for a robust detection of the ground faults.

Low Impedance Line-to-Ground Faults

Starting with low impedance ground faults, there will be a high discharge current when the grounding capacitors are discharged as shown in Fig. 7.21. When a ground fault occurs, the grounding capacitor connected to the faulted cable is discharged and the non-faulted cable will take the whole line-to-line potential. In Fig. 7.22, the currents and the voltages for the faulted radial are shown in the case of a ground fault for the positive cable with a fault resistance of 10 mΩ. The values used for the grounding capacitors are C_g = 10 μF and R_{gr} = 40 Ω. Here, it can be seen that when the fault occurs at t = 0.1 s, the potential for the faulted cable is decreased to the ground potential and there are some oscillations for both the currents and voltages before the operation goes back to the same operation point as before the fault, but with changed potentials for the cables.

In Fig. 7.23, the behavior of the system in the case of a ground fault is shown in detail.

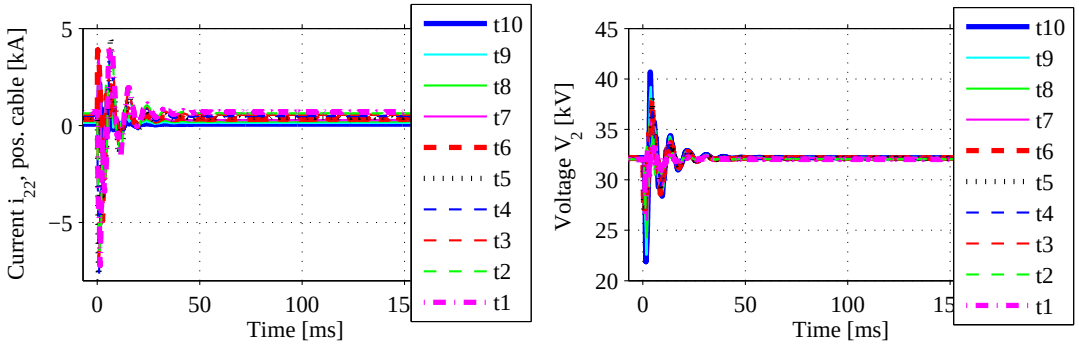

(a) Currents in the faulted radial.

(b) Line-to-line voltages for the faulted radial.

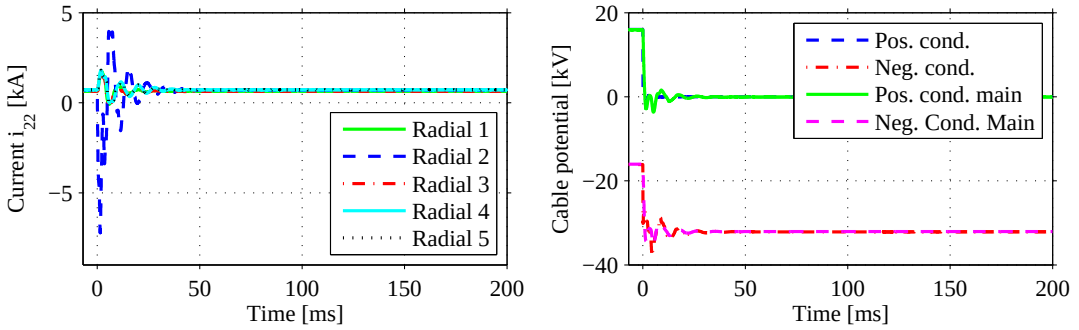

(c) Currents from the five radials to the main converter.

(d) Potentials for the lines, both at the fault and at the main converter.

Fig. 7.22 Currents and voltages for the DC bus in the case of a low impedance ground fault between turbines 5 and 6 in radial 2.

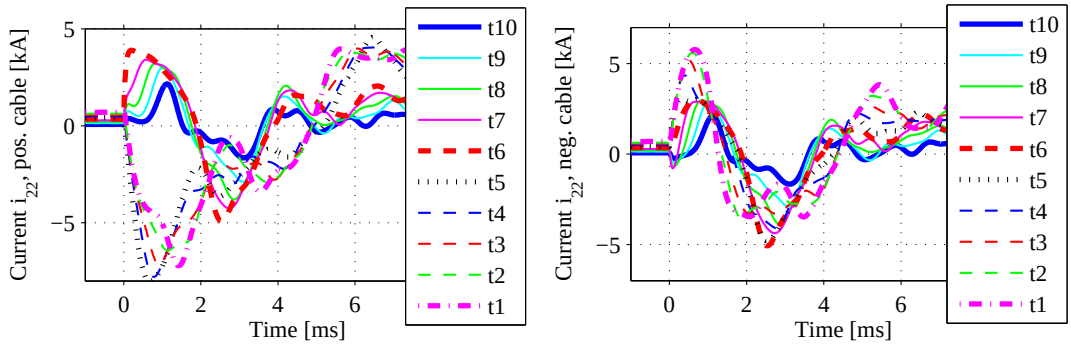

(a) Currents in the positive cable of the faulted radial.

(b) Currents in the negative cable of the faulted radial.

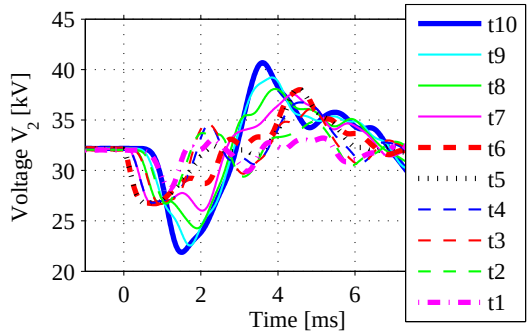

(c) Line-to-line voltages for the faulted radial.

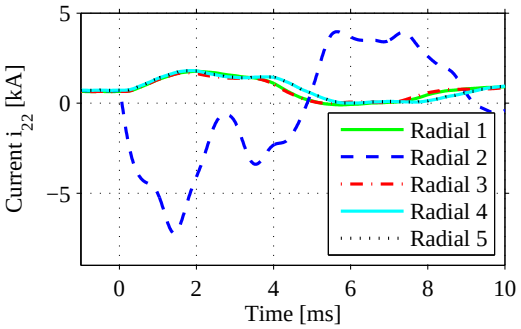

(d) Currents from the five radials to the main converter.

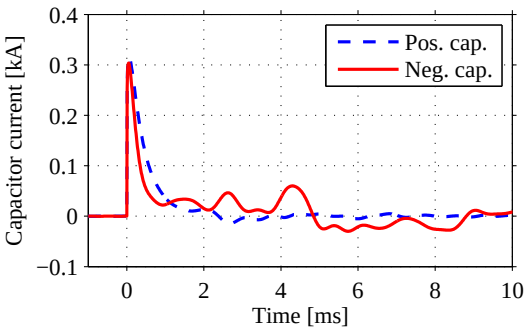

(e) Currents for the grounding capacitors closest to the fault.

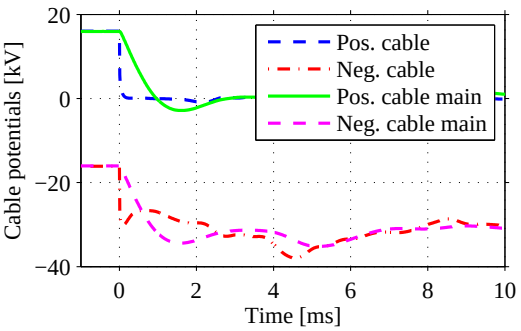

(f) Potentials for the cables, both at the fault and at the main converter.

Fig. 7.23 Currents and voltages for the DC bus in the case of a low impedance ground fault between turbines 5 and 6 in radial 2.

Starting from the fault currents discharging the grounding capacitors seen in Fig. 7.21, it can be seen that the fault currents for turbines 6-10 are positive and the fault currents for turbines 1-5 are negative, which is also seen in Fig. 7.23 (a). It can also be seen, both for the currents in Fig. 7.23 (a) and the voltages in Fig. 7.23 (c), that there is a time constant for the discharge between the different turbines where each cable segment gives a delay. However, there is not just the currents discharging the grounding capacitors that contribute to the increased currents in the system. In Fig. 7.23 (b), it can be seen that there is an increase in the current also for the negative potential. Further, in Fig. 7.23 (c), it can be seen that the voltage is initially decreased, which means that the filter capacitors connected to the output of each turbine are discharged, resulting in an increased current. Consequently, there will be an increase in the current also for the negative cable. For the positive cable, this discharge of the capacitors will be added to the current for discharge of the grounding capacitors for turbines 6-10. However, for turbines 1-5, the discharge current from all grounding capacitors in the system becomes much larger than the discharge current for the filter capacitances and the current will therefore be negative. In Fig. 7.23 (d), it can be seen that the major part of the negative current for turbines 1-5 is from the discharge of the grounding capacitors in the other radials.

For the grounding of the DC bus, both the values of the capacitances and the series resistances should be chosen. Starting with the resistances, the value should be small enough to detect a significant over current. Looking at the wind farm operating at full power, the load resistance R_{load} seen from a radial is calculated as

$$R_{load} = \frac{V_{load}}{i_{load}} = \frac{32000}{710} = 45\Omega. \tag{7.11}$$

Assuming that the resulting current from the discharge of one capacitor should be similar to the load current, the resistance should have a similar value as the load. However, it should be considered that each ground capacitor just have half the line-to-line voltage which will reduce the load current. On the other hand, currents from several grounding capacitors will contribute to the over current. Thereby, the resistance R_{gr} is chosen to be 40 Ω. In the case of no inductance in the system, the initial value of the current discharging the capacitor is then the voltage divided by the resistance giving 16000/40 = 400 A. As seen in Fig. 7.23 (e), the initial current is 300 A due to the inductance in the system and also the fast decrease of the potential for the positive conductor seen in Fig. 7.23 (f). In Fig. 7.24, the currents and voltages are shown for different values of the resistance R_{gr} connected in series with the grounding capacitors. Further, the discharge current for the grounding capacitors is shown in Fig. 7.25.

Here, it can be seen that for a lower value of the resistance, the oscillations for both the currents and the voltages are increasing as seen in Fig. 7.24. However, the difference is

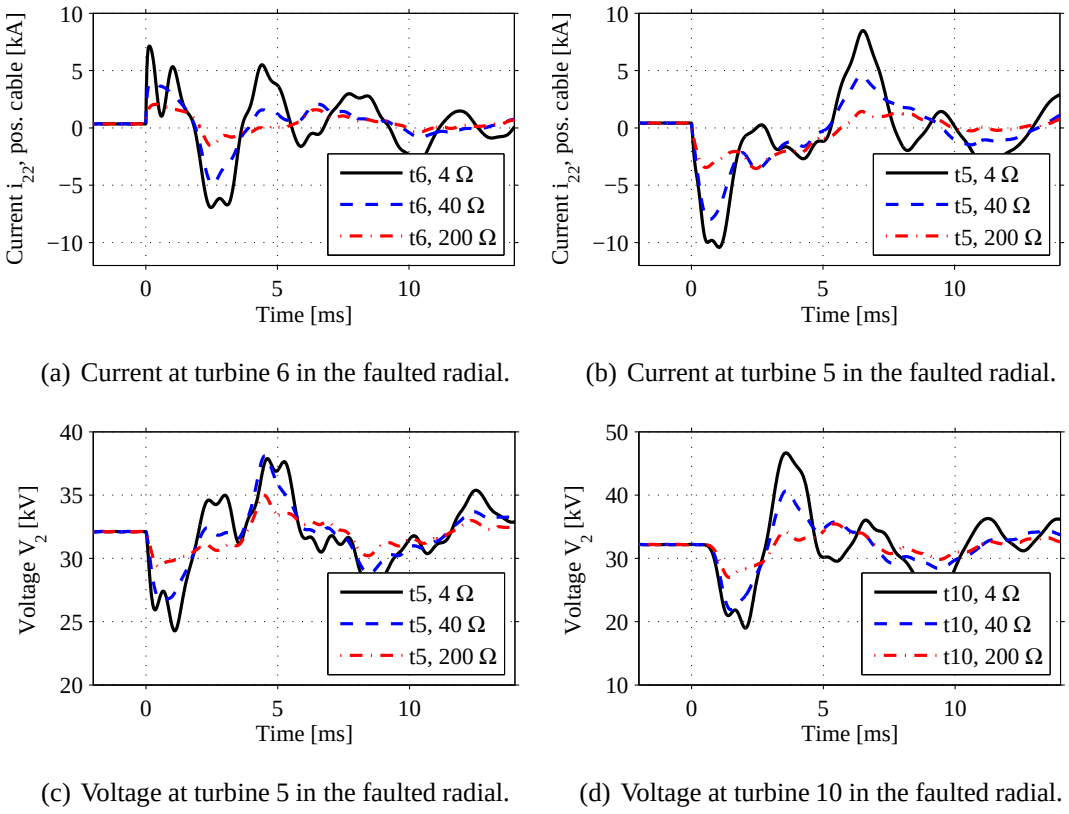

(a) Current at turbine 6 in the faulted radial.

(b) Current at turbine 5 in the faulted radial.

(c) Voltage at turbine 5 in the faulted radial.

(d) Voltage at turbine 10 in the faulted radial.

Fig. 7.24 Currents and voltages for the DC bus in the case of a low impedance ground fault between turbines 5 and 6 in radial 2, using grounding resistances 4 Ω, 40 Ω and 200 Ω.

not proportional to the value of the resistance since a large part of the over current is a result of the voltage oscillations at the cable. For the discharge current of the grounding capacitors shown in Fig. 7.25, the relation between the value of the resistance and the resulting current magnitude is more obvious. The large current magnitude for the low resistance will then result in the larger oscillations for both the current and the voltage seen in Fig. 7.24.

Also, the value of the capacitance should be determined. In Fig. 7.26, the resulting current and voltage waveforms are shown for a low impedance ground fault using different grounding capacitances. In Fig. 7.27, the current for the discharge of the grounding capacitances is shown.

For a constant value of the resistance, an increasing value of the capacitance will increase the time constant but not the peak current from each capacitor as seen in Fig. 7.27. However, the peak current in the faulted radial will increase since the increased time constant for the discharge will result in that a larger number of the capacitors are discharged at

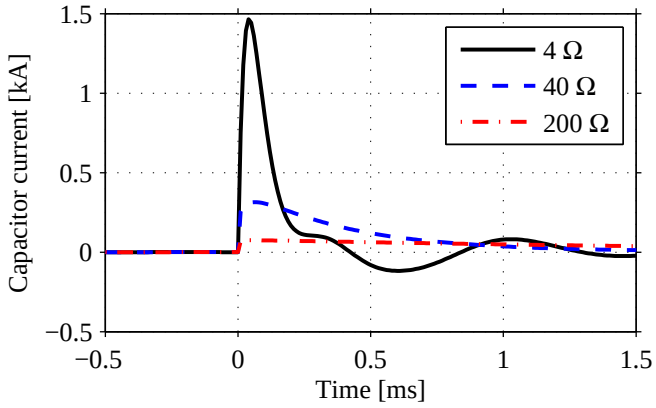

Fig. 7.25 Current for the grounding capacitor in the case of a low impedance ground fault between turbines 5 and 6 in radial 2, using grounding resistances 4 Ω, 40 Ω and 200 Ω.

the same time as seen in Fig. 7.26 (a) and (b). The time constants between the different turbines and thereby also the different capacitors should also be considered. If the capacitance is low and the grounding capacitors closest to the fault have been discharged before the discharge of the next capacitor has started, there will be a lot of oscillations and it is hard to detect the location of the fault. As seen in Fig. 7.23 (c), the approximate delay between the discharges of two capacitors are 0.2 ms. Thereby, an appropriate value of the time constant τ_g for the discharge of the capacitor can then be 0.4 ms. The value of the capacitor C_g will then be

$$\tau_g = R_{gr}C_g \Rightarrow C_g = \frac{\tau_g}{R_{gr}} = \frac{0.4 \cdot 10^{-3}}{40} = 10\mu F. \tag{7.12}$$

In Fig. 7.23 (e), it can be seen that the current for the capacitors closest to the fault have decreased from 300 A to 30 A 1 ms after the occurrence of the fault. Thereby, it can be seen that the additional inductances in the system make the discharge slower, especially when there are large current derivatives for the lines as shown in Fig. 7.23 (a). Using the capacitance 1 μF, this time constant is 0.15 ms and for 100 μF it is about 10 ms as seen i Fig. 7.27.

Regarding the detection and localization of a low impedance ground fault, it can be seen that the over current in the faulted radial indicates the occurrence of a fault and also the change in potentials for the cables indicates that there is a fault and for which cable the fault has occurred. Knowing the faulted cable, the location of the fault can be detected by the direction of the fault currents in the faulted cable. However, the location of the fault must be found using the first transient of the fault current since there are large oscillations for the system where the location of the fault can not be determined. Consequently, the

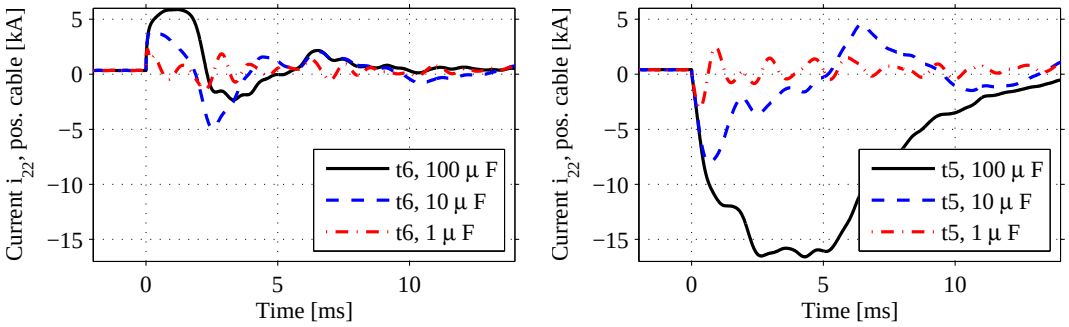

(a) Current at turbine 6 in the faulted radial.

(b) Current at turbine 5 in the faulted radial.

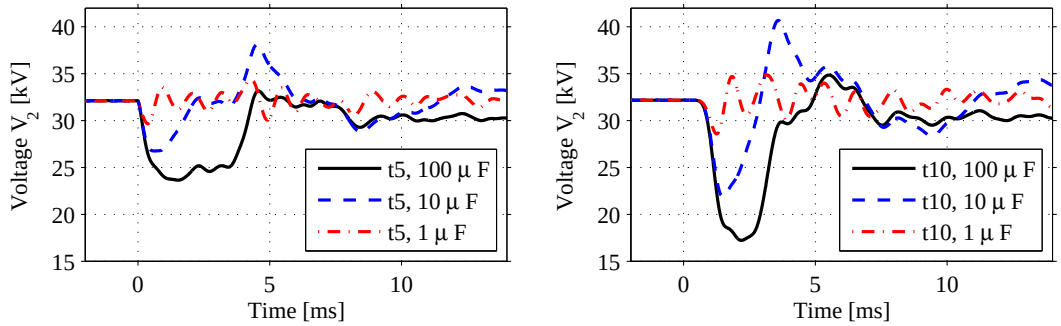

(c) Voltage at turbine 5 in the faulted radial.

(d) Voltage at turbine 10 in the faulted radial.

Fig. 7.26 Currents and voltages for the DC bus in the case of a low impedance ground fault between turbines 5 and 6 in radial 2, using grounding capacitors of 1 μF, 10 μF and 100 μF.

low impedance ground faults can be detected in each turbine without communication and the direction of the fault can also be determined. Then, fast fault detection methods can be used due to the limited need of communication.

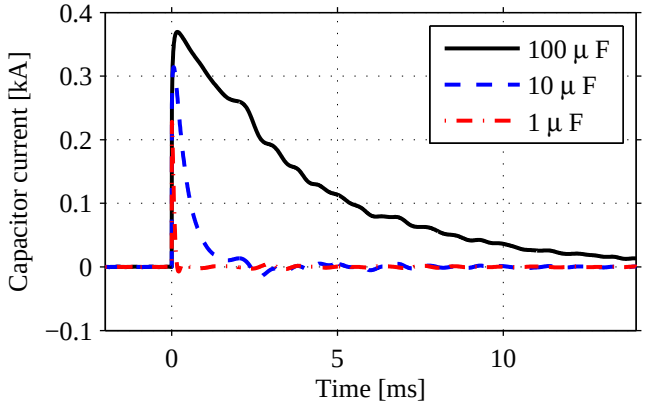

Fig. 7.27 Current for the grounding capacitor in the case of a low impedance ground fault between turbines 5 and 6 in radial 2, using grounding capacitors of 1 μF, 10 μF and 100 μF.

High Impedance Line-to-Ground Faults

In the case of a high fault impedance, it is harder to detect the fault just using the measured currents. In Fig. 7.28, the currents and voltages can be seen for a faulted radial for the fault resistances 0.01 Ω, 1 Ω, 10 Ω and 100 Ω.

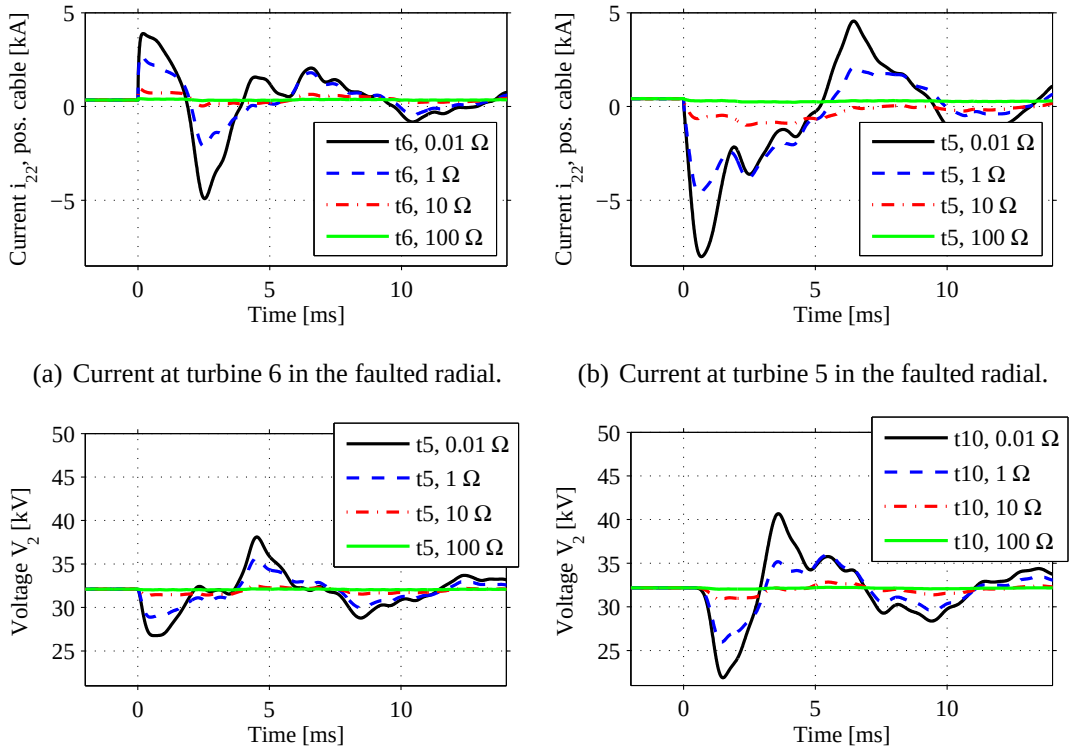

(a) Current at turbine 6 in the faulted radial.

(b) Current at turbine 5 in the faulted radial.

(c) Voltage at turbine 5 in the faulted radial.

(d) Voltage at turbine 10 in the faulted radial.

Fig. 7.28 Currents and voltages for the DC bus in the case of a ground fault between turbines 5 and 6 in radial 2, with the fault resistances 0.01 Ω, 1 Ω, 10 Ω and 100 Ω.

As seen in the figures, the over currents during the fault are significantly lower for an increasing value of the fault resistance. Also the voltage oscillations are decreasing. Thereby, it can be hard to detect and determine the location using the over currents as was done for the low impedance ground faults.

A high impedance ground fault can be detected by measuring the potentials for the cables. Measuring at the main converter, the potentials for the cables are shown in Fig. 7.29. Here, it can be seen that the detection of a ground fault can be made by measuring the potential for the cables, but the location of the fault can not be determined.

To find the location of the fault, the currents must be used. As shown in Fig. 7.21, a

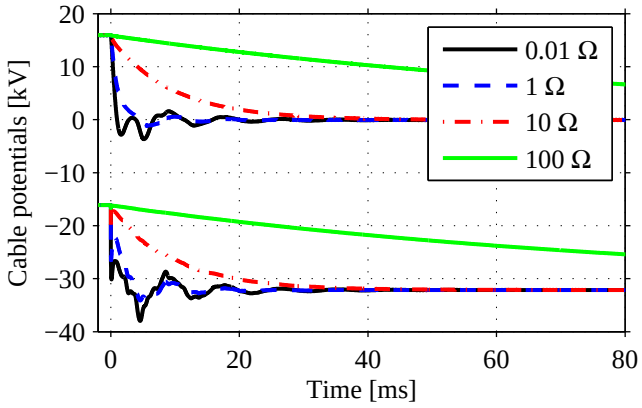

Fig. 7.29 Potential for the cables in the case of a ground fault between turbines 5 and 6 in radial 2, with the fault resistances 0.01 Ω, 1 Ω, 10 Ω and 100 Ω.

ground fault gives common mode currents that in the case of a low impedance fault can be detected by subtraction of the cable currents [16]. For a high impedance fault, Fig. 7.30 shows the currents in the positive and negative cables at the turbines located closest to the fault.

In the figures, it can be seen that there is a clear difference between the currents in the negative conductor and the positive conductor in the case of a ground fault. It can also be seen that the difference is largest for turbine 5 and much smaller for turbine 6. The reason for this is that there are just 5 grounding capacitors that are discharged through the cable at turbine 6, while the remaining 44 grounding capacitors are discharged through the cable at turbine 5. The differences between the currents in the positive and the negative cables are shown in Fig. 7.31.

In the figures, it can be seen that there is a clear difference in the cable currents for the faults with low impedance, but the difference is smaller and harder to detect for high impedance faults. Also, it can be noticed that the sign of the difference between the currents in the cables on the different sides of the fault is different. Thereby, the location of the fault can then be determined using a differential measurement of the cable currents. However, for the high impedance faults, it can be hard to measure the difference in current with good accuracy. One way to improve the detection of the differential currents is to integrate the difference and thereby see longer trends rather than noise and oscillations. In Fig. 7.32, the integrated difference between the currents seen in Fig. 7.31 is shown.

Here, it can be seen that the integrated difference shows that the charge removed by the fault currents is the same independently of the fault resistance since the capacitor values are the same. The integrated current difference for the cable at turbine 5 is about 8 times

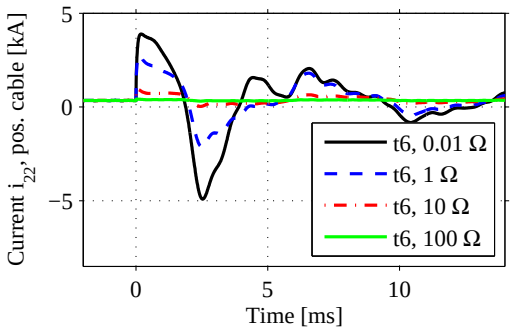

(a) Current for the positive cable at turbine 6 in the faulted radial.

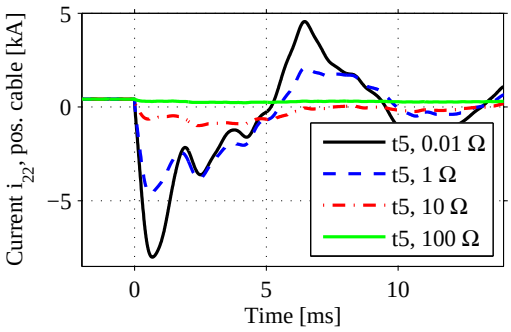

(b) Current for the positive cable at turbine 5 in the faulted radial.

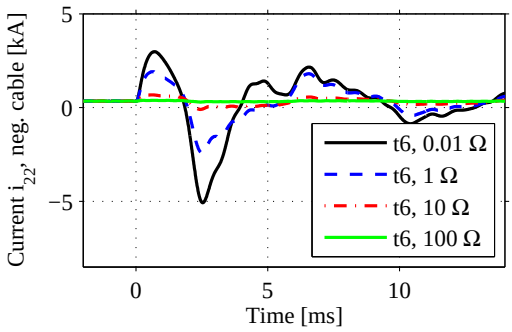

(c) Current for the negative cable at turbine 6 in the faulted radial.

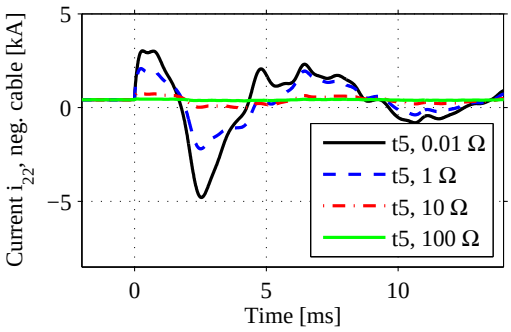

(d) Current for the negative cable at turbine 5 in the faulted radial.

Fig. 7.30 Currents for for cables in the DC bus in the case of a ground fault between turbines 5 and 6 in radial 2, with the fault resistances 0.01 Ω, 1 Ω, 10 Ω and 100 Ω.

the value for the cable at turbine 6. This is due to the 44 capacitors discharged through that cable compared to 5 capacitors for the cable at turbine 6. Further, the location of the fault can be detected using the sign of the integrated current difference for the different turbines. Also for the fault with the highest fault resistance, the integrated values of the current differences clearly show the location of the fault.

Also for the high impedance ground faults, the fault can be detected and the direction of the fault can be determined in each turbine. What is limiting the speed of the fault detection is the time needed for integrating the difference in current between the cables.

7.4 Summary

In this section, the fault handling for the wind farm with an internal DC grid has been investigated. For the faults in the connecting main grid, the performance of the wind farm is shown in the case of a total interruption in the power transfer. At the occurrence of the

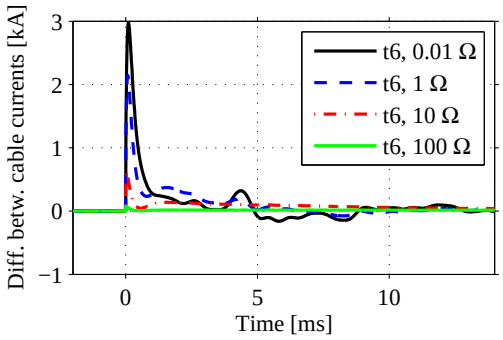

(a) Current difference between the cables at turbine 6 in the faulted radial.

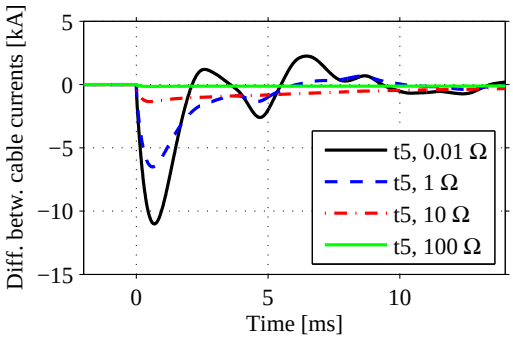

(b) Current difference between the cables at turbine 5 in the faulted radial.

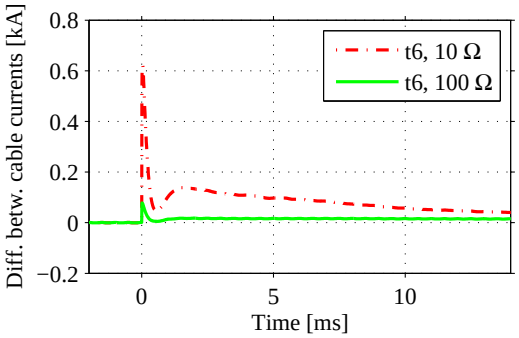

(c) Current difference between the cables at turbine 6 in the faulted radial.

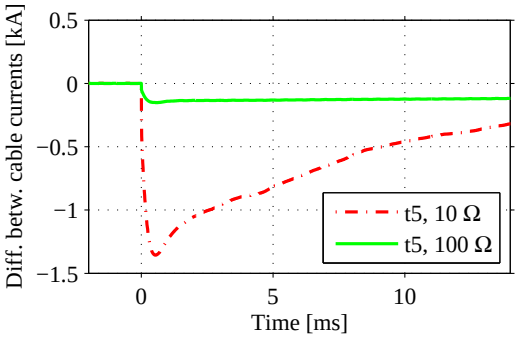

(d) Current difference between the cables at turbine 5 in the faulted radial.

Fig. 7.31 Current difference between the cables in the DC bus in the case of a ground fault between turbines 5 and 6 in radial 2, with the fault resistances 0.01 Ω, 1 Ω, 10 Ω and 100 Ω.

fault, the required performance of the HVDC link is determined. For the reconnection after the fault, the full power is available after 14 ms, which is well within the requirements in existing grid codes. For the internal faults in the wind farm, the focus has been on the faults at the DC bus. The detection and the clearing of the fault was shown for different faults. For the low impedance faults, the detection is made using the resulting over currents and the location of the faults can be found in the same way. For high impedance faults, more communication between the turbines is needed to detect the fault and find the location. When the fault has been detected, the faulted part can be disconnected and the non-faulted parts can be reconnected within 100 ms with a DC breaker for each radial and within 300 ms without DC breakers.

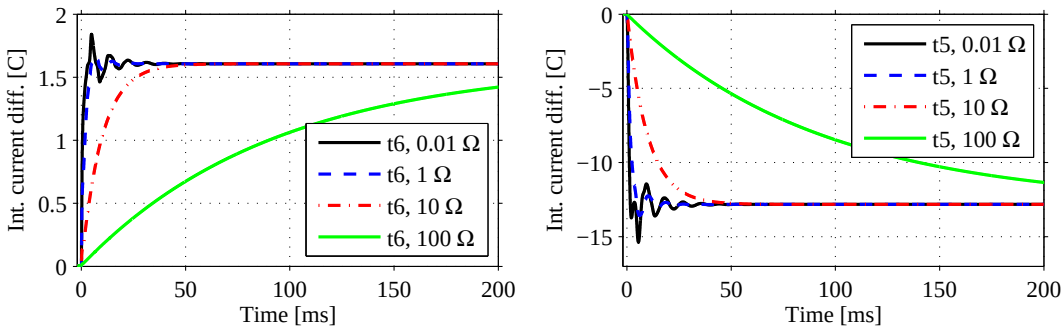

(a) Integrated current difference between the cables at turbine 6 in the faulted radial.

(b) Integrated current difference between the cables at turbine 5 in the faulted radial.

Fig. 7.32 Integrated current difference between the cables in the DC bus in the case of a ground fault between turbines 5 and 6 in radial 2, with the fault resistances 0.01 Ω, 1 Ω, 10 Ω and 100 Ω.

Chapter 8

Conclusions and Future Work

8.1 Summary and Concluding Remarks

In this thesis, a wind farm with an internal DC collection grid is investigated with focus on the design, the losses and the dynamical behavior of the DC grid. For the implementation of an internal DC grid, the DC/DC converters are identified as key components. A suitable design of the DC/DC converters is obtained including the choice of topology, the control of the converter and also the choice of switching frequency. For the chosen switching frequency of 1 kHz, the weight of the medium frequency transformer in the DC/DC converter is reduced by 90 % compared to a corresponding 50 Hz transformer. In addition, the loss calculations for the DC/DC converters are verified using a down scaled experimental setup.

For the investigations of the DC collection grid, a wind farm with the same layout as the wind farm Lillgrund is chosen. Here, 48 turbines of 2.3 MW each, located in 5 radials, are connected to an offshore platform. In the investigated DC system, a DC/DC converter in each wind turbine increases the 1.5 kV DC link voltage in the turbine to 32 kV for the internal DC bus. Then, a main DC/DC converter for the whole wind farm increases the DC voltage to 130 kV for the HVDC transmission. For the DC system in the wind farm, the total losses are 3 % of the transferred power, where the losses for the DC/DC converter in the wind turbine are 1.35 % and for the main DC/DC converter 1.41 %. The losses in the internal DC bus are 0.24 %. The losses for the DC system are similar to the losses for a corresponding AC system.

Considering the dynamic operation of the internal DC collection grid in the wind farm, the DC/DC converters control the power flow and thereby also the voltage levels for the DC links. The voltage control for the DC collection bus is achieved by the main DC/DC converter connected to the HVDC link, and the voltage for the DC link in the wind turbine is controlled by the wind turbine DC/DC converter. The control method used for the control

of the voltage is a droop control that works without communication within the wind farm. By determining the maximum voltage variations, and limiting the bandwidth due to the 1 kHz switching frequency, the required DC link capacitances were found to be 152 mF for the DC link in the wind turbine and 16 mF for the internal DC bus. The stored energy in both DC links will then correspond to 74 ms transferred rated power. This capacitance can be lowered by increasing the bandwidth of the controller, but then the stability margin is decreased. Further, the startup procedure of the wind farm has been developed and shown to be appropriate. Due to the unidirectional power flow in the DC/DC converters, the system must be energized from the wind turbines, and it is shown that the wind farm can start up and the DC bus can be energized using 500 V power sources in the wind turbines.

In the case of a fault in the connecting main grid, there are two options to decrease the output power during the fault; either by decreasing the output power from the turbines or by dissipating the excess power in a breaker resistance at the HVDC link close to the grid side converter. In the case of a large breaker resistance, the wind farm will not experience the fault and the power can be reconnected immediately after the fault. If the power flow should be stopped in the turbines, the detection of the fault must be investigated as well as the reconnection after the fault. Here, it was shown that the fault can be detected both with and without communication between the different parts in the system. Also, the required HVDC link capacitance needed to limit the over voltage was determined. Further, after the reconnection of the system, the output power has reached the rated value after 14 ms and the oscillations have been damped after 70 ms, which is well within the time frames specified in the German, Irish and English grid codes.

For the internal faults in the wind farm, the procedures of detecting and locating the fault as well as disconnecting the faulted part have been investigated. For a fault in a wind turbine, the turbine is disconnected and it will not influence the operation of the wind farm significantly. For a severe fault in the main DC/DC converter or the HVDC cable, the whole wind farm must be shut down. However, if there is a fault in the internal DC bus, the operation is affected, but the wind farm can continue operating if the faulted part is disconnected. Here, methods for detecting and finding the location of both line-to-line faults and ground faults have been determined. Also the procedure of disconnecting the fault was shown, both without full power DC breakers and with a DC breaker in each radial. In the case of a DC breaker, four of five radials can continue to deliver power during the disconnection of the faulted part, compared to the case without DC breakers where the whole DC bus must be discharged. In the case without DC breakers, the faulted part is discharged and the non-faulted parts back in operation within 300 ms, and with DC breakers this time will be reduced to just above 100 ms.

8.2 Proposals for Future Work

For the DC/DC converters, the fraction of the losses are significantly higher at lower power levels compared to high power levels. One possible way to reduce the losses at low power is to instead use a modular approach for the DC/DC converters. This could result in that the active modules are operating closer to their rated power at all operating points and thereby also the fraction of the losses will decrease. Also, the high power medium frequency transformer needs further investigation.

In the case of a grid fault, further investigation is needed regarding the interaction between the wind turbines and the DC/DC converters. During steady state operation, the wind turbines aim at maximizing the output power within the allowed operating range and the DC/DC converters control the input voltage level by adjusting the transferred power. However, in the case of a limitation in the output power, the wind turbines must decrease the output power. Thereby, in the case of an increased DC bus voltage, the converter in the wind turbine must limit the power flow, and consequently also the turbine must limit the output power. In this thesis, just the option of stopping all power flow during a grid faults is investigated. However, if the power flow just should be limited during the fault, the control interaction between the DC/DC converters in the turbines, the main DC/DC converter and the wind turbines must be investigated further to avoid oscillations. This is also the case if the wind farm should support the frequency for the main grid and thereby must control the output power.

For normal operation, an aim for further investigation is to reduce the required DC link capacitances by improving the control of the DC/DC converters. As shown in Chapter 6, the control is designed assuming no communication and no limitations for the power variations leading to large required DC link capacitances. Introducing fast communication between the converters can reduce the required DC link capacitance. Also by introducing an integral part of the controller and temporarily allowing larger over voltages or limiting the allowed voltage variations can decrease the needed DC link capacitances.

For further studies of high frequency transients, an improved model of the wind farm with high frequency models of the components should be used. Since the used models for the cables are π-link models, the accuracy for high frequencies can be improved using a high frequency model of the cables. This is mainly interesting for the behavior of the system during internal faults with fast transients.

References

[1] N. Flourentzou, V. G. Agelidis, and G. D. Demetriades, “VSC-based HVDC power transmission systems: An overview,” *IEEE Transactions on Power Electronics*, vol. 24, no. 3, pp. 592 – 602, March 2009.

[2] It’s time to connect - Technical description of HVDC Light®technology. [Online]. Available: http://www.abb.com/hvdc,2009-06-25

[3] N. Barberis Negra, J. Todorovic, and T. Ackermann, “Loss evaluation of HVAC and HVDC transmission solutions for large offshore wind farms,” *Electric Power Systems Research 76 (2006) 916-927*.

[4] W. Kling, P. Bresesti, I. Valadè, D. Canever, and R. Hendriks, “Transmission systems for offshore wind farms in the Netherlands,” in *Proc. Copenhagen Offshore Wind 05*, 2005.

[5] P. Bresesti, W. L. Kling, R. L. Hendriks, and R. Vailati, “HVDC connection of offshore wind farms to the transmission system,” *IEEE Trans. Energy Conversion*, vol. 22, no. 1, pp. 37–43, March 2007.

[6] L. Harnefors, Y. Yang-Häfner, M. Hyttinen, and T. Jonsson, “Ride-through methods for wind farms connected to the grid via a VSC-HVDC transmission,” in *Proc. Nordic wind power conference NWPC 2007,*, 2007.

[7] T. D. Vrionis, X. I. Koutiva, N. A. Vovos, and G. B. Giannakopoulos, “Control of an HVdc link connecting a wind farm to the grid for fault ride-through enhancement,” *IEEE Transactions on power systems*, vol. 22, no. 4, pp. 2039–2047, November 2007.

[8] L. Xu, L. Yao, and C. Sasse, “Grid integration of large DFIG-based wind farms using VSC transmission,” *IEEE Transactions on power systems*, vol. 22, no. 3, pp. 976–984, August 2007.

[9] W. Lu and B.-T. Ooi, “Optimal acquisition and aggregation of offshore wind power by multiterminal voltage-source HVDC,” *IEEE Transactions on power delivery*, vol. 18, no. 3, pp. 201–206, July 2003.

[10] K. Zhou, X. Fu, M. Cheng, X. Zhu, W. Wang, and T. Wang, "Topologies and control of VSC-HVDC systems for grid connection of large-scale off-shore wind farms," in *Proc. Electrical Machines and Systems, 2008. ICEMS 2008. International Conference on* ,, 2008, pp. 2357 – 2361.

[11] D. Jovcic, "Interconnecting offshore wind farms using multiterminal VSC-based HVDC," in *Proc. Power Engineering Society General Meeting*, 2006.

[12] C. Meyer and R. W. De Doncker, "Design of a three-phase series resonant converter for offshore DC grids," in *Proc. the 42th IEEE Industry Application Society Annual Meeting (IAS)*,, vol. 2, 2007, pp. 216 – 223.

[13] A. Prasai, J.-S. Yim, D. Divan, A. Bendre, and S.-K. Sul, "A new architecture for offshore wind farms," *IEEE Trans. Power Electronics*, vol. 23, no. 3, pp. 1198 – 1204, May 2008.

[14] S. Lundberg, "Wind farm configuration and energy efficiency studies - series DC versus AC layouts," PhD Thesis, Dep. of Energy and Environment, Chalmers University of Technology, Göteborg, Sweden, 2006, ISSN-0346-718X.

[15] C. Meyer, M. Höling, A. Peterson, and R. W. De Doncker, "Control and design of DC grids for offshore wind farms," *IEEE Trans. Industry Applications*, vol. 43, no. 6, pp. 1475–1482, November/December 2007.

[16] P. Karlsson, "Dc distributed power systems, analysis, design and control for a renewable energy system," PhD Thesis, Dep. Industrial Elelctrical Engineering and Automation., Lund University, Lund, Sweden, 2002, iSBN 91-88934-25-X.

[17] P. Karlsson and J. Svensson, "DC bus voltage control for a distributed power system," *IEEE Trans. Power Electronics*, vol. 18, no. 6, pp. 1405– 1412, November 2003.

[18] A. Petersson, "Analysis, modeling and control of doubly-fed induction generators for wind turbines," PhD Thesis, Dep. of Energy and Environment, Chalmers University of Technology, Göteborg, Sweden, 2005, ISSN-0346-718X.

[19] C. Meyer, M. Kowal, and R. W. De Doncker, "Circuit breaker concepts for future high-power DC-applications," in *40th Conf . Rec. IEEE IAS Annu. Meeting*, 2005, pp. 860–866.

[20] G. L. Johnson, *Wind Energy Systems*. New Jersey, USA: Prentice-Hall, 1985.

[21] Å. Larsson, "Practical experiences gained at Lillgrund offshore wind farm," in *Proc. 7th International Workshop on Large Scale Integration of Wind Power and Transmission Networks for Offshore Wind Farms*, 2008, pp. 97–104.

[22] R. L. Steigerwald, R. W. De Doncker, and H. Kheraluwala, "A comparison of high-power DC-DC soft-switched converter topologies," *IEEE Trans. Industry Applications*, vol. 32, no. 5, pp. 1139–1145, September/October 1996.

[23] G. D. Demetriades, "Evaluation of different topologies for high-power DC-DC converters," Dep. Electrical Eng., Royal University of Technology, Tech. Rep. ISSN-1404-8248, 2001.

[24] L. Max, "Energy evaluation for DC/DC converters in DC-based wind farms," Dep. of Energy and Environment, Chalmers University of Technology, Tech. Rep., 2007.

[25] L. Max and S. Lundberg, "System efficiency of a DC/DC converter-based wind farm," *Wind Energy Journal*, vol. 11, no. 1, pp. 109– 120, January/February 2008.

[26] A. Bendre, S. Norris, D. Divan, I. Wallace, and R. W. Gascoigne, "New high power DC-DC converter with loss limited switching and lossless secondary clamp," *IEEE Trans. Power Electronics*, vol. 18, no. 4, pp. 1020–1027, July 2003.

[27] R. W. Erickson and D. Maksimović, *Fundamentals of Power Electronics, Second Edition*. Massachusetts, USA: Kluwer Academic Publishers, 2002.

[28] J. Morren, S. W. H. de Haan, and J. A. Ferreira, "Design study and scaled experiments for high-power DC-DC conversion for HVDC-systems," in *Power Electronics Specialists Conference, 2001. PESC, 2001 IEEE 32nd Annual*, vol. 3, 2001, pp. 1529 – 1534.

[29] G. D. Demetriades, "On small-signal analysis and control of the single- and dual-active bridge topologies," PhD Thesis, Dep. Electrical Eng., Royal University of Technology, Stockholm, Sweden, 2005, ISSN-1650-674X.

[30] N. Mohan, T. M. Undeland, and W. P. Robbins, *Power Electronics: Converters, Applications and Design*. John Wiley and Sons INC., third edition, 2003.

[31] L. Mihet-Popa, F. Blaabjerg, and I. Boldea, "Wind turbine generator modeling and simulation where rotational speed is the controlled variable," *IEEE Trans. Industry Applications*, vol. 40, no. 1, pp. 3– 10, January/February 2004.

[32] "FF200R33KF2C data sheet," Eupec, June 2003.

[33] T. Kjellqvist, S. Norrga, and S. Östlund, "Switching frequency limit for soft-switching MF transformer system for AC-fed traction," in *Proc. IEEE PESC 05*, 2005.

[34] "5SLF 20H2500 data sheet," ABB, Doc. No. 5SYA1584-02, May 2004.

[35] R. Petkov, "Optimum design of a high-power, high-frequency transformer," *IEEE Trans. Power Electronics*, vol. 11, no. 1, pp. 33 – 42, January 1996.

[36] M. Sippola and R. E. Sepponen, "Accurate prediction of high-frequency power-transformer losses and temperature rise," *IEEE Trans. Power Electronics*, vol. 17, no. 5, pp. 835 – 847, September 2002.

[37] T. Kjellqvist, S. Norrga, and S. Östlund, "Design considerations for a medium frequency transformer in a line side power conversion system," in *Proc. IEEE Power ELectronics Specialists Conference, PESC 04*, 2004.

[38] POWERLITE®inductor cores, technical bulletin. [Online]. Available: http://www.metglas.com,2009-10-21

[39] M. Albach, T. Durbaum, and A. Brockmeyer, "Calculating core losses in transformers for arbitrary magnetizing currents a comparison of different approaches," in *Proc. PESC 96*, vol. 2, 1996, pp. 1463 – 1468.

[40] J.-G. Cho, J. A. Sabate, H. Guichao, and F. C. Lee, "Zero-voltage and zero-current-switching full bridge PWM converter for high-power applications," *IEEE Trans. Power Electronics*, vol. 11, no. 4, pp. 622 – 628, July 1996.

[41] M. T. Aydemir, A. Bendre, and G. Venkataramanan, "A critical evaluation of high power hard and soft switched isolated DC-DC converters," in *Proc. IEEE IAC'02*, vol. 2, 2002, pp. 1338–1345.

[42] L. Max and T. Thiringer, "Design and control of a 5 MW medium frequency DC/DC converter for a wind turbine," in *Proc. the 2nd EPE Wind Energy Chapter,*, 2009.

[43] M. H. Kheraluwala, D. W. Novotny, and D. M. Divan, "Coaxially wound transformers for high-power high-frequency applications," *IEEE Trans. Power Electronics*, vol. 7, no. 1, pp. 54 – 62, January 1992.

[44] D. Vinnikov, J. Laugis, and I. Galkin, "Middle-frequency isolation transformer design issues for the high-voltage DC/DC converter," in *Proc. IEEE Power Electronics Specialists Conference, 2008. PESC 2008. ,*, vol. 1, 2008, pp. 1930 – 1936.

[45] "5SNR 20H2500 data sheet," ABB, Doc. No. 5SYA1582-02, May 2004.

[46] M. Steiner and H. Reinold, "Medium frequency topology in railway applications," in *Power Electronics and Applications, 2007 European Conference on*, 2007.

[47] M. B. Beza, "Multilevel harmonic elimination methods for HVDC," Master's thesis, Dep. of Energy and Environment, Chalmers University of Technology, 2009.

[48] T. Nyikos and T. Tomaschett, "Experimental verification of a DC-DC converter for a DC wind farm," Master's thesis, Dep. of Energy and Environment, Chalmers University of Technology, 2006.

[49] A. Perdana, "Dynamic models of wind turbines; a contribution towards the establishment of standardized models of wind turbines for power system stability studies," PhD Thesis, Dep. Energy and Environment, Chalmers University of Technology, Göteborg, Sweden, 2008, iSSN-0346-718X.

[50] D. K. Cheng, *Fundamentals of Engineering Electromagnetics*. Addison-Wesley Publishing Cmpany, Inc., 1994.

[51] [Online]. Available: http://www.abb.com/hvdc,2009-05-08

[52] K. J. Karimi, A. Booker, and A. Mong, "Modeling, simulation, and verification of large DC power electronics systems," in *Proc. IEEE PESC'96*, vol. 2, 1996, pp. 1731–1737.

[53] T. Petru and T. Thiringer, "Modeling of wind turbines for power system studies," *IEEE Trans. Power Systems*, vol. 17, no. 4, pp. 1132– 1139, November 2002.

[54] A. Kulka, "Pitch and torque control of variable speed wind turbines," Master's thesis, Dep. of Energy and Environment, Chalmers University of Technology, 2004.

[55] E. Muljadi and C. P. Butterfield, "Pitch-controlled variable-speed wind turbine generation," *IEEE Trans. Industry Applications*, vol. 37, no. 1, pp. 240 – 246, January/February 2001.

[56] Z. Wang and L. Chang, "PWM AC/DC boost converter system for induction generator in variable-speed wind turbines," in *Electrical and Computer Engineering, 2005. Canadian Conference on*, 2005, pp. 591 – 594.

[57] L. Harnefors, "Control of variable-speed drives," Dep. of Electronics, Malardalen University, Vasteras, Sweden, Tech. Rep., 2002.

[58] M. Belkhayat, R. Cooley, and A. Witulski, "Large signal stability criteria for distributed systems with constant power loads," in *Proc. Power Electronics Specialists Conference, 1995. PESC '95 Record., 26th Annual IEEE*, vol. 2, 1995, pp. 1333 – 1338.

[59] P. Karlsson, "Small-signal modeling and analysis of DC distributed power systems," *EPE Journal*, vol. 17, no. 2, pp. 49 – 58, June 2007.

[60] A. Griffo, J. Wang, and D. Howe, "Large signal stability analysis of DC power systems with constant power loads," in *Proc. Vehicle Power and Propulsion Conference, 2008. VPPC '08. IEEE*, 2008, pp. 1 – 6.

[61] G. Michalke, A. D. Hansen, and T. Hartkopf, "Fault ride-through and voltage support of permanent magnet generator wind turbines," in *Proc. Nordic wind power conference NWPC 2007,*, 2007.

[62] A. Reidy and R. Watson, "Comparison of VSC based HVDC and HVAC interconnections to a large offshore wind farm," in *Proc. Power Engineering Society General Meeting, 2005. IEEE*, 2005.

[63] W. Freitas, A. Morelato, and W. Xu, "Improvement of induction generator stability using braking resistors," *IEEE Transactions on power systems*, vol. 19, no. 2, pp. 1247–1249, May 2004.

[64] A. Causebrook, D. J. Atkinson, and A. G. Jack, "Fault ride-through of large wind farms using series dynamic braking resistors (march 2007)," *IEEE Transactions on power systems*, vol. 22, no. 3, pp. 966–975, August 2007.

[65] P. Sandberg and L. Stendius, "Large scale offshore wind power evacuation by HVDC light®," in *Proc. European Wind Energy Conference, EWEC, 2008.*, 2008.

[66] A. Johnson, N. Tleis, and J. Greasley, "The development of connection requirements for offshore generation and transmission in Great Britain (GB)," in *Proc. 8th International Workshop on Large Scale Integration of Wind Power into Power Systems as well as on Transmisison Networks for Offshore Wind Farms*, 2009.

[67] L. Tang and B.-T. Ooi, "Locating and isolating DC faults in multi-terminal DC systems," *IEEE Transactions on power delivery*, vol. 22, no. 3, pp. 1877–1884, July 2007.

[68] ——, "Protection of VSC-multi-terminal HVDC against DC faults," in *Proc. Power Electronics Specialists Conf.*, vol. 2, 2002, pp. 719–724.

[69] J. Ribrant and L. Bertling, "Survey of failures in wind power systems with focus on swedish wind power plants during 1997 - 2005," *IEEE Trans. Energy Conversion*, vol. 22, no. 1, pp. 167 – 173, March 2007.

[70] Grid disturbance and fault statistics. [Online]. Available: http://www.nordel.org,2009-05-08

[71] R. M. Cuzner and G. Venkataramanan, "The status of DC micro-grid protection," in *Proc. Industry Applications Society Annual Meeting IEEE*, 2008.

[72] G. Biegelmeier and G. Rabitsch, "Körperströme und berührungsspannungen in der badewanne," *E und M*, vol. 103, no. 2, pp. 50 – 59, 1986.

Appendix A

Symbols and Glossary

A.1 Selected Symbols

Here, the the symbols related to the wind farm layout are shown, which are used in Chapters 4-7. The location of the variables in the wind farm can be seen in Fig. A.1 and in the HVDC link in Fig. A.2.

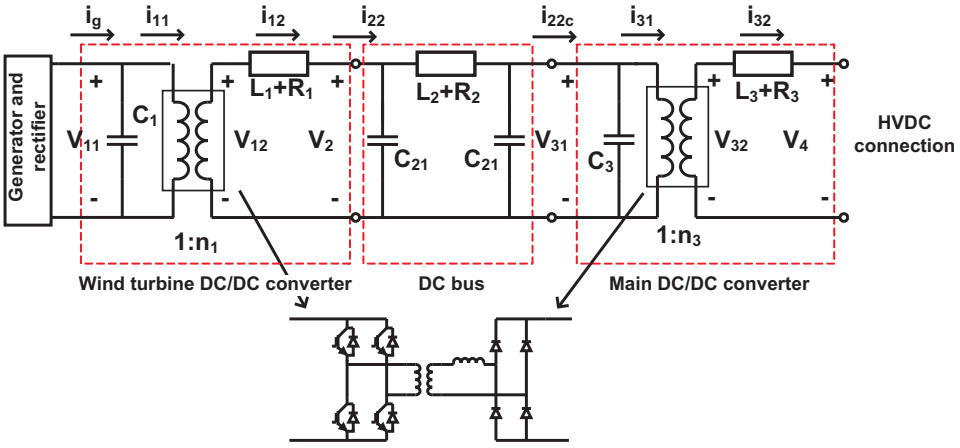

Fig. A.1 The equivalent circuit of the internal DC grid.

C_1	DC-link capacitor for the wind turbine.
C_{21}	Cable capacitance and filter capacitance.
C_3	Input capacitor for the main DC/DC converter.
i_{11}	Input current to the H-bridge in the wind turbine DC/DC converter.
i_{12}	Output current from the diode bridge in the wind turbine DC/DC converter.
i_{22}	Current in the DC bus.

i_{22c}	Input current to the main DC/DC converter.
i_{31}	Input current to the H-bridge in the main DC/DC converter.
i_{32}	Output current from the diode bridge in the main DC/DC converter.
i_g	Output current from the inverter towards the DC/DC converter.
L_1	Filter inductance for the wind turbine DC/DC converter.
L_2	Inductance for a cable segment.
L_3	Filter inductance for the main DC/DC converter.
n_1	Ideal voltage ratio for the wind turbine DC/DC converter.
n_3	Ideal voltage ratio for the main DC/DC converter.
R_1	Filter resistance for the wind turbine DC/DC converter.
R_2	Resistance for a cable segment.
R_3	Filter resistance for the main DC/DC converter.
V_{11}	Input voltage for the DC/DC converter in the wind turbine.
V_{12}	Output voltage from the diode bridge in the wind turbine DC/DC converter.
V_2	Output voltage from the DC/DC converter.
V_{31}	Input voltage to the main DC/DC converter.
V_{32}	Output voltage from the diode bridge in the main DC/DC converter.
V_4	Output voltage from the main DC/DC converter.

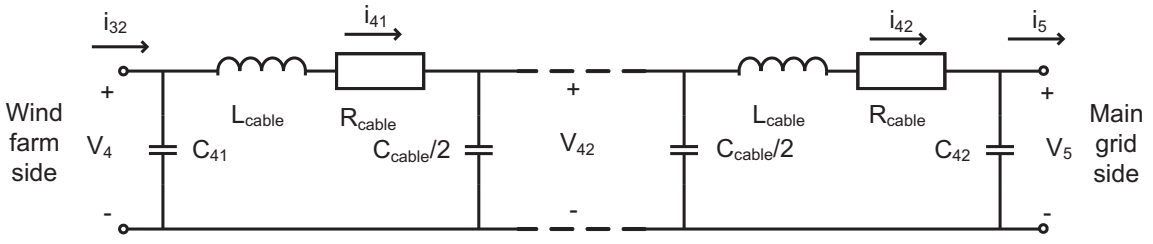

Fig. A.2 The equivalent circuit of the HVDC link.

C_{41}	Input capacitance for the HVDC link.
C_{42}	Output capacitance for the HVDC link.
C_{cable}	Capacitance for a cable segment.
i_{41}	Input current to the HVDC cable.
i_{42}	Output current from the HVDC cable.
i_5	Input current to the HVDC converter connected to the main grid
L_{cable}	Inductance for a cable segment.
R_{cable}	Resistance for a cable segment.
V_4	Output voltage from the main DC/DC converter.
V_{42}	Voltage at the middle of the HVDC link.

V_5	Output voltage of the HVDC link cable towards the main grid.

A.2 Glossary

BJT	Bipolar junction transistor
DFIG	Doubly fed induction generator
FB	Full bridge
HVAC	High voltage alternating current
HVDC	High voltage direct current
IG	Induction Generator
IGBT	Insulated gate bipolar transistor
LCC	Series parallel resonant converter
SAB	Single active bridge
VSC	Voltage source converter